Evaluation of Wind Tunnel Performance Testings of an Advanced 45° Swept Eight-Bladed Propeller at Mach Numbers From 0.45 to 0.85

C. Rohrbach, F. B. Metzger,
D. M. Black, and R. M. Ladden

NASA

NASA Contractor Report 3505

Evaluation of Wind Tunnel Performance Testings of an Advanced 45° Swept Eight-Bladed Propeller at Mach Numbers From 0.45 to 0.85

C. Rohrbach, F. B. Metzger,
D. M. Black, and R. M. Ladden
Hamilton Standard
Windsor Locks, Connecticut

NASA

National Aeronautics
and Space Administration

**Scientific and Technical
Information Branch**

1982

TABLE OF CONTENTS

TABLE OF CONTENTS (Cont)

SUMMARY

NASA-Lewis has completed wind tunnel performance tests of a fourth model Prop-Fan, SR-3, as a part of the NASA Aircraft Energy Efficient Program. A 62.2 cm (24.5 in) diameter variable pitch model was tested at Mach numbers from 0.45 to 0.85 in the NASA-Lewis 2.44 x 1.83m (8 x 6 ft) supersonic wind tunnel. This fourth Hamilton Standard model incorporates more sweep than the previous Prop-Fans. The aerodynamic design and the degree of blade sweep of SR-3 were influenced by noise reduction considerations which were analyzed with a recently developed acoustic theory. Hamilton Standard, under contract to NASA-Lewis, has analyzed the SR-3 test data and presented the results in this report.

The objective of the test and the data analysis programs was to establish and present the performance of this highly swept propeller over a wide range of conditions. These results have also been compared to earlier tests of the unswept SR-2 Prop-Fan and the 30° tip swept SR-1 Prop-Fan.

The model had eight blades which were swept aft 45° at the blade tips. SR-3 was designed to produce a net efficiency of 81.2% and a near field noise of 137 dB at the design cruise condition. The cruise design point is at a freestream Mach number of 0.80 at an altitude of 10.68 km (35000 ft.), a tip speed of 243.8 m/s (800 ft/sec) and a power loading of 301 kw/m^2 (37.5 HP/ft^2). The model Prop-Fan was tested with an integrally designed area-ruled spinner and specially contoured nacelle. The sweep was incorporated to minimize high Mach number performance losses and to produce acoustical phase interference which would result in reduced noise levels. The spinner and nacelle contours were selected to reduce blade section Mach numbers and to relieve blade root choking.

A net efficiency of 78.2% was achieved at the 0.80 Mach number design point. This is a 2% higher efficiency than that obtained for the 30° swept SR-1 model and 2.4% higher than that for the unswept SR-2 model, where all data are based upon NASA-Lewis tests. Comparisons showing both the predicted and the measured performance characteristics indicate fair agreement and point to the need for additional theoretical development.

INTRODUCTION

The potential benefits of the Prop-Fan (advanced turboprop) propulsion concept have been investigated in numerous propulsion and aircraft systems studies conducted by both the airframe and engine manufacturers under NASA sponsorship (Ref. 1-7). This work was largely undertaken in response to the worldwide energy shortage and the rapidly increasing cost of aviation fuel. These studies were initiated in late 1974 followed by the initial research programs in 1976.

The Prop-Fan is a small diameter, highly loaded, multi-bladed variable pitch advanced turboprop. The blades incorporate thin airfoils with sweep and are integrated with a spinner and nacelle shaped to reduce the axial Mach number through the blading. This configuration alleviates compressibility losses and results in higher propulsive efficiency than is achievable by high bypass turbofans. The envisioned installed configuration which incorporates the above advanced aerodynamic concepts is pictured in Figure 1. A complete discussion of the Prop-Fan concept is presented in References 8 and 9.

The Prop-Fan mated with a turboshaft engine of equal core technology to a turbofan engine exceeds the turbofan by 15 to 30 percent in efficiency at Mach 0.8 cruise speed and 25 to nearly 40 percent at Mach 0.7, resulting in about the same percentage reduction in fuel consumption.

In view of the attractive fuel savings potential of the Prop-Fan propulsion system, NASA has included the Advanced Turboprop Project as part of the extensive Aircraft Energy Efficient Program. The Lewis Research Center has total responsibility for this turboprop project which is summarized in Reference 10. The objective of the Advanced Turboprop Project is to demonstrate technology readiness for efficient, reliable and acceptable operation of turboprop-powered commercial transports at cruise speeds up to Mach 0.8 and at altitudes above 9.1 km (30,000 ft.). This technology would also apply to possible new military aircraft for a variety of missions.

Phase I of this project, titled Enabling Technology, was started in 1976. This effort included the wind tunnel testing of a series of 62.2 cm (24.5 in) diameter, 8 and 10-bladed Prop-Fan models aimed at establishing the aerodynamic design criteria to achieve the projected propulsive efficiency goals. To date four 8-bladed models, designated SR-1, SR-2, SR-1M and SR-3 have been designed and fabricated by Hamilton Standard. These models were designed for the same high speed cruise operating condition, i.e., 0.8 Mach number, 10.7 km (35,000 ft) altitude, 244 m/s (800 ft/sec) tip speed and a cruise power loading of 301 kw/m^2 (37.5 SHP/D^2). Two models, the 30° swept-bladed SR-1 and the straight-bladed SR-2 were tested in both the United Technologies Research Center's (UTRC) 2.44m (8 ft) high speed wind tunnel and in the NASA Lewis

2.44m by 1.83m (8 x 6 ft) supersonic wind tunnel. The third model, SR-1M, a twist and camber modification of the SR-1 based on test results, has been tested in the NASA Lewis wind tunnel. For the first three models, primary emphasis was on achieving high aerodynamic efficiency. Noise was not a design consideration in these models primarily because derivation of an adequate noise theory was not yet complete. However, based on experimental data, it was expected that incorporation of thin airfoil sections and blade sweep would reduce noise. The fourth model, SR-3, was designed for both improved aerodynamic efficiency and reduced noise utilizing the newly derived Hamilton Standard Prop-Fan noise theory. This model has been tested in the NASA wind tunnel. The test program in the UTRC wind tunnel on the SR-1 model is reported in Reference 9, and data for both the SR-1 and the SR-2 models are shown in Reference 11. Although the reports of the NASA wind tunnel tests for the SR-1, SR-2 and SR-1M models have not yet been published, data for these as well as for the SR-3 model are included in References 12 and 13. This report covers the testing of the fourth model, SR-3, and presents a discussion of the aerodynamic and acoustic design philosophy, a description of the test program and an analysis and a discussion of the test results.

AERODYNAMIC AND ACOUSTIC DESIGN APPROACH

Prior to the design of the initial Prop-Fan models an aerodynamic design procedure was developed based on the well-established Hamilton Standard Propeller Aerodynamic Prediction Method. The method was derived from the work of Goldstein, Reference 14, and will not be discussed herein. This Prop-Fan aerodynamic design procedure was used in designing the previous three models, SR-1, SR-2 and SR-1M and an improved revision has been used to design the latest model, SR-3 reported herein. The procedure has been discussed in References 8 - 12 and will be only briefly restated later.

Since a suitable acoustic theory for high speed swept-bladed propellers had not yet been developed, the first three Prop-Fan models were designed without the benefit of an acoustic analytical method to optimize the blade shape characteristics for minimum noise. Instead, design guidance was based on evaluation of the available noise data on conventional, straight-blade propellers operating at various tip speeds. Of course, this evaluation was done in the light of trends which were expected based on existing propeller noise prediction methodology. This existing methodology was limited to consideration of straight (unswept) blades and was limited in the amount of configuration detail that could be considered in the noise calculation. Fortunately, a new acoustic method, developed by Hamilton Standard in 1976-1977, was available for the design of SR-3. In view of the importance of noise to the acceptance of the Prop-Fan concept, SR-3 was optimized for reduced noise as well as improved efficiency relative to the earlier models. Thus, the unique shape of the SR-3 blade was dictated primarily by the acoustic requirements. The new acoustic theory is discussed in some detail. Additional theoretical discussions have been included in earlier technical reports and papers (References 15 and 16).

Aerodynamic Design Procedure

The procedure for the aerodynamic design of the Prop-Fan is accomplished by using several existing aerodynamic methods which best apply to particular portions of the Prop-Fan and nacelle combination. Briefly, as outlined in the block diagram of Figure 2, the approach is to model the Prop-Fan as a turbofan in the root sections where the gap-to-chord ratios are below 1.0, as a turboprop over the outer portions and as a swept wing for those sections incorporating sweep. To this end, conventional turbofan aerodynamics have been modified to represent the Prop-Fan root blading and nacelle combination with the usual influence of the turbofan duct removed. This method includes a streamline analysis coupled to empirical cascade data. The basic propeller performance prediction method was modified to incorporate 2-D compressible airfoil data with a cascade correction for the mid-blade portion. For the tip section, this same method has been further modified to incorporate a tip relief correction to account for the three-dimensional flow effect on compressibility losses. In addition, a method based on the two-dimensional wing cosine correlation for sweep effects on airfoil performance has been added to the propeller program.

Finally, development of a new compressible induction method based on the Biot-Savart equations was undertaken to account for the effects of the supersonic Mach number zone of silence and the swept lifting line on the induction at the outer portions of the blade. In addition, the method incorporated the same compressible airfoil data, cascade correction and sweep analysis as were included in the Hamilton Standard Propeller Performance Method. Also, a supersonic blade tip Mach cone correction to the airfoil data was incorporated in the method. Although not yet fully developed, this advanced method was used in the final optimization of the shape characteristics of the initial three models. A refined version of the method was similarly utilized in the final refinement of the SR-3 Prop-Fan model.

The design procedure begins with a preliminary analysis where the Prop-Fan diameter, number of blades, RPM, and power are selected. Blade thickness ratio distribution is generally chosen as the minimum allowable by stress limitations, aeroelastic considerations and the fabrication state-of-the-art. The initial blade planform is selected based on experience and a preliminary performance analysis of the design condition. Next, the velocity gradient at the Prop-Fan plane is obtained from calculations of the flow field around the spinner/nacelle configuration including the blade blockage. Then, with this velocity gradient and the selected initial geometry and design operating condition(s), the Prop-Fan is analyzed using the aerodynamic design method described above. With this program, the optimum loading distribution for minimum induced loss with corresponding minimum profile losses along the blade span is established by iterating between angle of attack (twist) and camber.

4

As previously mentioned, the blade root sections are relatively thick with low gap-to-chord ratios. Therefore, cascade effects are important and choking could be a problem. Since the conventional propeller theory does not apply under these conditions, the flow in this region is analyzed and cascade airfoils are selected using the turbofan methodology as indicated above.

Finally, the design must be checked at take-off and climb conditions. Because good low speed performance may require higher camber, the low camber selected for high speed cruise may need to be modified to a slightly higher camber. Then, with the inclusion of the root configuration designed by the turbofan method and the take-off climb constraints, final iterations with the aerodynamic program are required to assure that the final design achieves the highest cruise performance with acceptable take-off performance.

Since this basic program may not properly analyze the induction at the tips of blades operating at supersonic speeds, the aforementioned compressible induction method is then used for the final tailoring of the Prop-Fan model.

Prop-Fan Acoustic Design Procedure

In the SR-1 design, the features included to minimize noise were a reduction in airfoil thickness and a moderate amount of sweep. The reduction in thickness was expected to reduce the near field noise in cruise since thickness related noise is a dominant part of the noise of propellers operating at high tip speed. The moderate amount of sweep incorporated was expected to lower the effective Mach number at which the blade airfoils operate and, therefore, reduce the excess noise which has been observed in conventional propellers when they operate at tip relative Mach numbers exceeding the critical Mach number of the blade airfoils. Unfortunately, the effect of these design features could not be accurately analyzed without an appropriate theory. Thus, the earlier Prop-Fan models were not optimized for minimum noise.

However, in 1976 a theory was developed by Hanson (see ref. 17) which allowed prediction of near field noise of propellers operating at high subsonic speed. This theory was based on the Lighthill/Ffowcs-Williams "acoustic analogy" (see ref. 18) in which the equations of fluid motion are cast into a wave equation for acoustic pressure. Two components of noise are calculated by this theory, the first, called thickness noise, is dependent on the blade airfoil section thickness distribution and the second, called loading noise, is determined by the pressure loading distribution on the surface of the blade. A third term in the Lighthill/Ffowcs-Williams equation, the quadrupole source term, was ignored in this early theoretical development because it was believed to be small relative to the thickness term. In the formulation of this theory the propeller blades are assumed to travel along an infinite helical surface defined by the forward flight speed of the aircraft and the angular velocity of the propeller. In the calculation process, the

noise is calculated for a single blade traveling along the helical path and the noise from the other blades is added by superposition with appropriate time lags.

Figure 3 shows schematically the input requirements, computations, and output of the computer program which makes use of the above described theory. For propeller loading noise predictions the chordwise and spanwise blade differential pressure distribution is the input to the program. The spanwise variation in pressure is a function of the lift coefficient obtained from performance calculations for the propeller. The chordwise variation in pressure is based on the chordwise loading distribution of airfoils of the type used in the Prop-Fan design. For the design of the SR-3 a generalized chordwise loading distribution was used. For thickness noise calculations the actual blade thickness distribution is the input to the program.

The basic output of the program is the acoustic pressure waveform at a specified point in space assumed to be moving forward at the same speed as the propeller. The harmonic components of noise obtained from a Fourier analysis of this waveform are also an output. Thus, it is possible to calculate the noise at the location of a fuselage near a Prop-Fan as the aircraft is flying at cruise speed.

For the SR-3 the primary noise reduction feature of the design was the blade sweep which was optimized using the theory described above. This sweep optimization utilized the concept of destructive interference of noise from different spanwise stations on the propeller blade. This concept is based on the fundamental assumption of linear acoustics that the acoustic pressure at any observer position can be calculated as the sum of contributions from each element of the source volume and surface area. To be done correctly, the summation (or integration) process must account for the amplitude and phase of the elemental contributions. If source dimensions of the blades are greater than about 1/2 the wavelength of interest (i.e., if the source is "acoustically non-compact"), then at some observer positions, elemental signals from different positions of the source will arrive out of phase. The net noise will then be reduced by self-interference below the level which would be obtained if the source dimension were very small ("acoustically compact"). Although the term, "acoustically non-compact," is relatively new, the principle has been known for many years. For example, in Gutin's original theory for propeller noise (see ref. 19), the appearance of Bessel functions and the polar directivity pattern result from phase variation around the propeller circumference. For most conventional propellers, chordwise and spanwise phase variations can be neglected at blade passing frequency. However, the combination of high Mach number, many blades, and large chord of the Prop-Fan means that chordwise and spanwise phase variations must be included.

The phase interference concept is most clearly illustrated with reference to the effect of sweeping a blade planform as suggested by figure 4. At blade passing frequency, the noise from any spanwise strip of the blade is simply a sinusoidal wave with an amplitude

6

and phase angle. The noise from one blade as measured at a given point in space is simply the vector sum of the contributions from each spanwise strip and the noise of the total propeller is the product of the vector sum and the number of blades. The effect of sweeping the tip back is to cause the signal from the tip of the blade to arrive at the measuring point later than the signal from the mid-blade region thus causing partial interference and a reduction in net noise.

For the SR-3 design a graphical version of the concept discussed above was developed. In this graphical procedure the noise contributions associated with each spanwise strip of the blade are treated as vectors having amplitude and phase angle. Then, the summation of the contributions from the strips is performed by adding the vectors head-to-tail as shown in figure 5. In the figure at the left, the generally in-phase individual contributions from several spanwise locations on the blade starting from the root station at the lower left to the tip station at the upper right vectorially add up to a value shown by the resultant amplitude vector (the resultant noise). This is the general result for unswept and slightly swept Prop-Fan blades. However, in the figure at the right of figure 5 the phase differences of the individual noise contributions from these spanwise locations on the blade are seen to cause a substantial reduction in the resultant amplitude. This is the result for a Prop-Fan blade with proper blade sweep.

The effectiveness of blade sweep in reducing the noise predicted for the SR-3 as compared with that predicted for SR-1 is shown in figures 6 and 7. In these figures the vector plots are shown for the thickness and loading components of noise at dimensionless observer points 0.25 Prop-Fan diameters forward of the plane of rotation, in the plane of rotation, and 0.5 Prop-Fan diameters aft of the plane of rotation. The summation of the thickness and loading noise components are shown in the vector plots at the bottom of these figures. The observer locations in the figures were selected for study as experience had shown that near field noise for the design cruise condition would be a maximum in this region.

The greatest difference between SR-3 and SR-1 as seen in figures 6 and 7 is in the phase cancellation of the total noise ahead of the plane of rotation. Since this is where thickness noise tends to dominate, it has been concluded that thickness noise can be reduced effectively with sweep. However, aft of the plane of rotation, where loading noise tends to dominate, the sweep is not as effective.

The SR-3 is the result of an extensive study of the effect of configuration variables on noise. This study was constrained by the requirements to improve performance over previous Prop-Fan designs and by structural design limits. The greatest effects found in this study were those that result from increasing sweep and activity factor. A summary of these trends is shown in figure 8. Here it is shown that tip sweep of less than 30 degrees is not effective in reducing the total noise at any of the observer locations evaluated. In order to achieve substantial reductions a sweep of 40 to 50 degrees is required. Also, it is shown in figure 8 that an increase in activity factor relative to that of the SR-1 (slightly swept) or the SR-2 (unswept) Prop-Fan model blades is required to

reduce total noise. The combination of increased sweep and activity factor can be seen in figure 8 to be most effective at the observer locations ahead and in the plane of rotation. At the observer location 0.5 diameters aft of the plane of rotation some reduction can be observed, but is not as significant as that at other locations. This is due to the lack of effectiveness of sweep for reducing the loading noise which tends to dominate aft of the plane of rotation.

Figures 9, 10 and 11 show comparisons of the thickness, loading and total noise (the sum of thickness and loading) of the SR-1, SR-2 and SR-3. The greatest difference between the noise of the three configurations is in the thickness noise component of figure 9. For the slightly swept SR-1 design and the unswept SR-2 design, the thickness noise peaks near the plane of rotation. The lack of effectiveness of suppressing the thickness noise component of the SR-1 can be seen in figure 9. In contrast, the SR-3 design is predicted to show a reduction of about 14 dB in peak near field noise relative to SR-1 due primarily to its increased sweep.

The loading noise components of SR-1, SR-2, and SR-3 of figure 10 show that SR-3 is predicted to produce 7 dB lower peak near field noise as compared with SR-2. Based on figure 10, the sweep configuration of SR-1 was apparently effective in slightly reducing loading noise, but the increased activity factor and sweep of SR-3 is much more effective.

The predicted near field directivities of the total noise of the SR-1, SR-2, and SR-3 designs are shown in figure 11. SR-1 is seen to have a predicted peak of 142.6 dB. Even though SR-2 is unswept it is predicted to have a peak of 143.2, only 0.6 higher than SR-1. In contrast, SR-3 is predicted to produce a maximum of 137 dB or 6 dB less than SR-1. The noise components of SR-3 from figures 9 and 10 and the total noise from figure 11 are repeated in figure 12. It can be seen here that loading noise is the dominant contribution to total noise and that sweep has been effective in suppressing thickness noise.

In summary, the study which led to the SR-3 design has shown that the phase cancellation concept should be effective for reducing noise. Acoustic tests of the SR-1, SR-2 and SR-3 models in the United Technologies Acoustic Research Tunnel provide an indication of the benefits of the SR-3 concept. Those SR-3 acoustic results are presented in reference 20. Noise data have also been taken in the LeRC 8 by 6 tunnel and are presented in references 21 and 22 and briefly in this report. Further acoustic tests in flight to be conducted with the models installed on an air turbine drive mounted on a Lockheed Jetstar will provide additional information useful for further optimization of the phase cancellation concept.

MODEL DESCRIPTION

Utilizing the aerodynamic and acoustic design methodology described above, the SR-3 Prop-Fan model was designed for the same operating condition as were the previous three models, i.e., 0.8 Mach number, 10.668 km (35,000 ft) I.S.A. altitude, 244 m/s (800 ft/sec) tip speed and a power loading of 301 kw/m^2 (37.5 SHP/D^2). The design

goals of the SR-3 model were improved efficiency and significantly reduced near field noise compared to the earlier designs. Thus, the design effort required optimizing the blade shape for both performance and noise. This effort involved many design iterations to establish a configuration providing maximum efficiency and minimum noise. Many further iterations were required to satisfy the structural requirements. The final configuration of the SR-3 blade is pictured in figure 13. The calculations yield a net uninstalled efficiency if 81.2 percent and a total noise at blade passage frequency of 137 dB. These values represent an increment of approximately 2-2.5% increase in efficiency and 6-7 dB reduction in total noise compared to the predicted values of the previous models.

The nominal 62.2 cm (24.5 in) diameter was the same as that of the previous models. However, it should be pointed out that the diameter of variable pitch propellers with swept blades changes as the blade angle is varied. Thus, the diameter of the SR-3 model varies with blade angle as shown in figure 14. The static or zero RPM curve shows that the diameter varies from 62.2 cm (24.5 in) at approximately the feather angle to a maximum of 64.7 cm (25.5 in) at nearly flat pitch. As shown on the plot, the diameter is further increased with tip speed as the result of elastic deflection under centrifugal load.

The mechanism by which the diameter varies is shown schematically in figure 15. The height, y, of the tip airfoil center of gravity (CG) above a plane passing through the propeller axis of rotation and perpendicular to the pitch change axis is 31.12 cm (12.25 in). This height is shown in both the side and front views. The top view looking from tip to hub shows the distance, z, from the pitch change axis to the tip airfoil CG. The tip airfoil offset, Δ, is the perpendicular distance from the projected tip chord line to the pitch change axis. This dimension occurs because the SR-3 model was swept along the advance angle line rather than the extended chord line. These dimensions are constant for a given geometry. Finally, the projected distance, x, is from the section CG to the axis of rotation and varies with blade angle as a function of Δ and z. Thus, the tip radius at any blade angle is given by $R_{TIP} = (y^2 + x^2)^{1/2}$. For the SR-3 model Δ and z are .64 cm (0.25 in) and 9.0 cm (3.45 in), respectively. These values result in the static diameter variation with blade angle shown in figure 14.

In this report, the minimum or reference diameter, D_{ref}, of 62.2 cm (24.5 in) was selected to define the coefficients, C_p, C_T and J used in the basic performance maps. The actual values of T/ρ, P/ρ and V/n can be obtained from the coefficients by using the reference diameter. Full scale performance can be obtained for geometrically similar Prop-Fans by using an identically defined but scaled reference diameter.

The overall characteristics of the SR-3 Prop-Fan model are listed below:

8 blades

235 activity factor/blade (AF)

0.214 Integrated Design Lift Coefficient (C_{L_i})

45° blade tip sweep (Λ)

NACA 16 and 65/CA airfoils

The blade shape characteristics are presented in figure 16. The thickness ratio, t/b, distribution is identical to that incorporated in the previous models. The twist $(\Delta \beta)$, design lift coefficient (C_{LD}) and planform (b/D) distributions were established to provide optimum loading distribution at the design condition for maximum efficiency and minimum noise. In general, for aerodynamic performance, the sweep distribution is that required to effectively reduce the local relative Mach number (MN) along the blade radius below the corresponding critical MN of the airfoils, thus alleviating compressibility losses over the outer portions of the blades. However, as discussed above, the sweep and planform on the SR-3 model were established by the acoustic theory to achieve maximum source noise cancellation consistent with acceptable structural design. The resulting sweep distribution more than meets the aerodynamic requirements.

As shown in the photograph of figure 13, the planform sweeps forward from the root section to approximately the 45 percent radius and then sweeps back to the blade tip. This configuration was required to alleviate unacceptably high blade stresses due to centrifugal loads on swept blades. The resulting sweep distribution is shown in figure 17. The manufactured sweep of the line connecting the centers-of-gravity of the airfoils along the blade radius varies from 45 degrees at the tip to zero at the 45 percent radius to -25 degrees at the spinner surface. Since the airfoil sections are laid out along streamlines which vary from conical lines at the spinner to cylindrical lines at the blade tip, the total effective aerodynamic sweep is increased as shown in the figure.

The stacked view and the developed planform of the blade are shown in figure 18. The sweep was achieved as in previous swept models by first stacking the sections along the pitch change axis and on the proper streamline. Next, each section of SR-3 was oriented to the proper twist angle and then swept back on the helix defined by the advance angle. The airfoil sections selected for the SR-3 blade design are NACA Series 16 from the tip to the 53 percent radius and NACA Series 65 with circular arc (CA) camber lines from the 37 percent radius to the root with a transition fairing between. These airfoils were chosen for their high critical Mach number and wide, low drag buckets. The spinner and nacelle lines shown in figure 19 were configured to produce the flow retardation required to alleviate the blade root choking and to minimize compressibility drag rise. The spinner incorporates area-ruling and blends to a maximum nacelle diameter equal to 35 percent of the model Prop-Fan diameter. The nacelle configuration is the same as that of

the previous models. The Mach number distribution along the nacelle surface, including the effect of blade blockage, is shown in the figure. It is noted that no choking is indicated through the blade row. A mild supercritical bubble over the nacelle surface near the maximum diameter is indicated. However, this localized region of supercritical flow, with Mach numbers reaching only slightly above 1.1, is not expected to present a problem. In fact, tests on the SR-1 and SR-2 models showed these local Mach numbers to be barely over 1.0.

The calculated thrust and power coefficient distributions along the blade radius are presented in figure 20. The curves were derived from calculations utilizing the methodology based on Goldstein. The test results from the SR-1 and SR-2 models indicated blade loading distributions closer to those predicted by this method than by the original compressible induction method. A comparison of the test distributions with those predicted by both the Goldstein and the new compressible induction method are covered later in the report.

TEST FACILITIES

Wind Tunnel

The SR-3 Prop-Fan model test was conducted in the NASA-Lewis 2.44 x 1.83m (8 x 6 ft) Supersonic Wind Tunnel. This tunnel, described in reference 23, incorporates a 4.27m (14 ft) long, 5.8 percent porosity perforated test section to minimize model/wall interactions. The test section Mach number can be set from 0.36 to 2.00, well encompassing the 0.45 to 0.85 range required for this test. The tunnel was run in the propulsion mode for this SR-3 model test program. This is an open circuit mode where outside air is drawn in upstream and is exhausted to the atmosphere downstream of the model.

Propeller Test Rig

The Propeller Test Rig (PTR) was strut-mounted from the ceiling in the tunnel test section. The PTR and the SR-3 model are shown in the tunnel in figure 21. A cutaway view of the PTR is presented in figure 22. The model is driven by a three-stage air turbine utilizing high pressure air at 3.1 x 10^6 newtons/m^2 (450 psi) and heated to 366° K (660° R). The turbine is capable of delivering nearly 746 kw (1000 Hp) to the Prop-Fan model. The PTR metric system includes two separate axial force measuring systems. The primary system is a rotating balance which measures thrust and torque of the Prop-Fan and spinner. The second system includes a thrust meter located in the overhead vertical strut. Both systems measure propeller blade and spinner forces only, when corrected for internal pressure tares. Model parts, other than the spinner and blades, that are metric to the strut-mounted load cell are shielded from the freestream tunnel air by a windscreen (figure 22). Static and dynamic (i.e., spinning) calibrations of the balances were done before and during the SR-3 test period. The data transducer pickups are scanned with

the CADDE (Central Automatic Digital Data Encoder) system which converts steady state direct current signals to digital numbers. Rotational speed, torque and both measurements of axial force were each recorded twelve times during each data scan and then averaged. All of the reduced wind tunnel and PTR data is available on-line with about a 15 second lag. This permits the data to be perused and, if desirable, certain additional points may be included as the test is in progress.

The PTR and the metric systems were designed and developed specifically for conducting research on advanced propellers in the LeRC 8 x 6 tunnel.

Pressure Instrumentation

Pressure measurements were made internal to the PTR (figure 23a), and were necessary to obtain the Prop-Fan model apparent thrust from the balance axial force measurements. Additional pressure measurements were made on the surface of the nacelle which is located downstream of the model hub. The nacelle body, which was mounted on the PTR windscreen, incorporated four azimuthal rows of static pressure taps and is shown in figure 23b. Nacelle pressure measurements were made for each test performance point and for special tare runs. Measured nacelle surface Mach number distributions at Mach 0.8 for spinner only, blades at windmill, and blades powered near the design condition are presented in figure 19. The tare runs were made with a special smooth blade hub which had no blade holes. These measurements were used to obtain an incremental nacelle pressure force and, with the apparent thrust values, provided the required net thrusts of the model Prop-Fan. These testing procedures are discussed in more detail later in the text.

A special series of test runs with a wake survey probe were made after the performance runs were completed. This is a yawable, traversing probe which was mounted on the tunnel floor and downstream of the model blades, as shown in the photograph of figure 21. The probe was remotely controlled and measured radial distributions of static and total pressure, total temperature and swirl (yaw) angle of the wake flow. These data are useful in diagnosing the Prop-Fan exit flow characteristics and in determining blade loading distributions. Four samples of power loading distributions are discussed and presented later in the text.

PROGRAM DESCRIPTION

Objectives

The objectives of this test program were:

1. To establish the complete aerodynamic performance of the third generation, SR-3 Prop-Fan model over a Mach number range from 0.45 to 0.85.

2. To obtain detailed wake measurements for deriving radial loading distributions at selected operating conditions.

3. To compare the measurements with predicted performance and loadings.

Test Variables and Techniques

In order to achieve the objectives of this program the SR-3 Prop-Fan model was tested over a range of Mach numbers from 0.45 to 0.85. At each Mach number, model thrust and power were measured through a range of blade angle and rotational speed. The blade angle/Mach number combinations covered are listed in the following test run schedule:

Mach No.	0.45	0.60	0.70	0.75	0.80	0.85
$\beta_{0.75R}$						
45.5	X					
48.2	X	X				
51.5	X	X	X			
54.3	X	X	X			
57.3	X	X	X	X	X	
58.5		X	X	X	X	X
59.3		X	X	X	X	X
60.5		X	X	X	X	X
61.3		X	X	X	X	X
62.3		X	X	X	X	X
63.3		X	X	X	X	X
64.7		X	X	X	X	X

At each blade angle/Mach number combination, measurements were taken over an rpm range from the windmilling value to 9000, the maximum allowed by blade stress limitations. Each rotational speed setting constituted a test point.

Test Procedure

A special test procedure was adopted based on utilizing measurements from both the rotating balance and the strut-mounted force system (figure 22). This procedure was required to overcome a slow thermal drift in the thrust reading of the rotating balance,

which was apparently due to heat generated by its bearings. An initial series of wind tunnel runs was made to establish reference windmill drags for each Mach number/blade angle combination using the strut-mounted force system. To minimize any errors during this testing due to tunnel air passing over the metric parts of the model, a cover plate was installed on the aft end of the model. After establishing the reference windmill drags, incremental thrust data were obtained using the rotating balance in a windmill-power-windmill test sequence. At each desired power point, the model was first wind-milled, then a power point was taken, and this was followed by a second windmill point. By subtracting the average of the two rotating balance windmill points from the thrust at the power point an incremental propeller thrust was obtained that minimized any thermal drift errors. Incremental thrusts thus determined were added to the reference windmill drags determined in the earlier tests with the strut-mounted force system to establish the final thrust values for each power point. This procedure was repeated for each Mach number and blade angle combination. Torque was determined directly from the rotating balance as it was not sensitive to any adverse thermal effects. A further explanation of this procedure along with the equations used is given in Appendix A. A direct comparison of propeller performance using this procedure with measurements from another propeller test rig in a second wind tunnel (ref. 9) is shown in figure A.3. The agreement when identical propeller hardware was tested is quite good.

After completion of the performance run schedule, surveys of the wake were made with a remotely controlled traversing probe for selected Prop-Fan operating conditions. At these conditions, the probe was positioned radially and in yaw to measure the total and static pressures, total temperature and flow direction.

PROPELLER NET FORCE MEASUREMENTS

As described previously, the Prop-Fan model was tested in the presence of a nacelle which was designed to alleviate compressibility loss in the blade root sections. Also, as shown in the section entitled "Test Facilities", the propeller blades and spinner were the only external model components on the metric portion of the PTR. The simulated axisymmetric nacelle was attached to the ground portion of the model. With this force measurement arrangement it has been shown (ref. 24) that the propeller net thrust can-not be directly measured on the force balance. This is true because, as discussed in references 24 and 25 there is a mutual force interaction for a propeller operating in the presence of a nacelle. This interaction causes an increase in propeller thrust and a corresponding increase in the pressure drag on the nacelle. This higher propeller thrust has been classically referred to as apparent thrust and is the major force component mea-sured by the PTR balance. The Prop-Fan net thrust was obtained by correcting the ap-parent thrust for the equal and opposite change in pressure drag on the non-metric nacelle. The corrections were obtained from integrations of the nacelle surface pressure measure-ments which were taken for each test point and for special tare test points taken with the aforementioned special hub without blades.

14

The net propeller thrust is defined as the propulsive force of the blades operating in the presence of the spinner and nacelle flow field without the increase in thrust due to the mutual interaction. This thrust is analogous to the traditional isolated propeller thrust.

With the present model force arrangement the balance measures the algebraic sum of the apparent thrust, spinner drag, and internal pressure area forces. Therefore, to resolve these forces, a series of model tare tests were made first without the propeller blades to evaluate both the external spinner aerodynamic drag and the nacelle pressure drag.

FORCE BALANCE (FB)
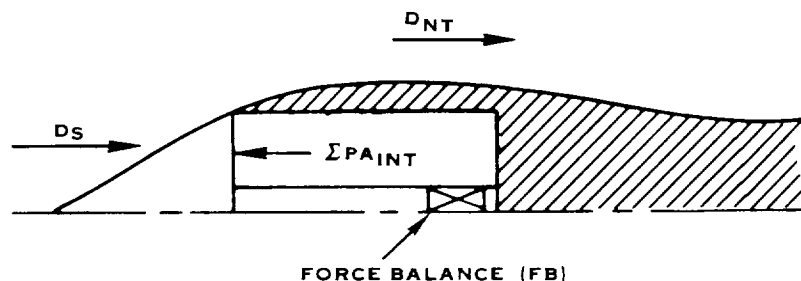
$$D_S = FB - \Sigma PA_{INT}$$
$$D_{NT} = \int (P_{S_N} - P_{S_O}) \, dA_N$$

In these tare tests the spinner for the performance testing was replaced by a "dummy" hub made without the holes for the blades. A special series of experimental runs was made to define the spinner aerodynamic and nacelle pressure drag for the same range of tunnel Mach numbers as would be tested with the model blades. Model RPM was shown to have no effect on measured spinner and nacelle drag. As shown in the above sketch, the spinner drag was measured directly from the force balance with a correction for the internal pressure area forces. The nacelle pressure drag (D_{NT}), was determined by pressure integration of the longitudinal rows of area-weighted pressure orifices. Spinner aerodynamic drag and nacelle pressure drag coefficients obtained in these tare tests are shown in figures 24 a and b.

With the blades installed and thrusting, the force balance measured the algebraic sum of the apparent thrust, the spinner drag, and the internal pressure area forces. The model forces are as shown in the following sketch:

FORCE BALANCE (FB)
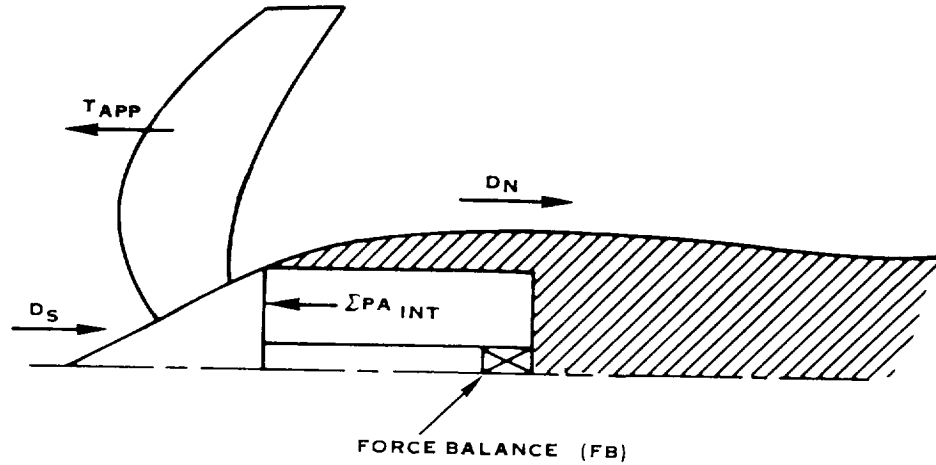
Therefore the apparent thrust of the propeller was obtained as shown in the following equation:

$$T_{APP} = FB - \sum PA_{INT} + D_S$$

and the nacelle pressure drag was obtained from nacelle surface pressure integrations:

$$D_N = \int (P-Po) \, dA$$

The change in nacelle pressure drag, ΔD_N, was obtained from the difference between these and the tare run pressure integrations =

$$\Delta D_N = D_N - D_{N_T}$$

Finally, the net thrust was obtained by subtracting the change in nacelle pressure drag from the apparent thrust:

$$T_{NET} = T_{APP} - \Delta D_N$$

RESULTS AND DISCUSSION

Formats for Force Data Presentation

The experimental force data corresponding to each freestream Mach number are completely contained in figures 25 through 30. In this format the data are shown as dimensionless power coefficient and net efficiency variations with advance ratio. Five or more

16

blade angle lines are shown on the figures for each of the six freestream Mach numbers. The power coefficients and the advance ratios are based upon the Prop-Fan reference diameter, D_{REF}, and are therefore referred to as $C_{P_{REF}}$ and J_{REF}. The true tip diameter, D, is larger than the 62.2 cm (24.5 in) reference diameter. The relationship between the true and the reference diameters has been previously discussed and shown in figure 14. Reference power coefficient and reference advance ratio are defined as:

$$C_{P_{REF}} = P/\rho_o n^3 D^5_{REF}$$

$$J_{REF} = V_o/n\, D_{REF}$$

The performance of the Prop-Fan is expressed as net efficiency, and this is the efficiency at which the model produces net propulsive thrust while operating in the velocity field of the nacelle and spinner. Net efficiency is defined as:

$$\eta_{NET} = \frac{\text{Net Thrust x Freestream Velocity}}{\text{Shaft Power}}$$

and, in dimensionless form:

$$\eta_{NET} = \frac{CT_{NET} \times J}{C_p}$$

Net efficiency is the same whether the coefficients are based upon true or reference coefficients as all the diameters cancel out in the dimensionless expression for η_{NET}.

The performance data presented is for a model configuration which has the gaps between the blade roots and the hub surface sealed. The gaps were disproportionately large for the model and were sealed to be more representative of a full scale Prop-Fan.

A group of four performance coefficient figures are shown for each test Mach number, except for $M_O = 0.45$. The first figure in each group, which is referred to as an efficiency map, summarizes the $C_{P_{REF}}$ and η_{NET} and blade angle. For clarity, the efficiency maps do not show the test data points. The data points and the data point fairings are shown in the second and third figures in each freestream Mach number group. The fourth figures shows the same η_{NET} vs J_{REF} fairings as the third figures but, again for clarity, without the data point symbols. The fourth figure was not necessary at the 0.45 freestream Mach number as the faired lines are clearly distinguishable from the data point symbols.

17

The faired lines in figures 25 through 31 are based upon extensive studies and crossplots of the experimental data. The faired lines accurately represent the data and yield smooth contours on the efficiency maps. The figures show that the actual data points do not always define smooth curves. However, smoothness was found to be improved for those data points which exhibited a difference of no more than ±0.01 in the windmilling advance ratios as obtained from the non-rotating and rotating balances. The windmilling advance ratio variation may be due to the blade locking mechanism which allows slight blade angle changes to occur during the initial powered operation at each new angle. The windmilling test procedures and the force measuring systems are described in the Test Procedure and Propeller Test Rig sections and in Appendix A of this report.

Additional performance characteristics for operating conditions that are of primary importance for Prop-Fan applications are presented in figures 32 through 40. In this second format the figures show variations in net efficiency with power loading, freestream Mach number, tip speed and altitude. These performance trends, which are in dimensional form, are based upon the true blade tip diameters as shown in figure 14 and upon the experimental data presented in figures 25 through 30. The relationships which have been used to generate these performance trend characteristics from the reference coefficient figures are presented in Appendix B. Additional relationships which were used in other sections of this report, and/or which clarify the variable diameter influence are also presented in the appendix.

A discussion of the experimental data in both the non-dimensional and the dimensional formats is presented in the following sections.

Reference Coefficient Data

The test data which define the SR-3 model Prop-Fan performance characteristics are summarized in figures 25 through 30. As previously stated, these figures show the data in dimensionless coefficient form for test freestream Mach numbers of 0.45, 0.60, 0.70, 0.75, 0.80 and 0.85. The coefficients are based upon the blade tip reference diameter and are therefore referred to as reference coefficients. Efficiency maps are presented for each freestream Mach number, which show contours of constant net efficiencies on lines for each blade angle of power coefficient versus advance ratio.

Net efficiency can be seen to vary from zero near the windmilling advance ratio (J_{REF} at $C_{PREF} = 0$) to a peak and then to lower values as advance ratio is decreased for each blade angle and freestream Mach number. These performance variations are rather completely related to the blade element angles-of-attack and relative Mach numbers which also vary with advance ratio. The blade elements generally operate at or near to the maximum profile lift to drag ratios at the peak efficiencies. The maximum L/D's, however, are dependent upon the blade element relative Mach numbers which increase with decreasing advance ratio at each freestream Mach number. Variations in blade tip relative Mach number with advance ratio are shown on each of the summary efficiency maps. These are the vector sums of the freestream and the tip rotational Mach numbers

18

and are independent of blade angle as they do not include the propeller induced velocities. The tip Mach numbers shown on the efficiency maps in figures 25 through 30 are based upon the model reference tip speeds and are calculated from:

$$MREL_{REF} = Mo \left[\left(\frac{\pi}{J_{REF}} \right)^2 + 1 \right]^{1/2}$$

The reference tip relative Mach numbers vary from about 0.60 to 1.25 for the test range of advance ratios and freestream Mach numbers. The actual tip relative Mach numbers are higher, by as much as 4%, and are defined by:

$$MREL = Mo \left[\left(\frac{\pi}{J_{REF}} \right)^2 \left(\frac{D}{D_{REF}} \right)^2 + 1 \right]^{1/2}$$

A number of performance characteristics can be obtained from visual inspections of the data presented in figures 25 through 30. Peak net efficiency, for example, is essentially constant at freestream Mach numbers from 0.45 to 0.70, but diminishes thereafter, and is five percent lower at 0.85 Mach number. It can be seen that C_{PREF} also decreases above 0.70 Mach number for any selected advance ratio and blade angle. At $J_{REF} = 3.1$ and $\beta_{0.75R} = 60.5°$, for example, C_{PREF} is 1.64 at $M_0 = 0.70$, but then drops to 1.49 at $M_0 = 0.80$ and to only 1.23 at $M_0 = 0.85$. Since the 9% and 25% lower power coefficients are accompanied by lower efficiencies, net thrust coefficient is down by 11% and 29% at the 0.80 and 0.85 Mach numbers respectively. The lower power coefficients at the design and higher Mach numbers were not expected, and for them to exist it is implied that the blade element lift coefficients were similarly lower. Since the SR-3 Prop-Fan was designed with a sufficient amount of blade sweep to promote subcritical operation, it appears that sweep is not as effective as expected.

Many other performance characteristics can be obtained either by an inspection of the curves or with a minimal amount of calculation and plotting. A few of the more interesting of these are summarized in Table I for nine conditions which can be read directly from the figures and for three which require inclusion of the true blade tip diameter. These conditions are identified in the table and are described in the correspondingly numbered listing below the table. Conditions 11 and 12 are based upon the approximation that the power required for an airplane in level flight is proportional to the cube of the freestream velocity, i.e., $P/\rho_0 V_0^3 = $ constant. The proportionality is valid if the airplane induced drag is small in comparison to the parasitic drag. In terms of the propeller coefficients, a constant $P/\rho_0 V_0^3$ for a given propeller diameter states that: $(P/D^2)/\rho_0 V_0^3 = C_p/J^3$. Based upon the reference diameter and figures 25 through 30 the power loading (P/D^2) is the reference power loading and C_p and J are reference parameters. The SR-3 model design J of 3.06 and C_p of 1.695 yield a $C_p/J^3 = 0.059$

for the 0.80 design freestream Mach number. Lines of constant C_P/J^3, or in this case C_{PREF}/J^3_{REF}, superimposed on the efficiency maps allow: (1) the assessment of airplane performance in level flight over the freestream Mach number range and (2) the rapid determination of the advance ratio (tip speed) at which net efficiency is a maximum for each Mach number. Two such lines for the design $C_{PREF}/J^3_{REF} = 0.059$ and for 60% cruise power, or $C_{PREF}/J^3_{REF} = 0.035$, are shown on the 0.80 Mach number efficiency map in Figure 31. These and identical lines were used in conjunction with each efficiency map to define the maximum net efficiencies in table I for the design power and 60% part power level flight.

TABLE I. NET EFFICIENCY VARIATIONS WITH MACH NUMBER FOR SELECTED OPERATING CONDITIONS

	Condition	$M_O =$	0.45	0.60	0.70	0.75	0.80	0.85
1.	$J_{REF} = 3.06$, $C_{PREF} = 1.695$		80.1	80.2	80.5	79.6	78.8	77.0
2.	$J = 3.06$, $C_P = 1.695$		79.5E	79.8	80.0	79.2	78.2	76.2
3.	Max η_{NET}		82.5	83.0	82.5	81.3	80.5	77.5
4.	Max η_{NET} @ $M\Omega_{REF} = 0.822$		81.0E	81.9	80.7	80.7	79.8	77.3
5.	Max η_{NET} @ $M\Omega = 0.822$		81.2E	82.0	81.0	80.8	80.0	77.4
6.	Max η_{NET} @ $MRE_{L_{REF}} = 1.15$		BD	BD	78.E	79.3	79.7	77.5
7.	Max η_{NET} @ $MRE_{L_{REF}} = 1.10$		BD	79.7	80.4	80.6	80.3	77.5
8.	Max η_{NET} @ $MRE_{L_{REF}} = 1.00$		80.0	82.0	82.0	81.3	79.0	74.E
9.	Max η_{NET} @ $MRE_{L_{REF}} = 0.95$		81.3	82.9	82.5	81.3	77.0	BD
10.	Max η_{NET} @ $MRE_L = 1.00$		80.2	82.1	82.1	81.4	78.6	73.E
11.	Max η_{NET} @ $C_{PREF}/J_{REF}^3 = 0.059$		82.5	82.0	80.8	80.0	79.2	77.0
12.	Max η_{NET} @ $C_{PREF}/J_{REF}^3 = 0.035$		82.5	83.0	82.5	81.3	80.5	77.5

BD = Beyond Data, E = Extrapolated

1. J_{REF} = Design J = 3.06, C_{PREF} = Design C_P = 1.695.

2. Design J = 3.06, Design C_P = 1.695.

3. Maximum net efficiency at each Mach number.

4. Maximum η_{NET} @ $M\Omega_{REF}$ = Design $M\Omega$ = 0.822, which is the rotational tip Mach number for the design tip speed of 243.8 m/s (800 fps) at an altitude of 10688 m (35000 ft).

5. Maximum net efficiencies at the design true $M\Omega = 0.822$.

6.-9. Maximum net efficiencies at reference tip relative Mach number of 1.15, 1.10, 1.00 and 0.95.

10. Maximum net efficiencies at a true tip relative Mach number of 1.00. These maximum efficiencies occur at J_{REF}'s that are D/D_{REF} higher than those for a reference tip relative Mach number of 1.00.

11. Maximum net efficiencies for an airplane in level flight and with the power required proportional to V_o^3 and equal to the design cruise power at 0.80 Mach number.

12. Same as 11 at 60% power.

Most of the tabulated results are self-explanatory, although some highlights are noted. As described earlier, the efficiency maps have been prepared with the use of the Prop-Fan reference diameter. Since the true SR-3 tip diameters are larger than the reference diameter at all test blade angles, the true Cp's and J's are smaller than the reference Cp's and J's. This means, then, that the reference maps must be entered at J_{REF}'s and $C_{P_{REF}}$'s that are greater than the true values in order to read true efficiencies. Some of the equations governing the relationships between true and reference quantities are presented in Appendix B.

Conditions 1 and 2 show that the net efficiency trends with freestream Mach number are similar for the true and the reference design advance ratios and power coefficients, but the level of the net efficiencies at the true J and Cp are from 0.4% to 0.8% lower. The 0.80 Mach number net efficiency at the true design J and Cp is 78.2% for the SR-3 model Prop-Fan, as shown in condition 2.

Conditions 4 and 5 show that the maximum net efficiencies at each test freestream Mach number are nearly the same at a true and at a reference 0.822 tip rotational Mach number. This Mach number corresponds to the design tip speed at the design altitude.

Variations in net efficiency with flight Mach number and with tip relative Mach number are illustrated in conditions 6 through 10. At 0.45, 0.60 and 0.70 flight Mach numbers the peak efficiencies occur at the lowest of the tabulated reference tip relative Mach numbers. At 0.75, 0.80 and 0.85 the peak efficiencies occur at higher reference tip relative Mach numbers, but within the range of those in the tabulation. For the design value of the reference tip rotational Mach number, $M\Omega_{REF} = 0.822$, the values of $MREL_{REF}$ vary from 0.937 to 1.182 as flight Mach number varies from 0.45 to 0.85, and is equal to 1.147 at the 0.80 design Mach number. Conditions 8 and 10 compare the

peak net efficiencies for a true and reference tip relative Mach number equal to 1.0. The differences are small except at 0.80 and 0.85 Mach number, where a 1.0 tip relative Mach number occurs to the right of the constant efficiency contours and where efficiency changes fast for small changes in advance ratio.

The eleventh and twelfth conditions express the peak net efficiencies at each Mach number where the operating points are governed by $P/\rho_0 V_0^3 = $ constant. This power-velocity relationship is expressed through the dimensionless coefficients as:

$$\frac{C_{P_{REF}}}{J^3_{REF}} = \frac{P/D^2_{REF}}{\rho V_0^3}$$

Condition number 11 represents the design point value of the power-velocity relationship examined at each of the tunnel freestream Mach numbers. These represent reference quantities, and the line of constant $C_{PREF}/J^3_{REF} = 0.059$, as shown on the 0.80 Mach number efficiency map in figure 31, passes through the design point values of $C_{PREF} = 1.695$ and $J_{REF} = 3.06$. The maximum efficiency on this line is 79.2%, or 0.4% higher than the reference design point efficiency. The higher efficiency occurs at a lower J_{REF} and therefore at a higher reference tip speed than the design values. Condition number 12 represents 60% of the design point power and is expressed as $C_{PREF}/J_{REF}^3 = 0.035$. It is interesting to note that the peak efficiencies at this loading level are equal to the maximum efficiencies at any C_{PREF} and J_{REF} combination, as shown, for example, in condition 3.

Dimensional Performance Trend Data

The coefficient data in figures 25 through 30 are shown in the most general and useful form to establish specific performance trends. Variations in net efficiency with power loading, tip speed and freestream Mach number that were obtained from these data are shown in figures 32 through 40. These performance trends are based upon the true tip diameters. The true diameters, expressed as percents of the 62.2 cm (24.5 in) reference diameter, are also shown on the performance trend curves.

The performance trends with tip speed and power loading at the design altitude are shown in figures 32 through 35 for cruise Mach numbers of 0.70, 0.75, 0.80 and 0.85. At each Mach number the highest peak net efficiency occurs at the lowest tip speed. In figure 34 at 0.80 Mach number, for example, the peak net efficiencies range from 80.2% to 79.7% at tip speeds of 213.3 m/s (700 fps) and 259.0 m/s (850 fps) respectively. The corresponding power loadings are 170 kw/m^2 (20 HP/ft^2) and 240 kw/m^2 (30 HP/ft^2).

Figures 32 through 35 can also be used to establish the maximum available net efficiencies at the design point value of the power/velocity relationship, $C_P/J^3 = 0.059$. The maximum efficiencies and the associated power loading and tip speeds for the design altitude

22

are summarized in table II. The tip speeds which produce these maximum efficiencies are higher than the design tip speed at all but the 0.70 freestream Mach number. At 0.80 Mach number the optimum tip speed at the design power loading is 10% higher than the design speed of 243 m/s (800 ft/sec). The net efficiencies at the power loadings shown in the table and at a tip speed of 243 m/s (800 ft/sec) are obtained from figures 32 through 35, and are 80.5%, 79.8%, 78.2% and 75.3% at the 0.70 to 0.85 freestream Mach numbers.

TABLE II - MAXIMUM NET EFFICIENCY AT
$Cp/J^3 = 0.059$

M	Net Efficiency %	Power Loading kw/m^2	(hp/ft^2)	Tip Speed m/s	(fps)
0.70	80.6	200	(25.1)	236.2	(775)
0.75	80.1	247	(30.9)	251.4	(825)
0.80	79.0	300	(37.5)	268.1	(880)
0.85	76.8	360	(45.0)	277.3	(910)

Variations in net efficiency with power loading and freestream Mach number are shown in figures 36 and 37 for the design tip speed and altitude. The same data are shown in these two figures with merely a switch in the abscissa and independent variables. Both figures show that the power loading at peak efficiency increases with increasing Mach numbers.

The effect of altitude on the relationship between net efficiency and power loading is shown in figure 38 at the design tip speed and freestream Mach number. The data covers higher power loadings at the lower altitudes due to the associated higher air densities. The peak efficiencies are slightly higher at the lower altitudes due to favorable increases in advance ratio at the selected tip speed and Mach number.

The performance trends at 0.45 Mach number are shown in figures 39 and 40 for sea level and 7634 meter (25,000 foot) altitude climb conditions respectively. The variations in net efficiency with power loading for three tip speeds are shown on each of these figures.

Performance Comparison With Predictions

One of the important objectives of the SR-3 Prop-Fan program was to utilize the measured performance to assess the aerodynamic design and performance predictive methodology. Two Prop-Fan methods have been compared with test. The first, program H444, the Hamilton Standard Propeller Method, discussed previously, is the basic propeller performance method, which has been revised to account for blade sweep and for

23

cascade airfoil effects. The method uses compressible airfoil data and calculates blade induced flow from the Goldstein theory (ref. 14). The second method, program H409, is a compressible vortex method developed especially for Prop-Fans. The major difference in the two methods is that the latter method corrects the induced velocity for supersonic relative Mach number effects and corrects the two-dimensional compressible airfoil data for Mach cone effects. The H409 program also includes the effect of the trailing vortex system on the induced flow of the swept lifting line as well as the bound circulation contribution of the swept blades to the induced velocity.

Comparisons of the calculated and test performance were developed to assess the ability of the methods to show the proper trends with Mach number, blade angle and advance ratio. These comparisons are shown in figures 41 through 43.

Variations in net efficiency with freestream Mach number for the test data and for both the H444 and H409 programs are shown in figure 41. These comparisons are for operation at the design advance ratio (J = 3.06) and power coefficient (Cp = 1.695) at each Mach number. The test and the calculated blade angles at the 0.80 design freestream Mach number are shown at the top of the figure. Variations in the change in blade angle with Mach number from the 0.80 Mach number blade angles which are necessary to maintain the design J and Cp are shown in the upper half of the figure. It can be seen that both methods under predict the design point blade angle by approximately four to five degrees. Blade angle descrepancies have also been observed in the earlier Prop-Fan model tests, and whereas the reasons for this are not fully understood the magnitude of the discrepancies has been observed to be dependent upon the amount of blade tip sweep.

It is noted that the trend in the blade angle change with Mach number is reversed in relation to the test data for the H444 program and is predicted somewhat better with the H409 method. Both the level of net efficiency, particularly at 0.80 Mach number, and the performance trend with Mach number are predicted best by the compressible vortex method.

The curves in the upper half of figures 42a through 42c show the performance comparison trends for variations in blade angle and freestream Mach number. Advance ratio is fixed at J = 3.06 for each of these figures and the power coefficient variations are due to the blade angle changes which are shown in the lower half of the figures. The blade angle changes are in relation to the blade angles, shown at the top of each figure, which are required for a J = 3.06 and Cp = 1.695. The performance at each Mach number is over predicted by both methods, but the correlation with the test results is better with the H409 program. This method correlates quite well at 0.80 Mach number but over predicts the efficiency by 1.5% to 2.0% at 0.75 and 0.85 Mach number. The slope of the Cp variation with blade angle change is also better predicted by the compressible vortex method.

Comparisons of test and predicted performance with variations in advance ratio are shown in the upper half of figures 43a through 43c at freestream Mach numbers of 0.75, 0.80 and 0.85. Blade angle is held fixed at the values shown at the top of these figures, and these are the same angles as in figures 42a through 42c. The performance levels predicted with the H409 program are again in better agreement with the test results, although the shapes of the η_{NET} versus J curves are better matched by the H444 method. The lower half of the figures show the comparison in the variations in Cp with changes in J. Here, the H444 method produces the better comparisons, but neither program matches the test results very well.

In summary, the levels of predicted net efficiencies with the H409 program are in better agreement with the experimental data than are those predicted with the H444 program. H409 accurately calculates the SR-3 design point net efficiency while the H444 calculated efficiency is 3% too high. Both methods underestimate the design point angle by from 4 to 5 degrees.

Power Loading Analysis from the Wake Survey Probe Data

Four of the test conditions for which the wake survey probe (WSP) was installed were selected to examine the spanwise distributions of elemental power coefficient, dCp/dx. Measurements of static and total pressure, total temperature and flow direction were made at a number of radial positions. The probe was located 13.0 centimeters (5.13 inches) downstream of the SR-3 blade pitch centerline.

The four test conditions which were analyzed are summarized in table III. Each of these is for an advance ratio which is near the design value, J = 3.06. The three quarter radius blade angle is the same for each case and is one degree lower than that which produces the design Cp and J at 0.80 Mach number. These data are based upon the calculated actual blade tip diameters.

TABLE III. WAKE SURVEY PROBE CONDITIONS USED
TO ESTABLISH POWER LOADING DISTRIBUTIONS

M	J	Cp	β0.75R	Tip Speed m/s	(fps)	Power Loading kw/m^2	(HP/ft^2)	Pressure Ratio	Tip Rel. Mach No.
0.70	3.007	1.504	60.7°	217	(713)	142	(35.4)	1.0461	1.010
0.75	2.995	1.457	6C.7°	233	(765)	137	(34.3)	1.0511	1.086
0.80	3.002	1.385	60.7°	249	(816)	131	(32.6)	1.0571	1.158
0.85	2.978	1.177	60.7°	266	(872)	111	(27.7)	1.0565	1.237

The elemental power coefficient distributions which were calculated from the traversing wake survey probe measurements are shown by the circled points in figures 44a through 44d. The probe data offered a choice between total temperature and swirl angle measurements from which to make these calculations. The total temperatures rather than the swirl angles were selected for three principal reasons: (1) they produce loadings which integrate closer to the power coefficients obtained from the rotating balance, (2) coupled with the total pressure they convert to more realistic adiabatic efficiencies than those based upon the swirl angle measurements, and (3) the temperatures generally showed less scatter and less sensitivity to the blade tip vortices. The calculation procedures which were used to obtain the dCp/dx distributions from both the total temperatures and the swirl angles are presented in Appendix C.

The four power coefficient distributions shown in Figures 44a through 44d are for a test blade angle of 60.7°, for advance ratios near the 3.06 design J and for the balance measured true Cp's that are indicated on the figures. The calculation blade angles were selected to match the measured Cp's and are from four to five degrees lower than the test blade angle. Integrations of the wake survey peak dCp/dx distributions yield Cp's of 1.50, 1.54, 1.42 and 1.29 at Mach numbers of 0.70, 0.75, 0.80 and 0.85 respectively.

Each of the wake survey probe loading distributions exhibit irregularities in the vicinity of the blade tips. These irregularities are believed to be associated with tip shocks, tip vortices and to the tip geometry of the SR-3 model. The shape of the four loading distributions are quite similar except at 0.85 Mach number where the tip loading is more irregular and dCp/dx falls off near the blade root. At this condition the shock strengths are highest, as the tip relative Mach number is 1.237, and blade root choke has been observed in the data.

As previously stated, the total temperature measurements were generally preferred over the swirl angle measurements for the purpose of calculating loading distribution. The swirl angle measurements were found to exaggerate the tip loading irregularities. Total temperature ratios obtained directly from the measurements and as calculated from the measured swirl angles for the 0.80 Mach number loading condition are shown in figure 45. Equivalency in appendix C was used to make this calculation, and the larger swirl dependent tip irregularity as well as the lower temperature ratio level are shown in the figure. The 0.85 Mach number distribution which is also shown is very irregular for the full span of the probe survey. At this Mach number the swirl angle measurements did not exhibit as much irregularity, and, as shown in figure 46, were as small as the 0.80 Mach number distribution.

Comparisons of Wake Survey Probe and Predicted Loading Distributions

Predicted loading distributions based upon the two previously discussed Hamilton Standard aerodynamic programs are also shown on figures 44a through 44d. These programs, H444 and H409, have been described in some detail in the Aerodynamic Design Proce-

dure section of the text. The H444 loadings are shown by the dashed lines in the figures and the H409 loadings are shown by the solid lines.

Both the H444 and the H409 predicted loadings agree fairly well with the loading calculated from the WSP measurements. Generally the mid-span loadings are predicted better by H444, while H409 produces a better match for the tip region loadings. Both programs under predict the root loadings except at 0.85 Mach number where the test dCp/dx falls off due to blade root choke.

The basic shapes of the H444 loadings are very similar at each Mach number. These predictions show peak loadings at fractional radii between 0.80 and 0.85. The shapes of the test loading are also quite similar at each Mach number, peaking perhaps a little nearer the tip. The H409 loading shapes, on the other hand, are dependent upon Mach number. The peaks occur further outboard at the lowest Mach number and further inboard at the highest Mach number than either the test or the H444 program loadings. It is fairly evident that further aerodynamic method development is required to improve the loading as well as the overall performance correlations for highly swept, high speed Prop-Fans.

PERFORMANCE COMPARISONS OF PROP-FAN MODELS

As previously pointed out, the SR-3 Prop-Fan model is the fourth in a series of models tested in the LeRC 8 x 6 tunnel. Accordingly, it is appropriate to present a brief comparison of the results of the four Prop-Fan models tested to date.

A photograph of an SR-3 blade is shown in figure 47 along with a 30° swept SR-1 blade and a straight SR-2 blade. The SR-1M blade, not shown, is similar to SR-1 except for a tip twist and section camber modification. Although the test reports on these models have not yet been published, the final performance data on the SR-1 and SR-2 models are available. Final corrections to the test data for the SR-1M model have not yet been established, at the time of this analysis of the SR-3 data.

The SR-3 Prop-Fan has shown the highest net efficiency of any model tested to date at the Mach 0.8 design cruise condition. Moreover, this model does not show the rapid fall-off in efficiency as Mach number is increased above 0.8. The measured net efficiency of the SR-1, SR-2 and SR-3 8-blade Prop-Fan models operating at the design advanced ratio and power coefficient are shown in figure 48. Note that the SR-3 model comes within 2.0 percent of the 80 percent efficiency goal at 0.80 Mach number. At Mach 0.85, the SR-3 model achieves an efficiency of 76.2 percent, exceeding the SR-1 and SR-2 by 3.5 and 3.0 percentage points, respectively. Over the entire Mach number range the SR-3 model shows the highest efficiencies. The figure indicates that the Prop-Fan performance is improved as sweep is increased. It is expected that new models, whose designs will incorporate the experience gained and the improved aerodynamic and acoustic methods being developed, will show further improvements in performance and source noise reduction.

27

LIMITED ACOUSTIC COMPARISONS

It has been pointed out that the SR-3 model was the first of the Prop-Fan mode is to be designed for both maximum performance and minimum near field noise. Near field noise measurements were made on this as well as on the SR-1 and SR-2 model Prop-Fans. The acoustic tests were conducted in the UTRC Acoustic Research Tunnel (ref. 15 and 20) and in the LeRC 8 x 6 tunnel (ref. 21 and 22). These data have not only established near field noise levels for Prop-Fans but have also provided a correlation data base for this contractor's newly developed noise theory. The initial correlations that have been made for these three models generally confirm the predicted acoustic trends that were previously shown in figure 11.

Transducer locations and data from the LeRC acoustic tests are shown in figure 49. Evident in figure 49(b) is the directivity of the blade passage tone measured on the tunnel ceiling. This indicates that any required fuselage treatment would be limited in area. Figure 49)c) presents the peak level of the blade passage tone at different helical tip speeds. The tip speed was changed by operating the tunnel at different free-stream Mach numbers and running the propeller at near design Cp and J. Both data plots show significant noise reduction (5 to 6 dB) for the 45° swept SR-3 design relative to the unswept design.

The acoustic measurements in both tunnels have shown that reduced levels of near field noise have been achieved with the SR-3 model Prop-Fan. These improvements were made as a result of a dedicated low noise design effort.

28

CONCLUSIONS

1. The SR-3 model achieved a net efficiency of 78.2% at the 0.80 Mach number design point.

2. The model achieved a maximum net efficiency of 80.4% at the 0.80 design Mach number.

3. The maximum net efficiency of the model at 0.85 Mach number is 77.5%, indicating that the performance fall off above the design Mach number is modest.

4. Maximum net efficiencies between 82.5% and 83.0% were measured at Mach numbers from 0.45 to 0.70.

5. The 78.2% design point efficiency of the 45° swept SR-3 Prop-Fan model exceeds the performance of the 30° swept SR-1 model by 2.0% and the unswept SR-2 model by 2.4%.

6. The wake survey probe measurements indicate the presence of flow irregularities near the blade tip. These are most likely due to the blade tip vorticity and are present at all Mach numbers. The measurement also show a significant reduction in root power loading at 0.85 Mach number where blade root choke has been detected.

7. Performance comparisons made with Hamilton Standard's two aerodynamic methods show fair agreement with the test results. The design point efficiency is accurately calculated with the newer compressible vortex method, but the efficiencies calculated with either method are generally higher than test.

8. Significant noise reductions have been measured for the aero/acoustically designed SR-3 model Prop-Fan.

LIST OF SYMBOLS

A	–	noise amplitude
A	–	area
AF	–	blade activity factor $= 6250 \int_{Hub/tip}^{1.0} (b/D) \, x^3 \, dx$
b	–	elemental blade chord, m
c	–	speed of sound
C	–	absolute velocity, m/sec
CLD	–	elemental blade design lift coefficient
CL_i	–	integrated design lift coefficient $= 4 \int_{Hub/tip}^{1.0} CLD \, x^3 \, dx$
CP	–	specific heat at constant pressure, 1004 (J/kg)/K
C_P	–	power coefficient $= P/\rho_o n^3 D^5$
C_T	–	thrust coefficient $= T/\rho_o n^2 D^4$
CTB	–	thrust coefficient direct from power-point data (Appendix A)
CTP	–	corrected thrust coefficient for power-point (Appendix A)
CTWB	–	average of effective thrust coefficients from windmill points before and after a power-point
C_x	–	axial velocity, m/sec
Cu	–	swirl velocity, m/sec
D	–	drag, N
D	–	blade tip diameter, m
dB	–	decibel

30

dCp/dx — elemental power coefficient

dC_T/dx — elemental thrust coefficient

FB — force balance

g — gravitational constant, 9.8 m/sec^2

J — advance ratio $= V_o/nD$

J — mechanical equivalent of heat (Appendix C)

JP — advance ratio for power-point (Appendix A)

JPR — reference windmill advance ratio

JPW — average windmill J before and after power points

J_{wind} — advance ratio during windmill drag runs

M — Mach number

MREL — blade tip relative Mach number

$M\Omega$ — blade tip rotational Mach number

n — rotative speed, rps

N — rotative speed, rpm

P — power, watt

PA — pressure forces in the form $(P - P_o)$ *Area, N

PR — total pressure ratio $= P_t/P_{to}$

P_S — static pressure, N/cm^2

P_T — total pressure, N/cm^2

PTR — propeller test rig

LIST OF SYMBOLS (Continued)

q	-	dynamic pressure, N/cm^2
Q	-	operating condition constant (Appendix C)
r	-	radius, m
R	-	tip radius, m
R	-	universal gas constant, m/K
r/R	-	fractional radius
S	-	operating condition constant (Appendix C)
SHP	-	Prop-Fan shaft horsepower
t	-	elemental blade maximum thickness, cm
T	-	thrust, N
TR	-	total temperature ratio = T_t/T_{t_o}
T_s	-	static temperature, °K
T_t	-	total temperature, °K
U	-	elemental rotational velocity, m/sec
V	-	velocity, m/sec
W	-	weight flow, kg/sec
WSP	-	wake survey probe
x	-	fractional radius, x = r/R
X	-	length aft of nacelle leading edge
β0.75R	-	Prop-Fan chord angle at 75% tip radius, deg
βeq	-	equivalent β0.75R used in Appendix A
γ	-	ratio of specific heats, 1.4

η —   efficiency $= TV_o/P \times 100$

Λ —   blade tip sweep angle (relative to radial line through blade root), deg

ηad   —   adiabatic efficiency $= (PR^{2/7}-1)/(TR-1) \times 100$

ρ —   mass density, kg/m^3

ϕ —   phase angle, deg

θ —   pitch angle, deg

ψ —   yaw (swirl) angle, deg

Subscripts

APP   —   apparent

EFR   —   effective or net from reference windmill drag data

N   —   nacelle, or nacelle maximum radius, 10.8 cm

NET   —   net

NT   —   nacelle tare

REF   —   reference, based upon 62.2 cm (24.5 in) reference diameter

S   —   spinner

w   —   wake survey probe

o   —   tunnel freestream condition

REFERENCES

1. "Cost/Benefit Tradeoffs for Reducing the Energy Consumption of the Commercial Air Transportation System", Douglas Aircraft Co; NASA Ames Contract NAS2-8618, NASA CR-137925 Summary Report, June 1976.

2. "Study of the Cost/Benefit Tradeoffs for Reducing the Energy Consumption of the Commercial Air Transportation System", Lockheed-California Company, NASA Ames Contract NAS2-8612, NASA CR-137927 Summary Report, August 1976.

3. "Energy Consumption Characteristics of Transports Using the Prop-Fan Concept", Boeing Commercial Airplane Company, NASA Ames Contract NAS2-9104, NASA CR-137938 Summary Report, October 1976.

4. "Study of Unconventional Aircraft Engines Designed for Low Energy Consumption", Pratt-Whitney Aircraft, NASA Lewis Contract NAS3-19465, NASA CR-135065 Final Report, June 1976.

5. "Study of Cost/Benefit Tradeoffs for Reducing the Energy Consumption of the Commercial Air Transportation System", United Airlines, NASA Ames Contract NAS2-8625, NASA CR-137891, June 1976.

6. "Study of Unconventional Aircraft Engines Designed for Low Energy Consumption", General Electric Co., NASA CR-135136, December 1976.

7. "Fuel Conservation Merits of Advanced Turboprop Transport Aircraft", Lockheed-California, NAS2-8612, NASA CR-152096 August 1977.

8. C. Rohrbach and F.B. Metzger, "The Prop-Fan - A New Look in Propulsors", AIAA Paper 75-1208 AIAA/SAE 11th Propulsion Conference, Anaheim, California, September 29, 1975.

9. D. Black, R.W. Menthe and H.S. Wainauski, "Design and Performance Testing of an Advanced 30° Swept, Eight Bladed Propeller at Mach Numbers from 0.2 to 0.85", NASA Lewis Contract NAS3-20219, NASA CR-3047, September 1978.

10. J.F. Dugan, Jr., NASA LeRC, B.S. Gatzen and W.M. Adamson, United Technologies, "Prop-Fan Propulsion- Its Status and Potential", SAE Paper 780995, November 1978.

11. Mikkelson, D.C.; Blaha, B.J.; Mitchell, G.A.; and Wikete, J.E., "Design and Performance of Energy Efficient Propellers for Mach 0.8 Cruise", NASA TMX-73612 and SAE Paper 770458, March - April, 1977.

34

REFERENCES (Continued)

12. Jeracki, R. J.; Mikkelson, D. C.; and Blaha, B. J., "Wind Tunnel Performance of Four Energy Efficient Propellers Designed for Mach 0.8 Cruise", NASA TM 79124 and SAE Paper 790573, April, 1979.

13. Mikkelson, D. C.; and Mitchell, G. A., "High Speed Turboprops for Executive Aircraft - Potential and Recent Test Results", NASA TM 81482.

14. Goldstein, S., "On the Vortex Theory of Screw Propellers", Proceedings of the Royal Aeronautical Society, Series A, Vol. 123, 1929.

15. Metzger, F. B.; and Rohrbach, C., "Aero Acoustic Design of the Prop-Fan", AIAA Paper 79-0610, March, 1979.

16. Hanson, D. B.; and Fink, M. R., "The Importance of Quadrupole Sources in Prediction of Transonic Tip Speed Propeller Noise", Journal of Sound and Vibration (1979) 62(1), pp 19-38.

17. D. B. Hanson, "Near Field Noise of High Tip Speed Propellers in Forward Flight," AIAA Paper No. 76-565, July 1976.

18. J. E. Ffowcs-Williams and D. L. Hawkings, "Sound Generated by Turbulence and Surfaces in Arbitrary Motion", Phil. Trans. Roy. Soc. London Series A, Vol. 264, 1969.

19. L. J. Gutin, "On the Sound Field of a Rotating Propeller", Physi Ralisehi Jetschrift det Sowjetunion, Vol. 9, No. 1, 1936. Presented as ARC paper 3115 or NACA Tech. Memo 1195.

20. Magliozzi, B.; and Brooks, B. M., "Advanced Turbo-Prop Airplane Interior Noise Reduction Source Definition", NASA CR-159668.

21. Dittmar, J. H.; Blaha, B. J.; and Jeracki, R. J., "Tone Noise of Three Supersonic Helical Tip Speed Propellers in a Wind Tunnel at 0.8 Mach Number", NASA TM-79046, December, 1978.

22. Dittmar, J. H.; Jeracki, R. J.; and Blaha, B. J., "Tone Noise of Three Supersonic Helical Tip Speed Propellers in a Wind Tunnel", NASA TM-79167, June, 1979.

23. R. J. Swallow and R. A. Aiello "NASA Lewis 8-by 6- foot Supersonic Wind Tunnel", NASA Lewis Research Center, NASATMX-71542, May 1974.

REFERENCES (Continued)

24. R. M. Reynolds, R. I. Sammonds and G. C. Kenyon, "An Investigation of a Four Blade Single-Rotation Propeller in Combination with an NACA 2-Series, D-Type Cowling at Mach Numbers up to 0.83", NACA RM A53B06, April 13, 1953.

25. H. Glauert, "Airplane Propellers, Body and Wing Interference", Volume IV, Division 2, Chapter VIII, Aerodynamic Theory, W. F. Durand, editor Julius Springer (Berlin), 1935 (Dover reprint 1963).
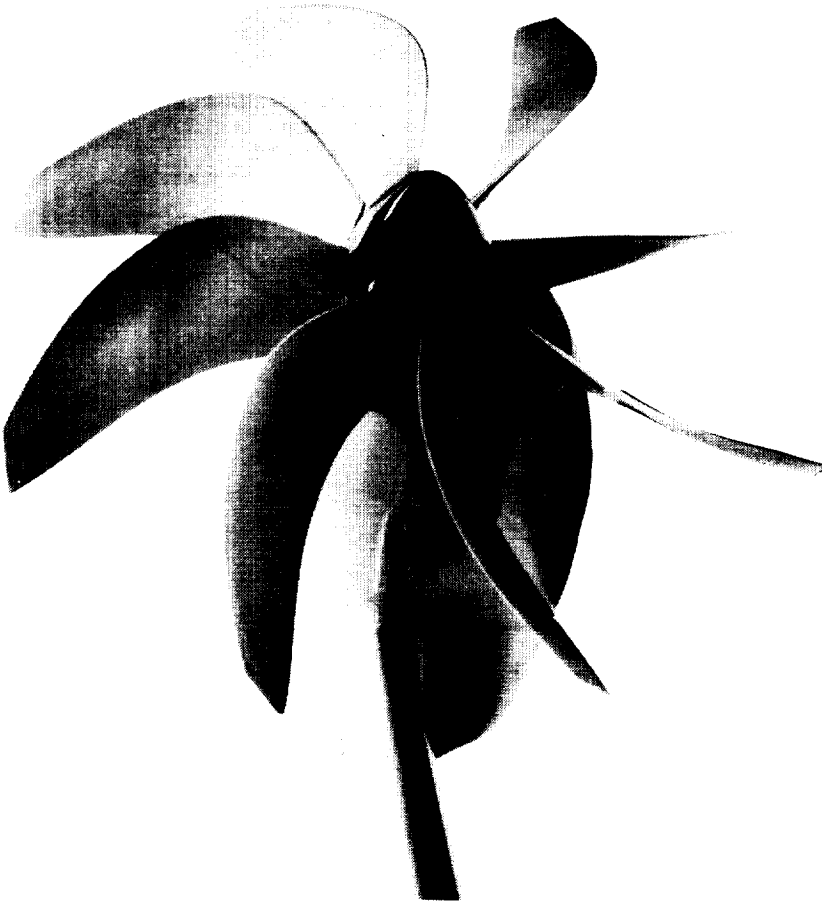
FIGURE 1. SR-3 PROP-FAN INSTALLATION

```
          ┌─────────────────────────────────────────────┐
          │   OPTIMUM AERO LOADING BASED ON GOLDSTEIN    │
          └─────────────────────────────────────────────┘


┌──────────────────────────┐        ┌──────────────────────────────┐
│      ROOT SECTIONS       │        │        OUTER BLADE           │
│                          │───────▶│                              │
│   GAP/CHORD < 1.0        │        │   HAMILTON STANDARD          │
│                          │        │   GOLDSTEIN THEORY           │
│   TURBOFAN ANALYSIS      │◀───────│                              │
│     STREAMLINE (A 654)   │        │   2D COMPRESSIBLE AIRFOIL    │
│     CASCADE PROGRAM      │        │     SWEEP                     │
│                          │        │     CASCADE                  │
│                          │        │     TIP ASPECT RATIO         │
└──────────────────────────┘        └──────────────────────────────┘


                  ┌──────────────────────┐
                  │     AERODYNAMIC      │
                  │    CONFIGURATION     │
                  └──────────────────────┘
```
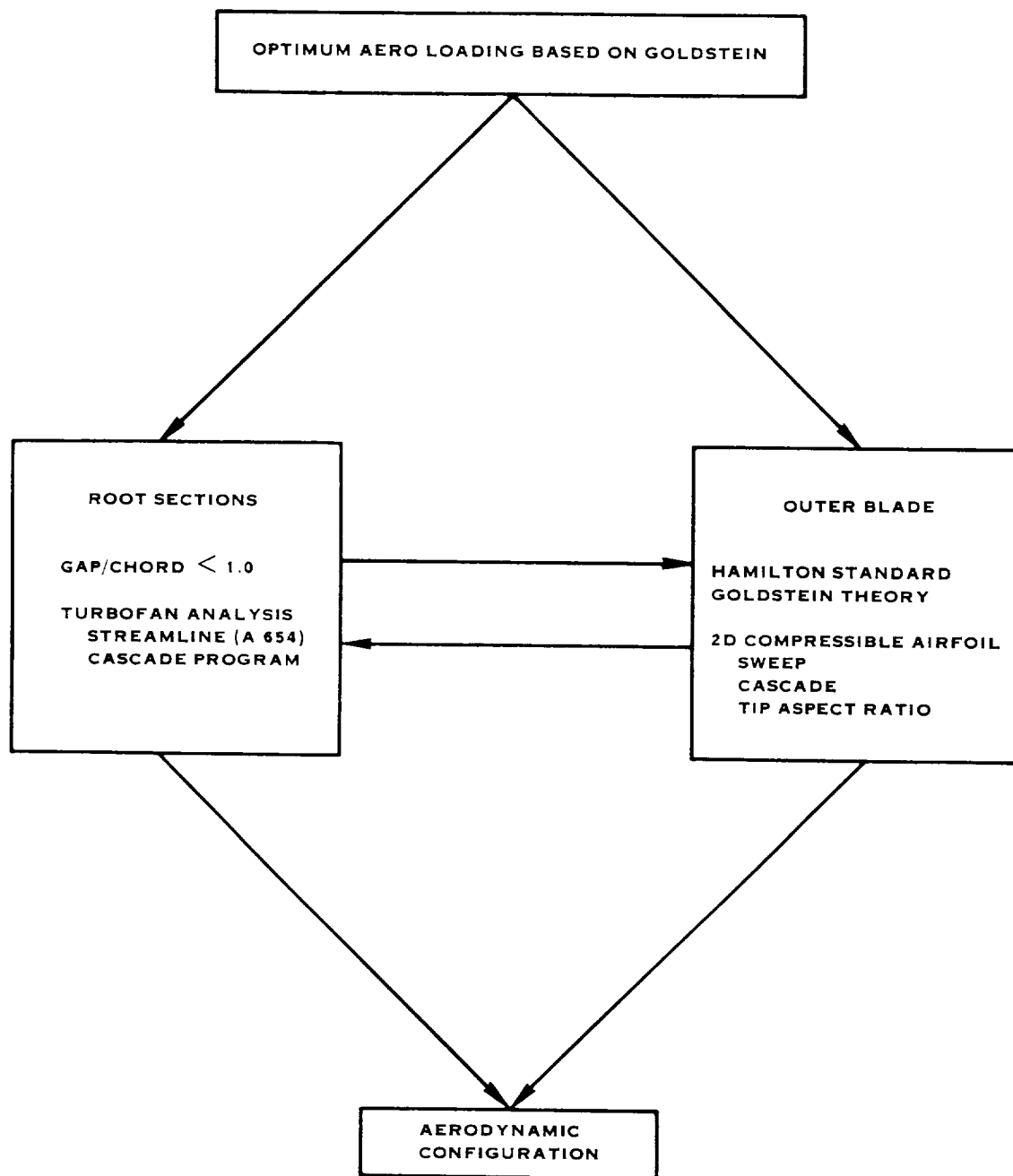
FIGURE 2.   AERODYNAMIC DESIGN ANALYSIS
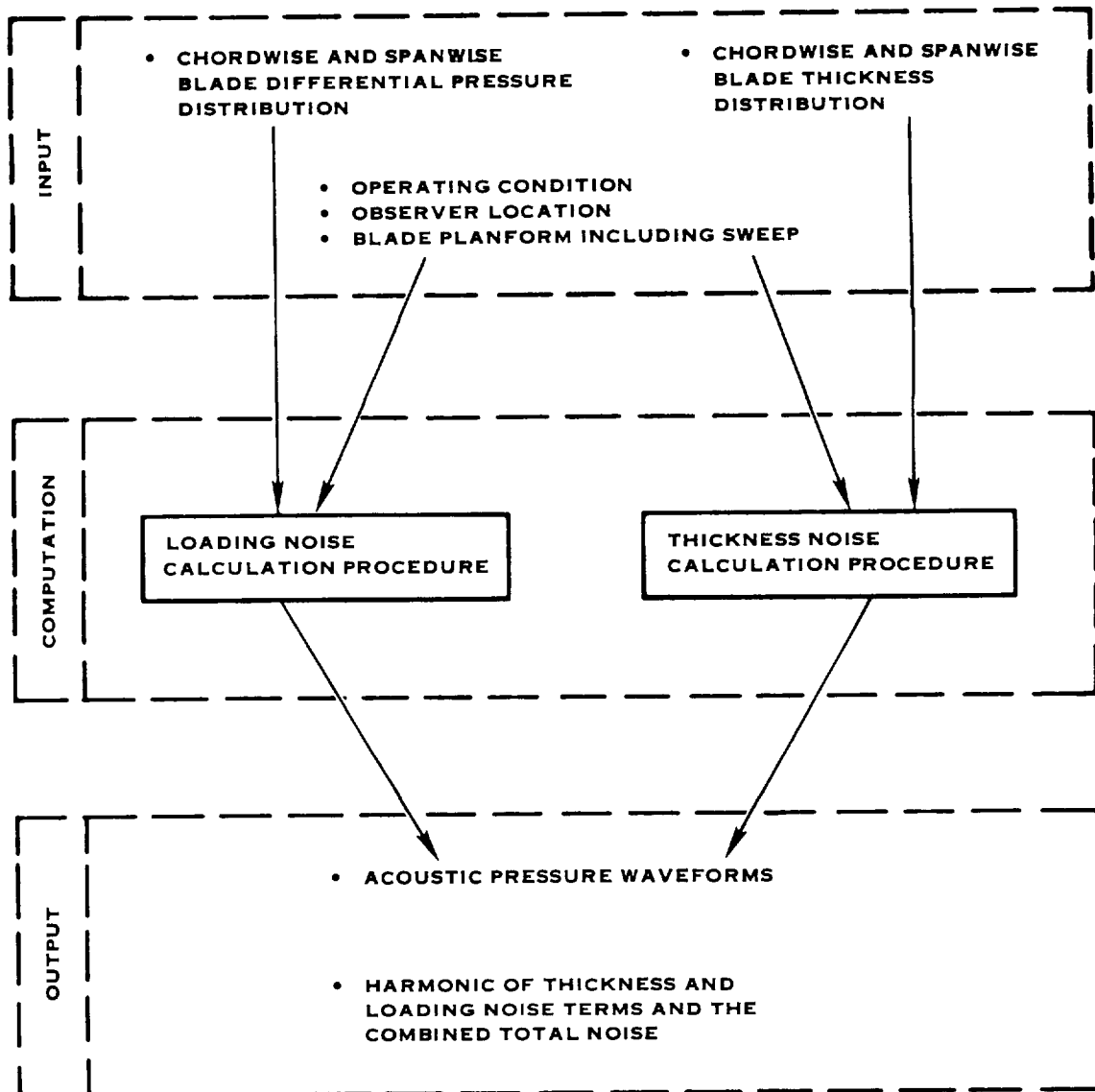
FIGURE 3.   PROP-FAN NOISE PREDICTION PROCEDURE
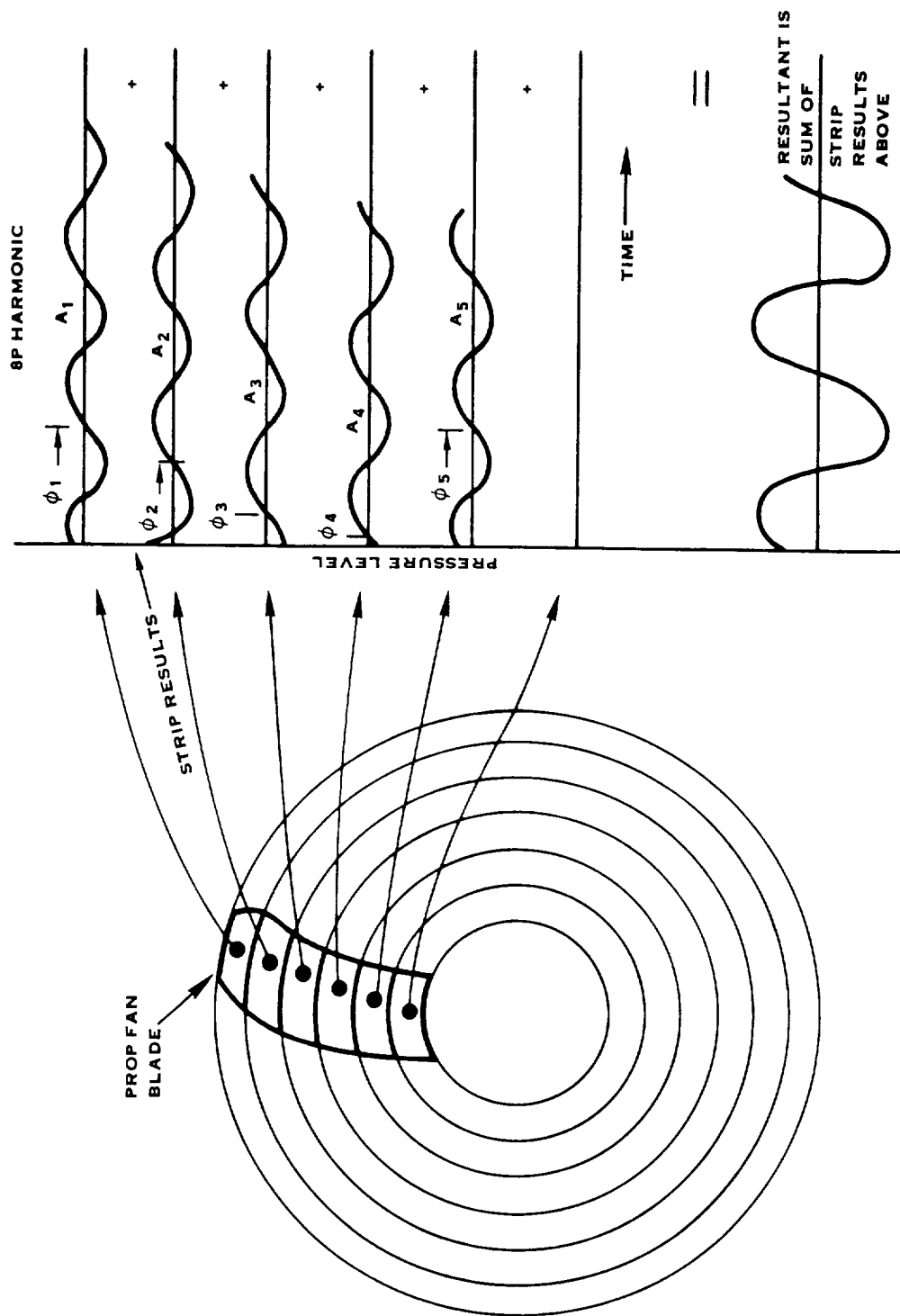
FIGURE 4.   ACOUSTIC STRIP ANALYSIS CONCEPT

40
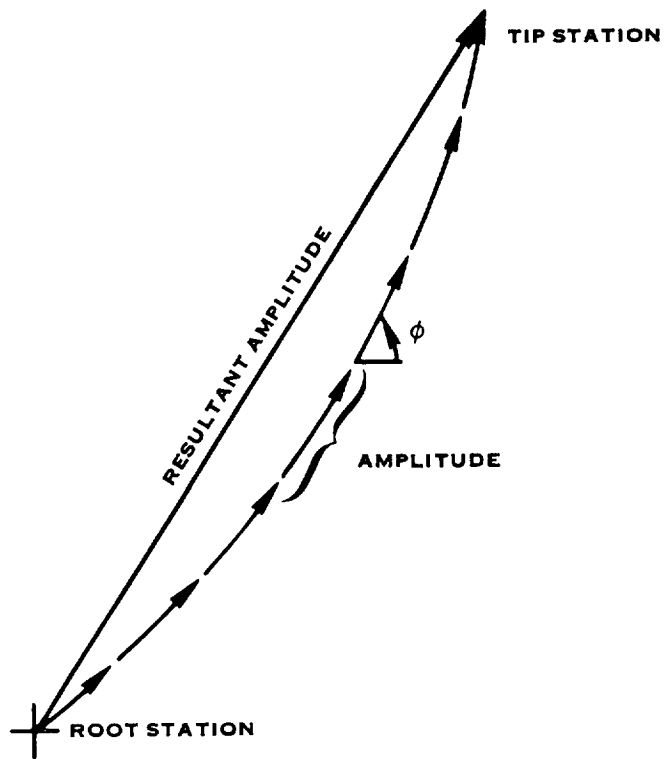
(A)   POOR CANCELLATION OF UNSWEPT
      OR SLIGHTLY SWEPT PROP-FAN
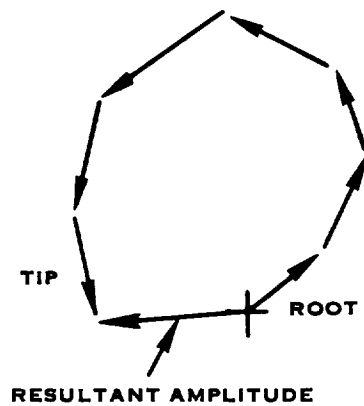
(B)   STRONG CANCELLATION OF
      ACOUSTICALLY SWEPT PROP-FAN

FIGURE 5.   PHASE CANCELLATION EFFECTS

41
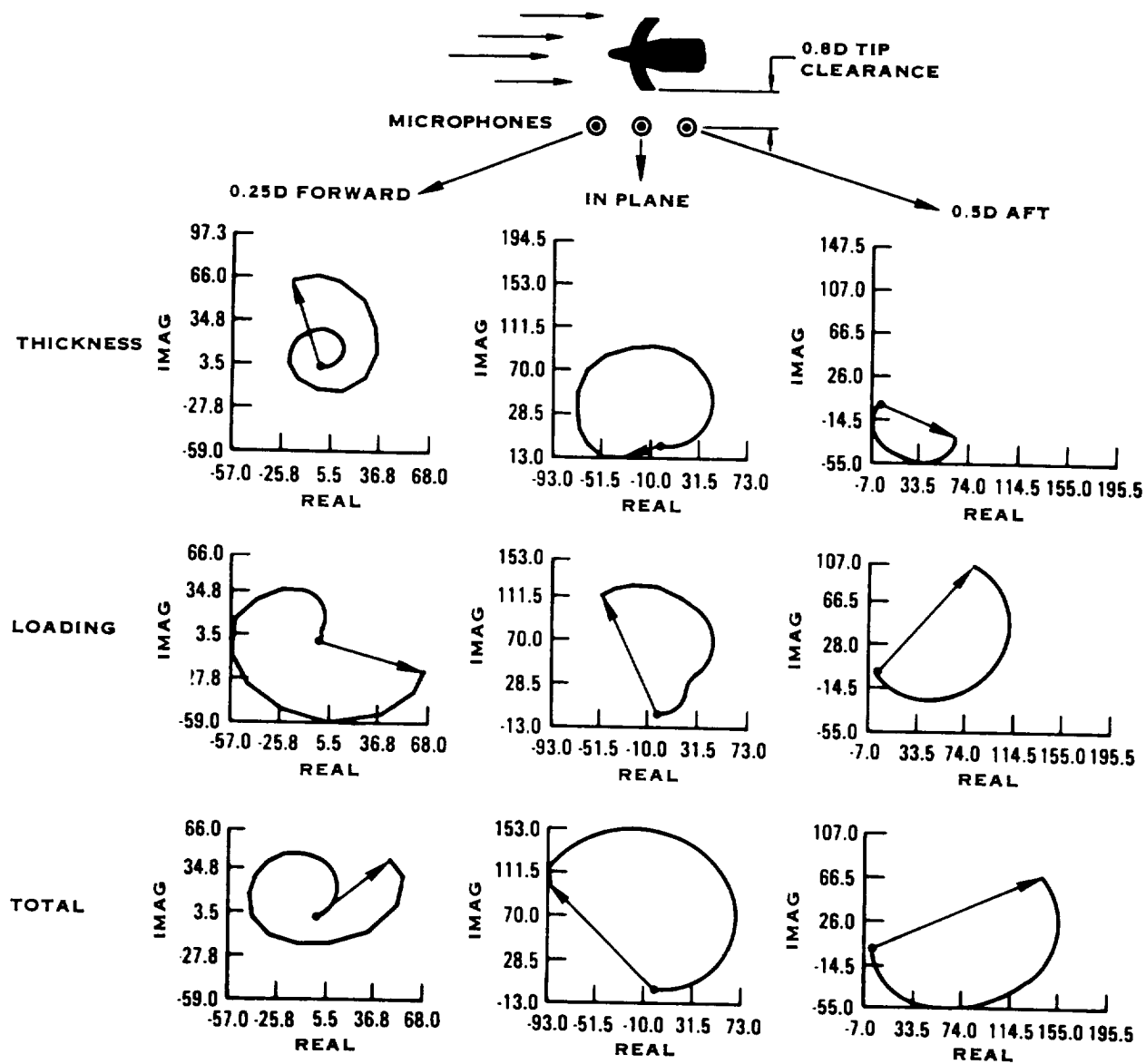
FIGURE 6.   BLADE PASSAGE FREQUENCY LEVEL SR3 PHASE PLOTS

42
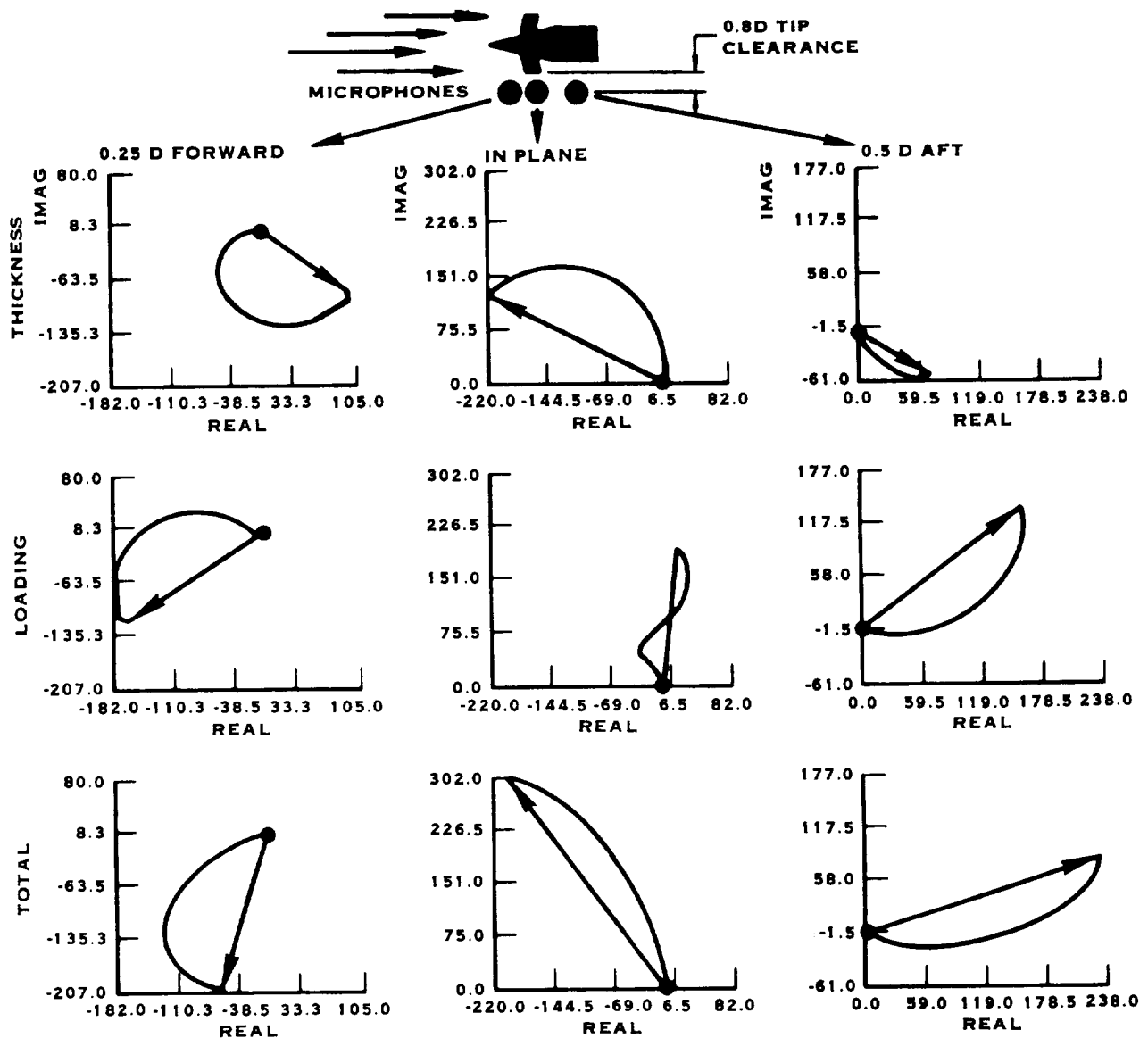
FIGURE 7. BLADE PASSAGE FREQUENCY HARMONIC LEVEL
SR-1 PHASE PLOTS

43
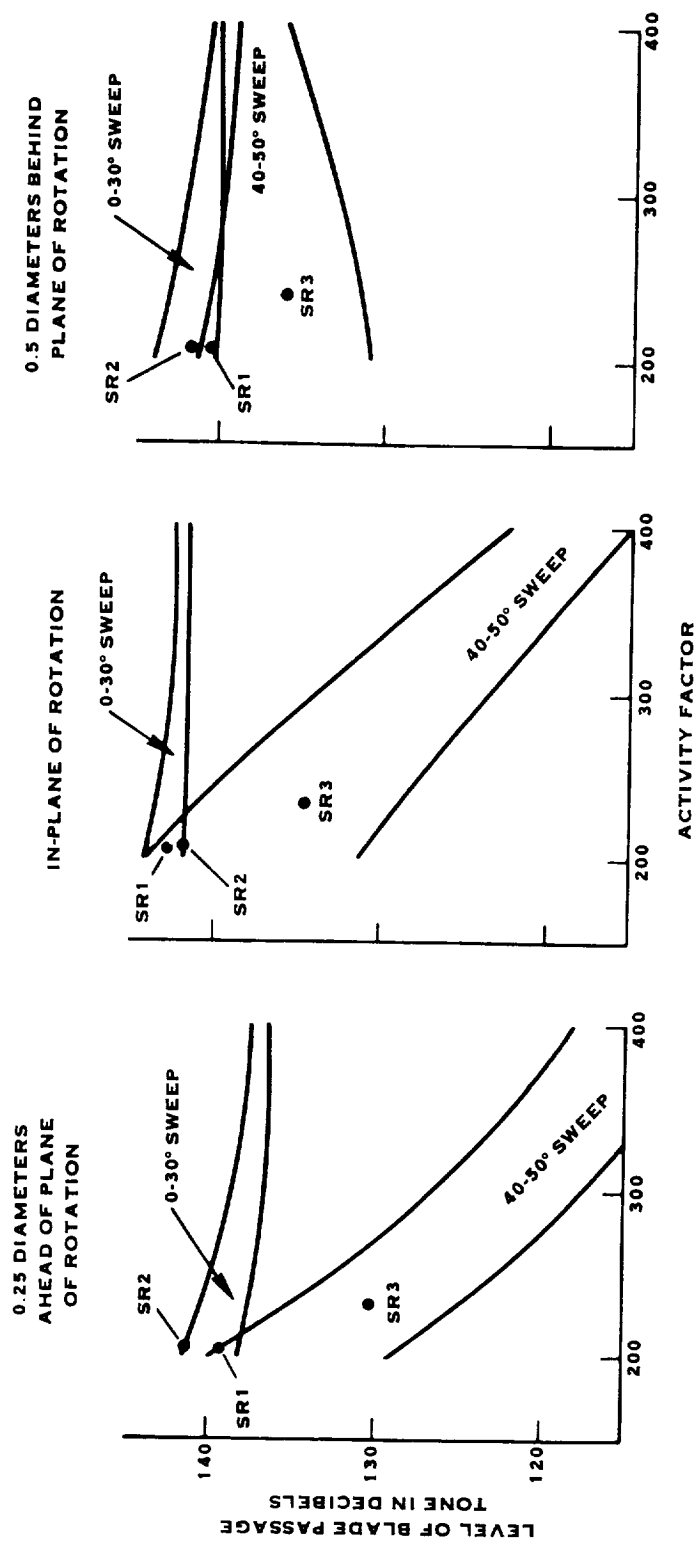
FIGURE 8. PROP-FAN NOISE TRENDS AS A FUNCTION OF ACTIVITY
FACTOR AND TIP SWEEP

44

BLADE PASSAGE FREQUENCY
0.8 MN CRUISE
10667 METER (35000 FT) ALTITUDE
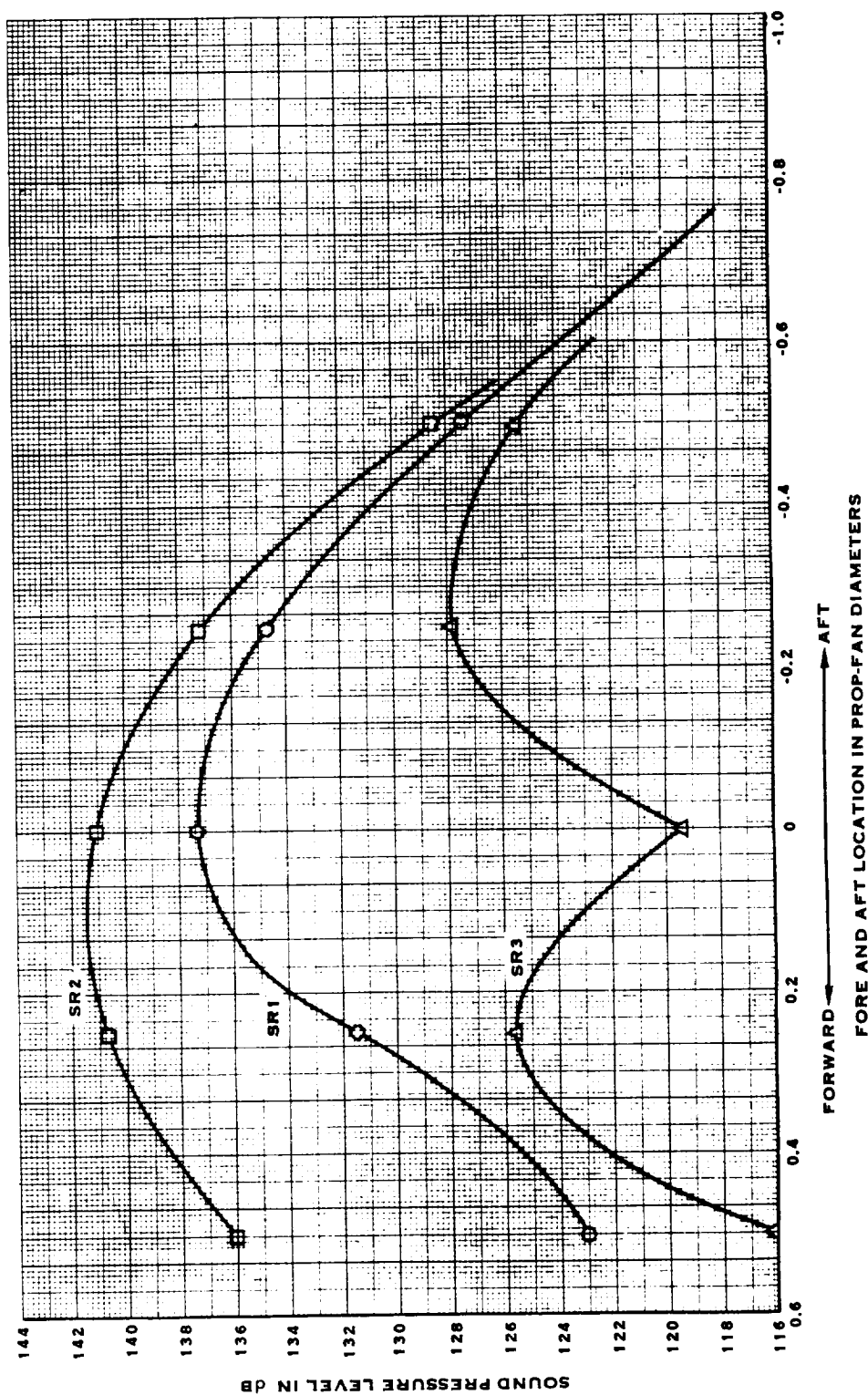
FIGURE 9. EFFECT OF BLADE SHAPE ON THICKNESS NOISE

BLADE PASSAGE FREQUENCY
0.8 MN CRUISE
10667 METER (35000 FT.) ALTITUDE
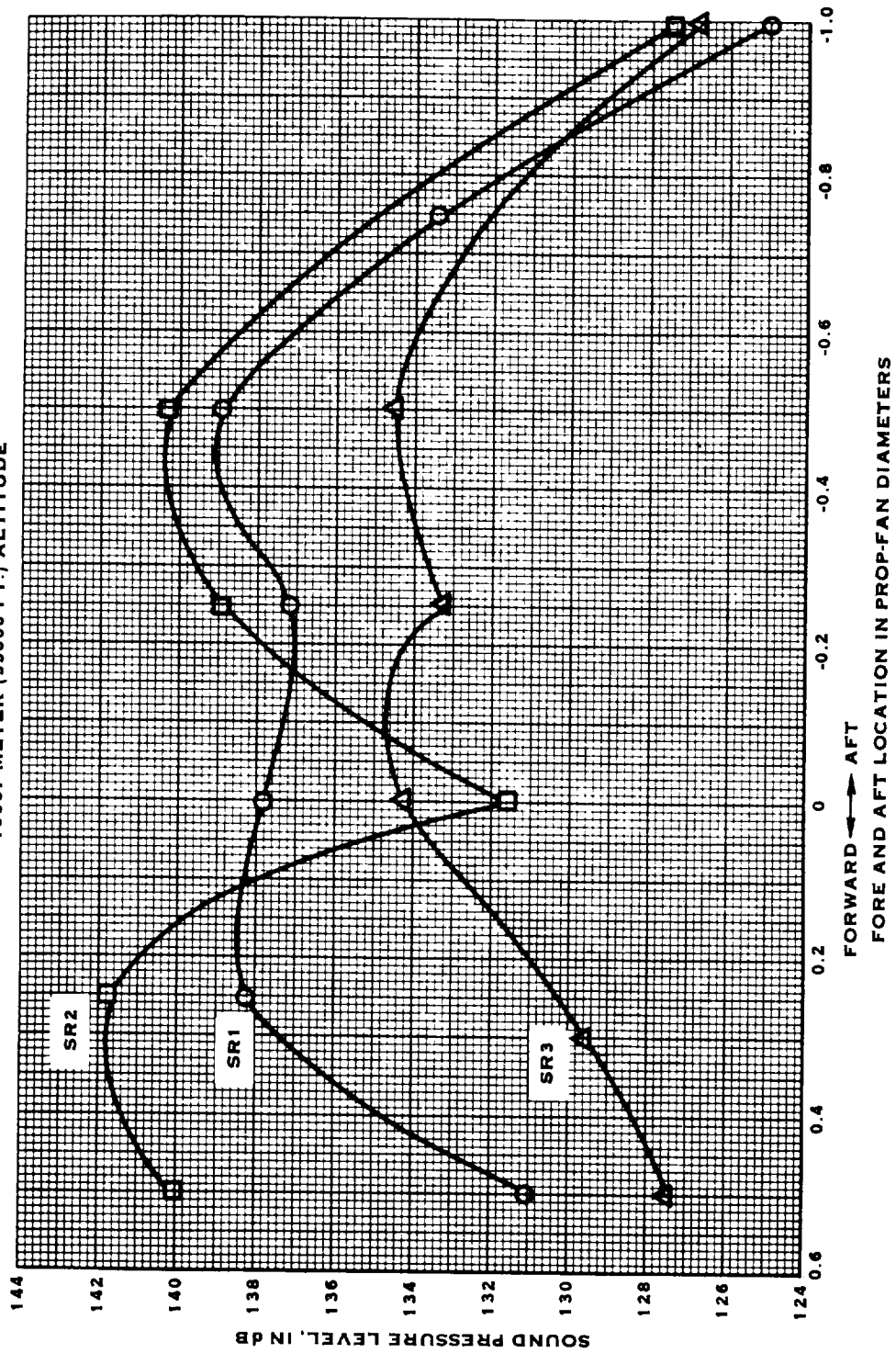
FIGURE 10. EFFECT OF BLADE SHAPE ON LOADING NOISE

BLADE PASSAGE FREQUENCY
0.8 MN CRUISE
10667 METER (35000 FT) ALTITUDE
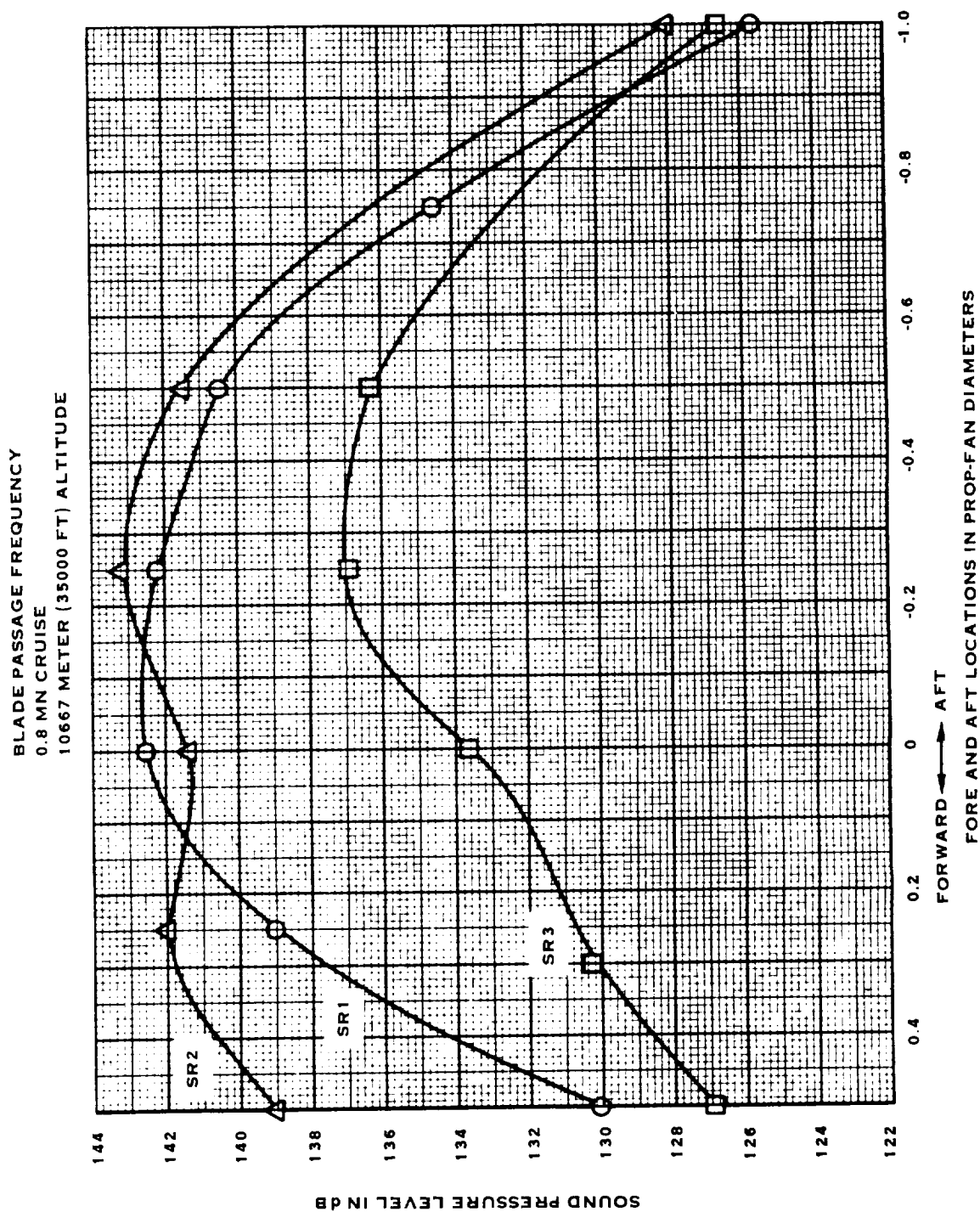
FIGURE 11. TOTAL NOISE COMPARISON OF THE THREE MODEL BLADES
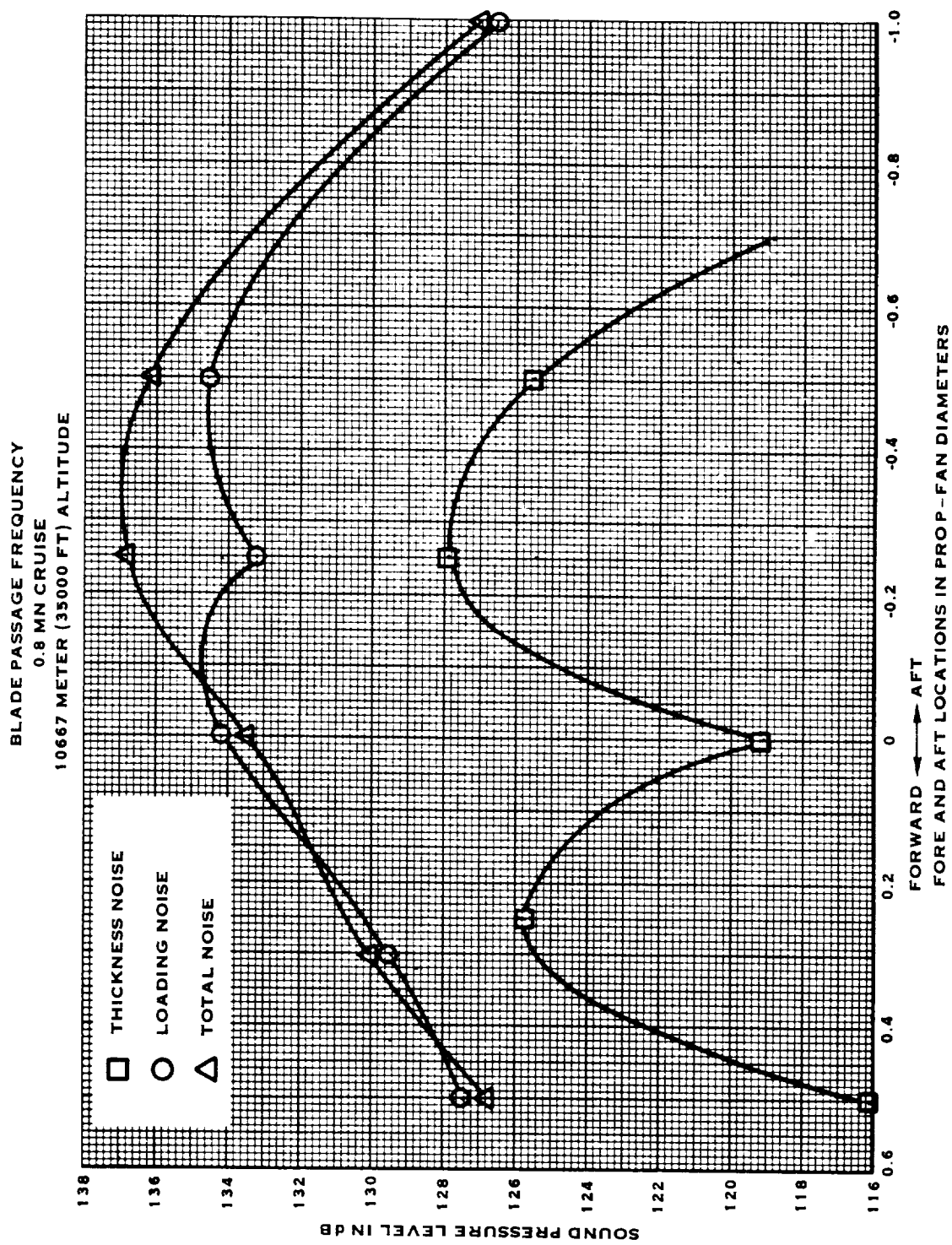
FIGURE 12. SR3 BLADE NOISE

48
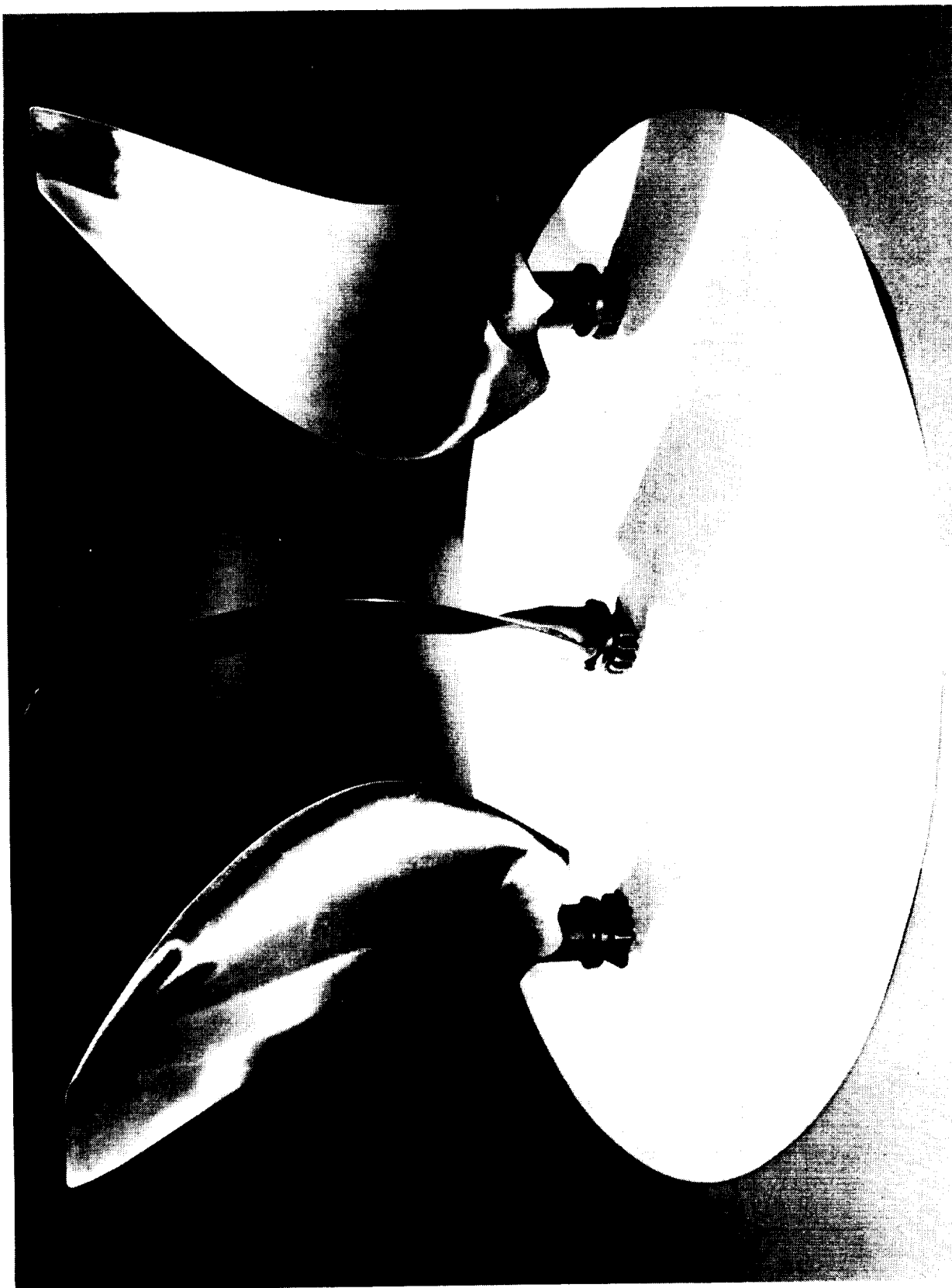
FIGURE 13. SR-3 MODEL BLADE

49
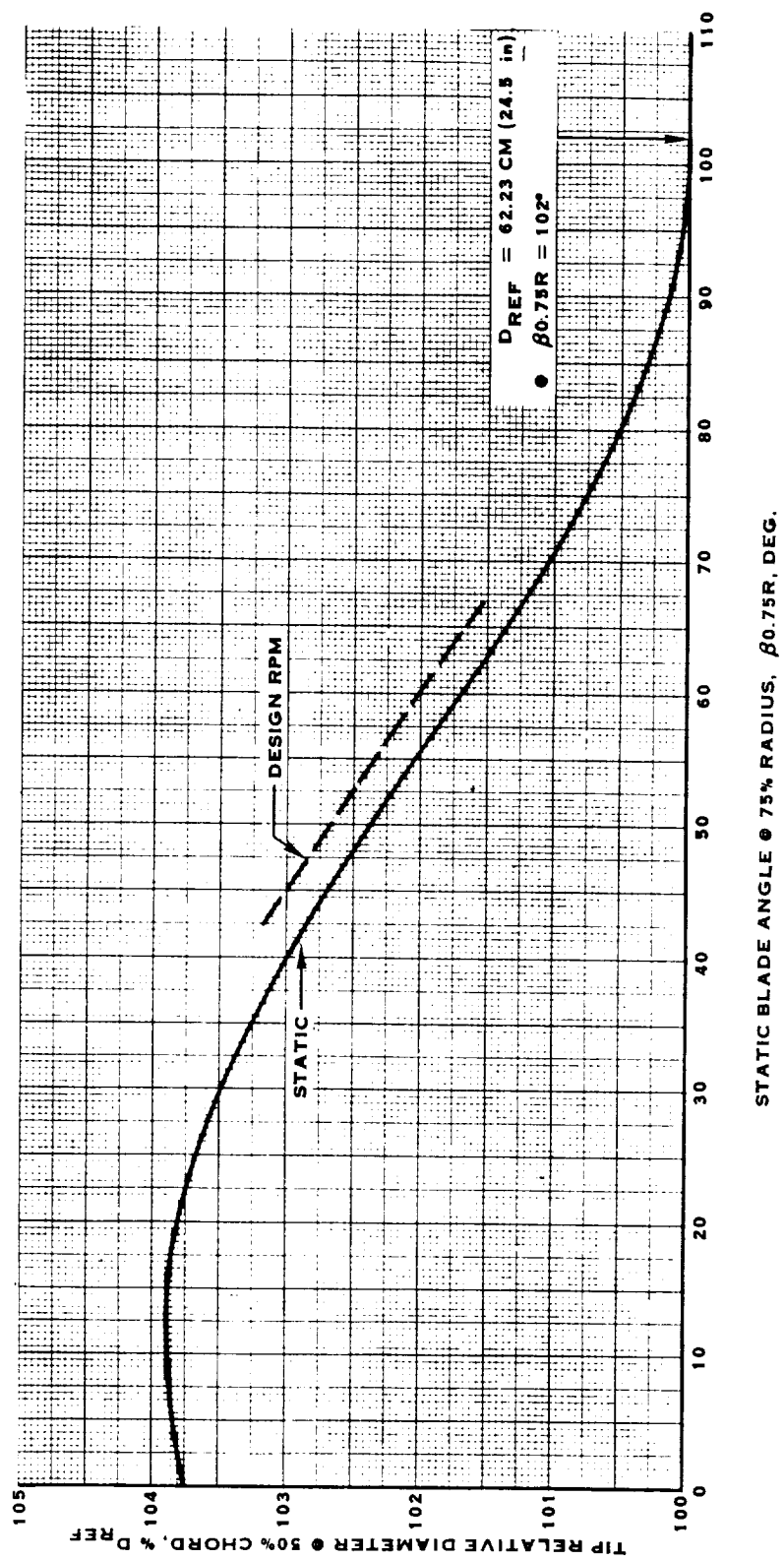
FIGURE 14. VARIATION OF TIP RELATIVE DIAMETER WITH BLADE ANGLE

STATIC BLADE ANGLE @ 75% RADIUS, $\beta_{0.75R}$, DEG.

TIP RELATIVE DIAMETER @ 50% CHORD, % D_{REF}

D_{REF} = 62.23 CM (24.5 in)

$\beta_{0.75R}$ = 102°

DESIGN RPM

STATIC
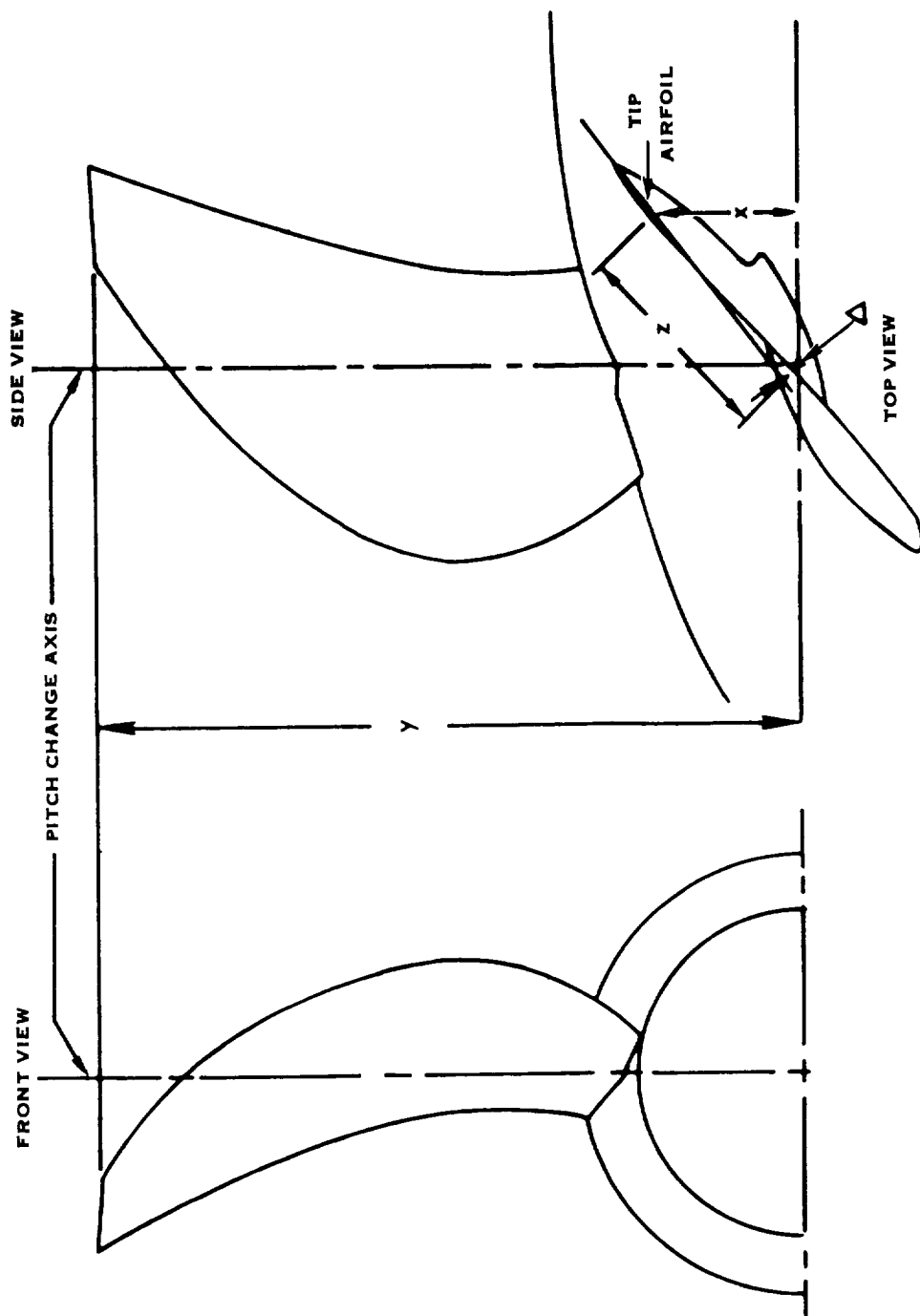
FIGURE 15. THREE VIEW SKETCH OF SR3 SHOWING RELATIVE LOCATION OF TIP AIRFOIL AND PITCH CHANGE AXIS

8 BLADES/235AF/0.241 CLI
0.62 METER (24.5 INCH) DIAMETER
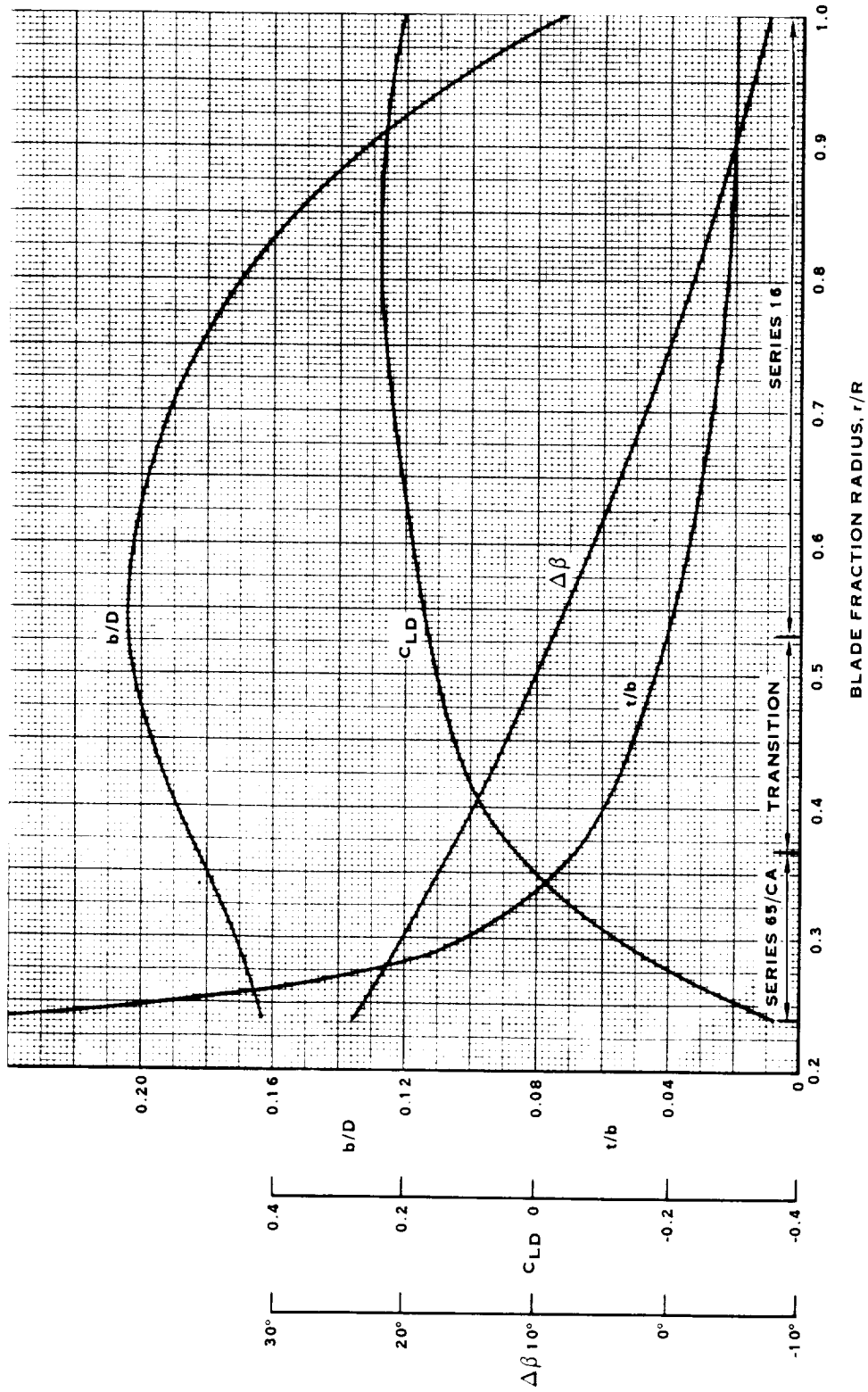
FIGURE 16. BLADE CHARACTERISTICS

52
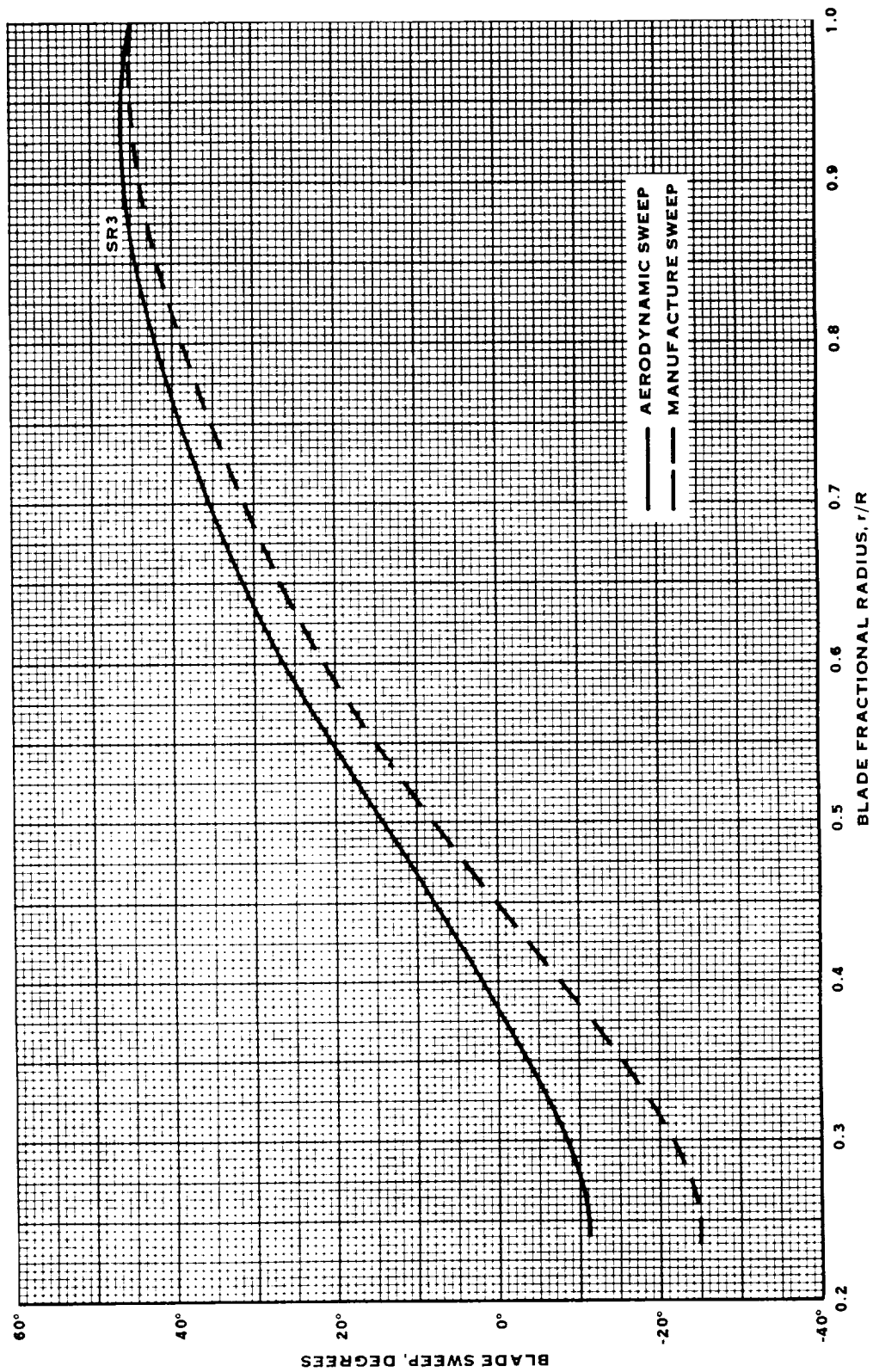
FIGURE 17. VARIATION OF BLADE SWEEP DISTRIBUTION WITH BLADE FRACTIONAL RADIUS

53

TIP AIR FOIL

STACKED VIEW

PITCH CHANGE AXIS

LEADING EDGE

DEVELOPED PLANFORM
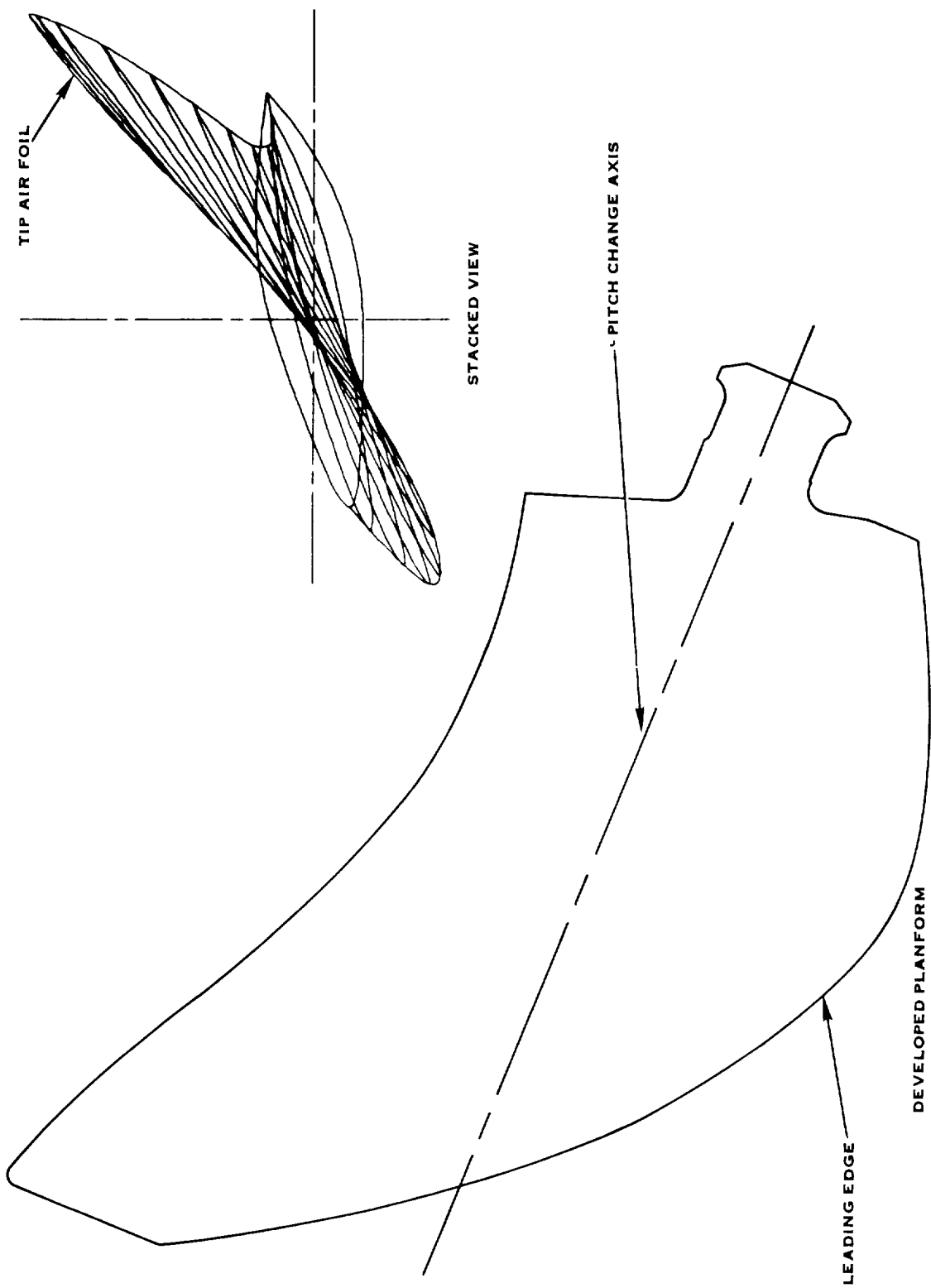
FIGURE 18. DEVELOPED PLANFORM AND STACKED VIEW

54
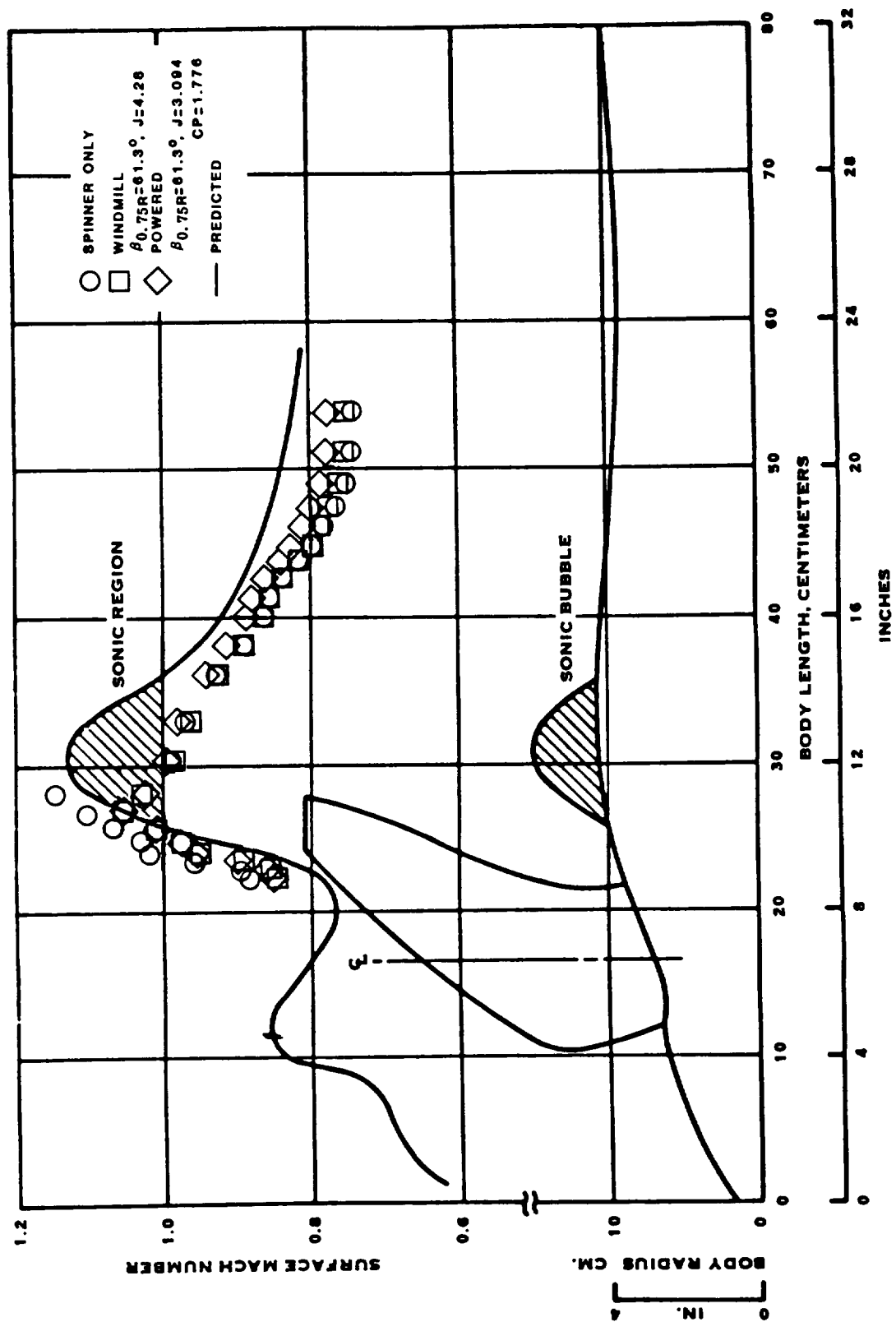
FIGURE 19. NACELLE SURFACE MACH NUMBER DISTRIBUTION
FREESTREAM MACH NUMBER 0.80

55
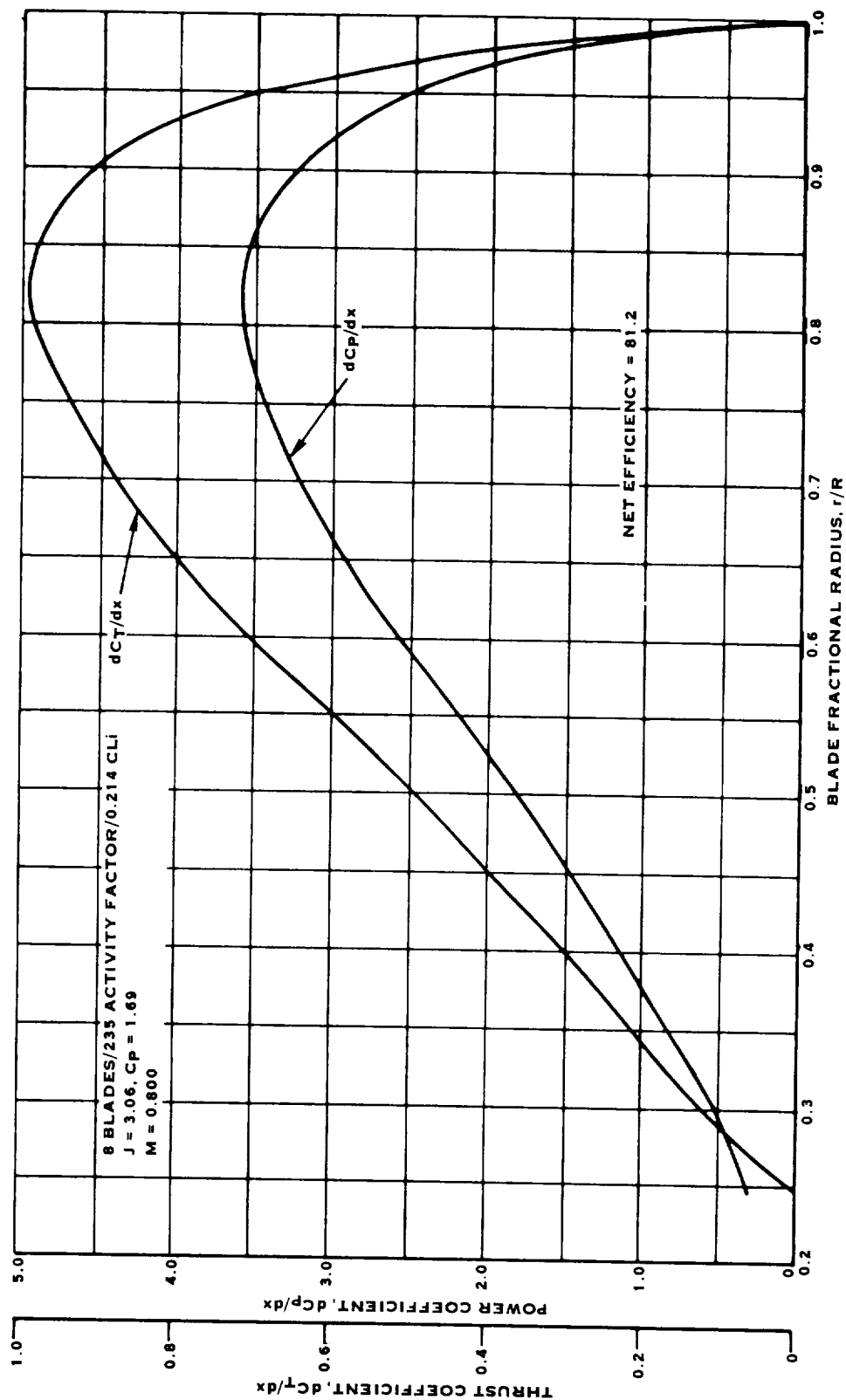
FIGURE 20. VARIATION OF CALCULATED THRUST AND POWER COEFFICIENTS WITH BLADE FRACTIONAL RADIUS

56

FIGURE 21. PROP-FAN INSTALLATION IN THE 8 X 6 FOOT TUNNEL

STRUT MOUNTED
LOAD CELL

WIND SCREEN

AXISMMETRIC NACELLE (GROUNDED)

ROTATING THRUST
AND TORQUE METER

BLADES AND
SPINNER (METRIC)
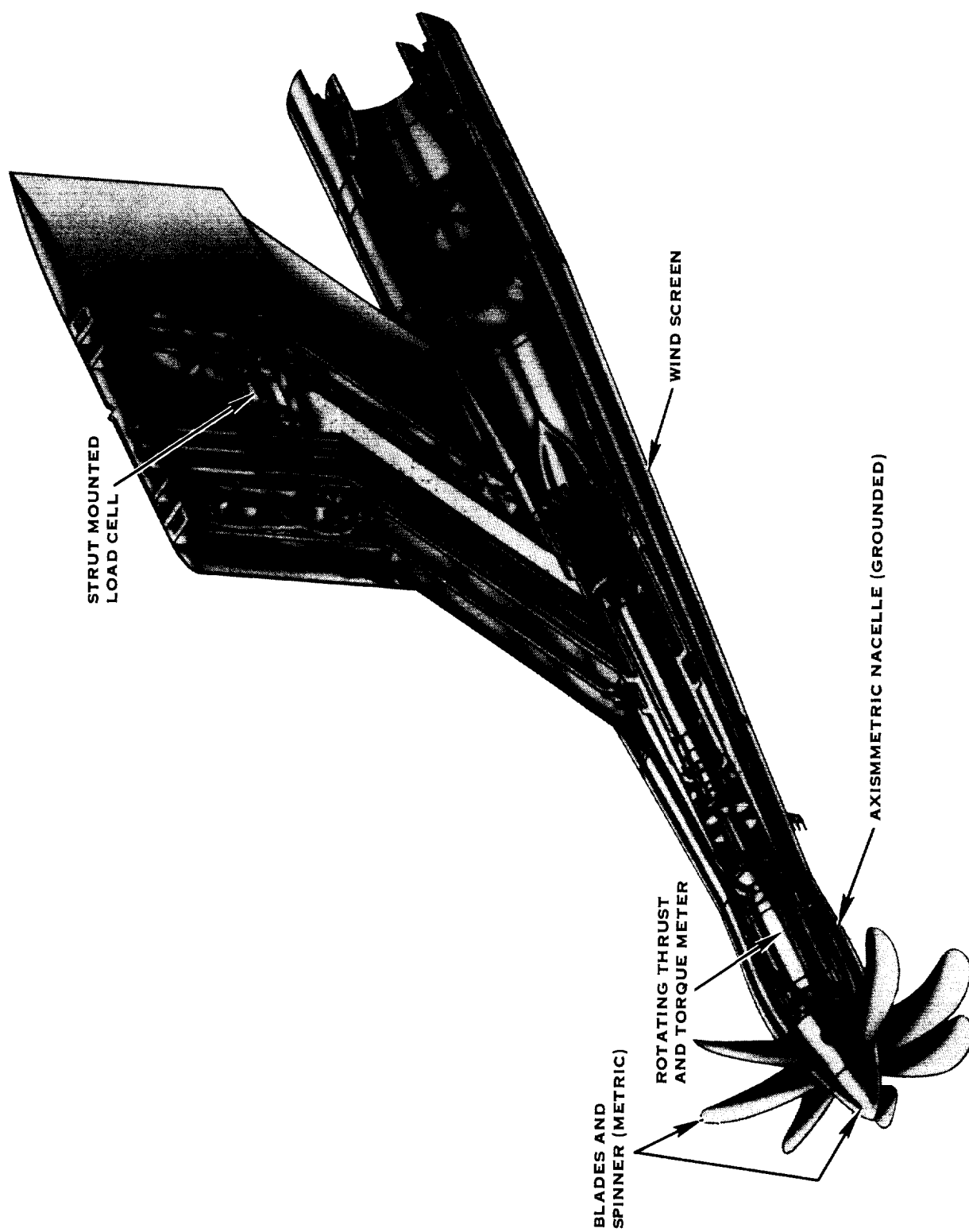
FIGURE 22. CUTAWAY VIEW OF THE PROPELLER TEST RIG (PTR)

58

COVER USED FOR
SPINNER DRAG AND
WINDMILL DRAG RUNS

STATICS ON
THE BASE
OF THE PTR

A-A

TOTALS IN THE
TURBINE EXIT DUCT

STATICS DISTRIBUTED
WITHIN WINDSCREEN CAVITY

STATICS BEHIND
THE INTERNAL SEAL

A) INTERNAL
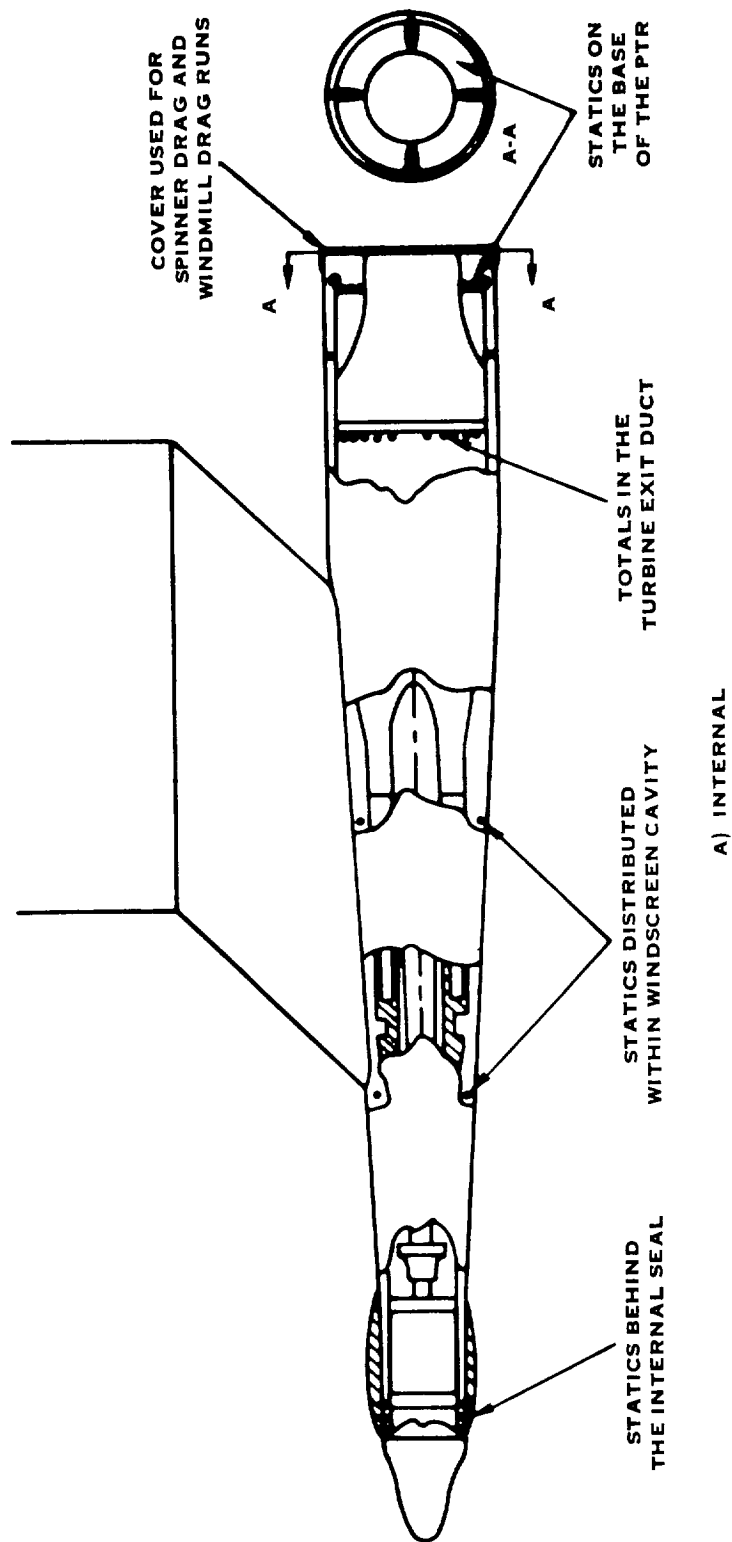
FIGURE 23. PTR STATIC PRESSURE LOCATIONS
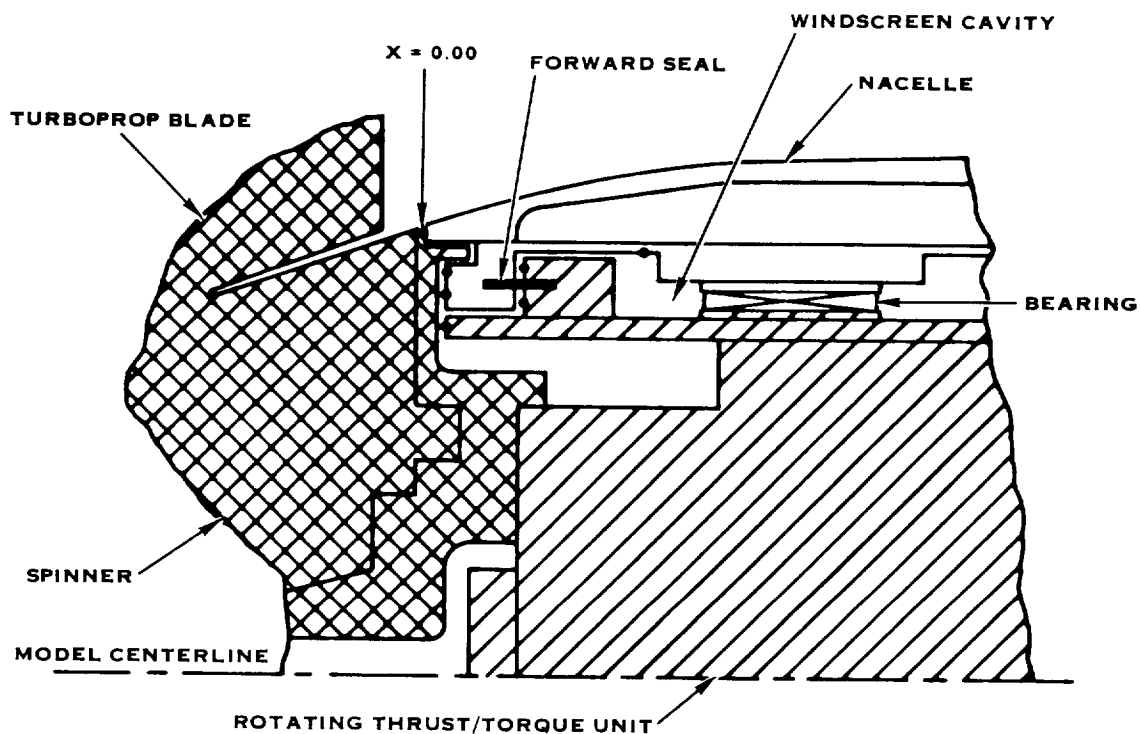
B) NACELLE AND SPINNER FACE

SPINNER
STATICS

$\dfrac{R}{R_N}$	θ
0.6835	0,180
*0.7353	0,180
0.7381	0,180
0.7861	0,180
0.8673	0,90,180,270

*BELOW FORWARD SEAL

NACELLE
STATICS

$\dfrac{X}{R_N}$	$\dfrac{Y}{R_N}$
0.0241	0.8684
0.0749	0.8848
0.1299	0.9010
0.1880	0.9170
0.2547	0.9326
0.3345	0.9480
0.4276	0.9631
0.5520	0.9780
0.7598	0.9927
1.0149	1.0000
1.2876	0.9949
1.4793	0.9848
1.6299	0.9745
1.7644	0.9642
1.8823	0.9537
1.9924	0.9431
2.0954	0.9323
2.2057	0.9215
2.3264	0.9105
2.4667	0.8994
2.6586	0.8882
2.9184	0.8768

FIGURE 23. PTR STATIC PRESSURE LOCATIONS
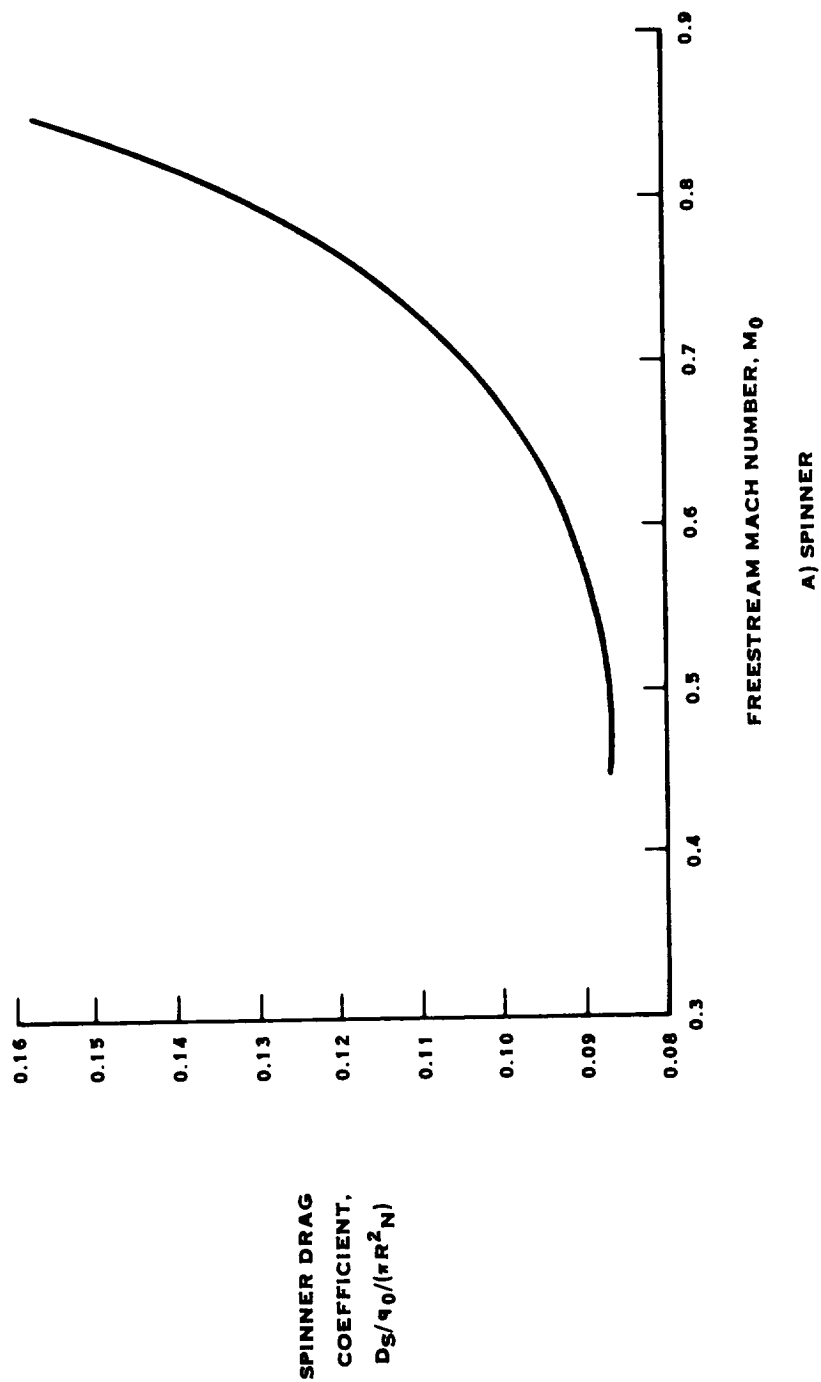
FIGURE 24. DRAG COEFFICIENTS WITHOUT BLADES
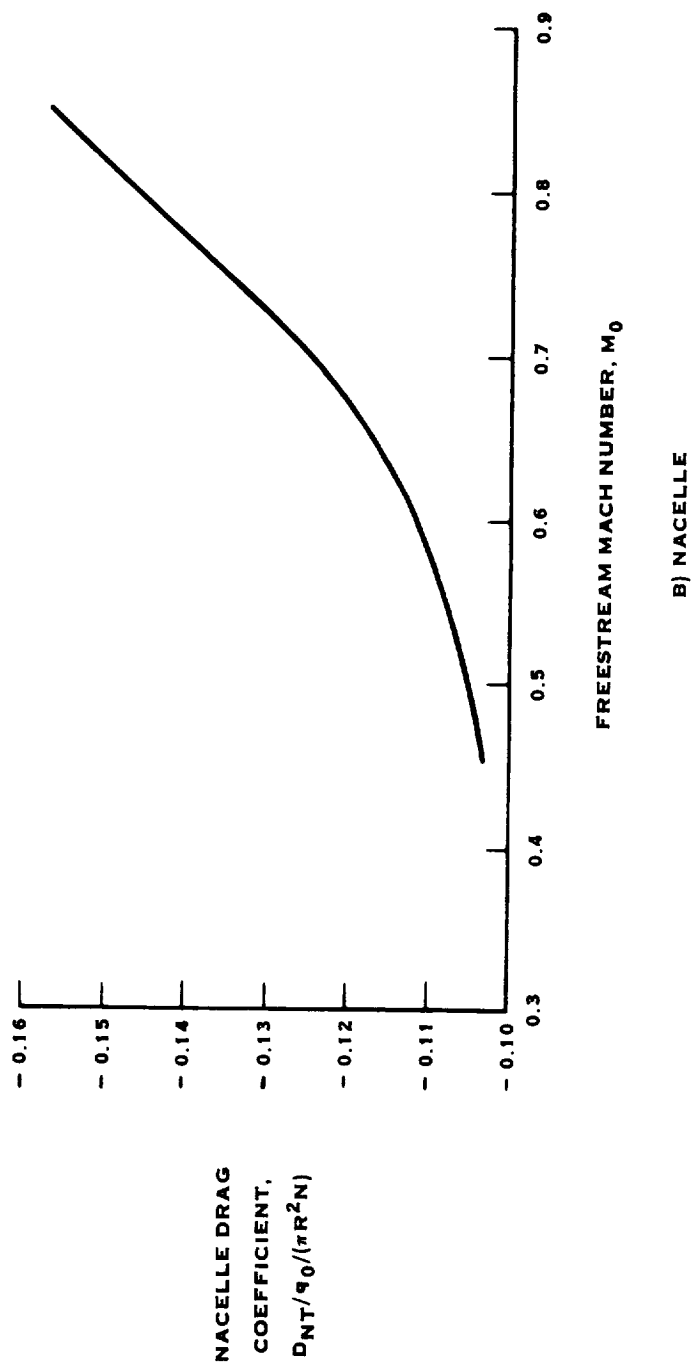
FIGURE 24. DRAG COEFFICIENTS WITHOUT BLADES
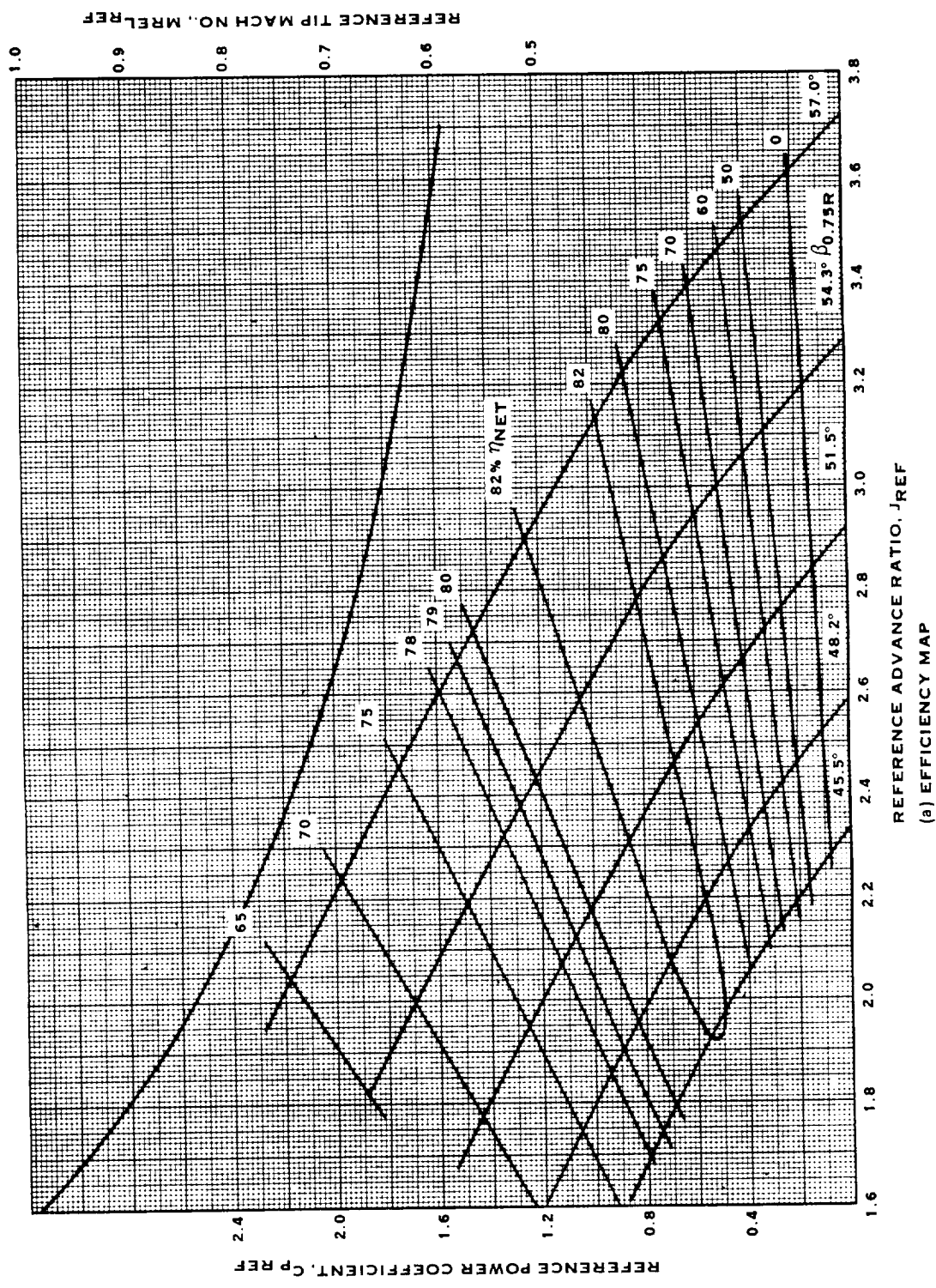
FIGURE 25. PROPELLER PERFORMANCE AT Mo = 0.45

(a) EFFICIENCY MAP

63

REFERENCE ADVANCE RATIO, J_{REF}

(b) POWER COEFFICIENT

FIGURE 25. (CONTINUED)

64

REFERENCE ADVANCE RATIO, J_{REF}
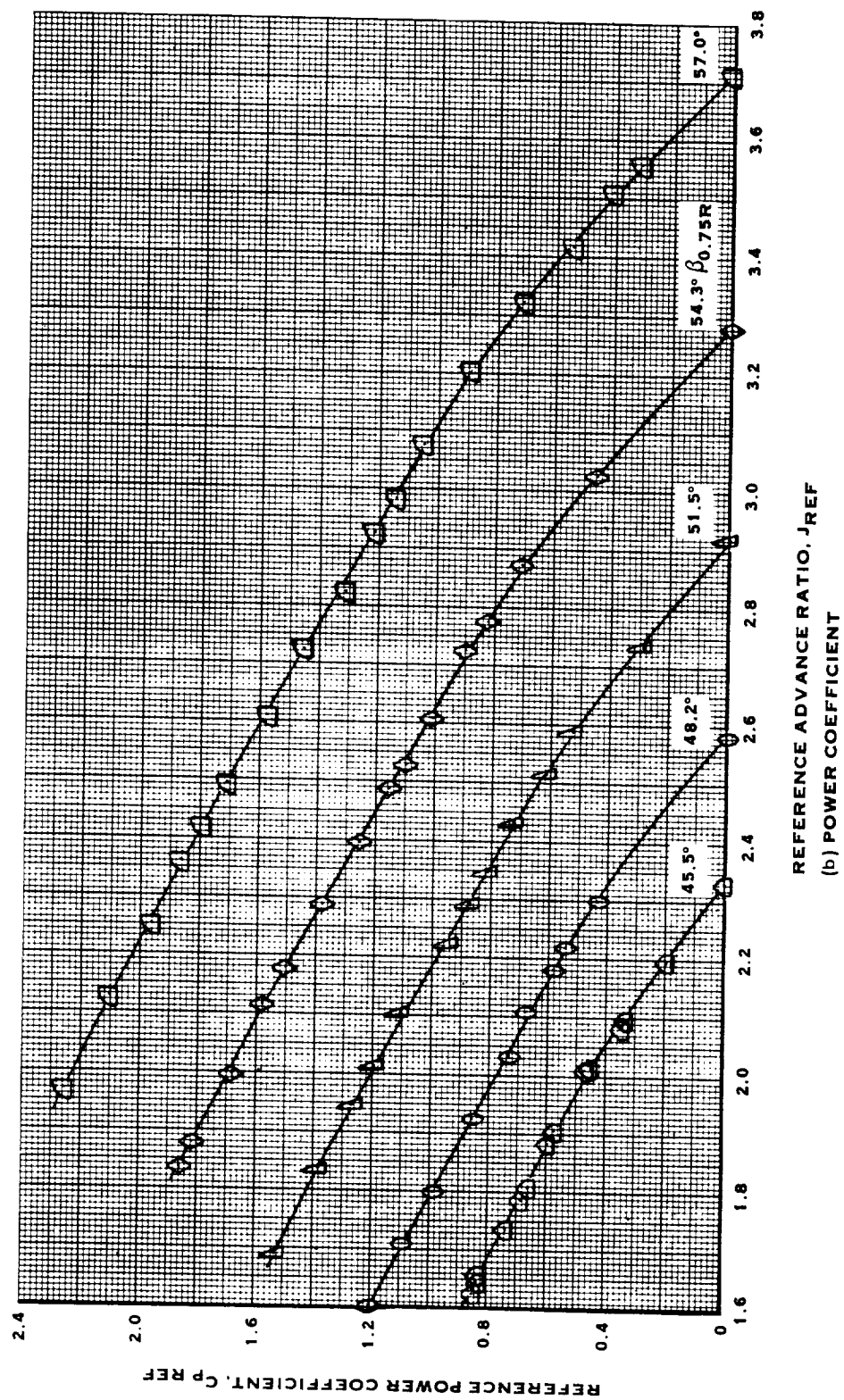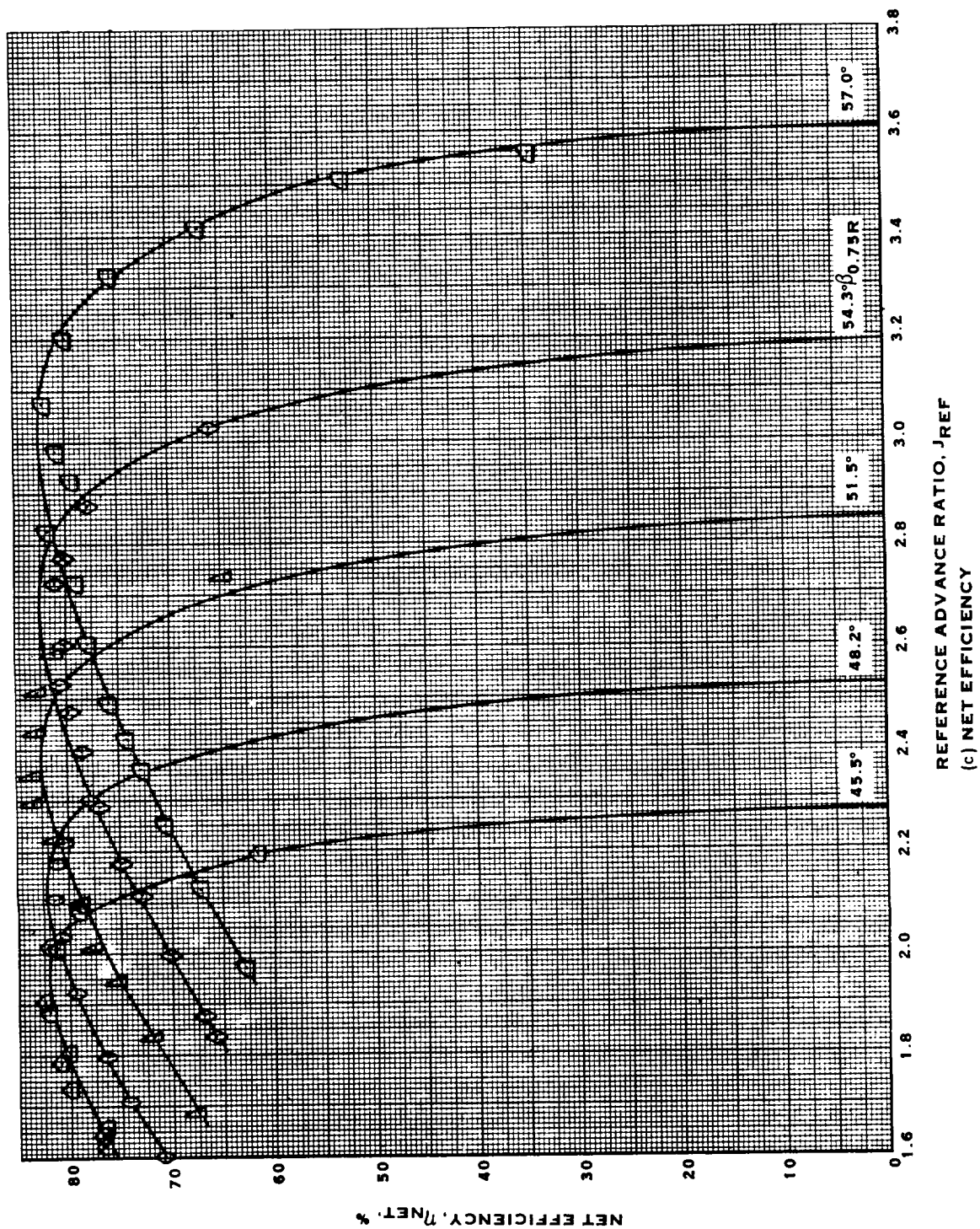
(c) NET EFFICIENCY

FIGURE 25. (CONTINUED)
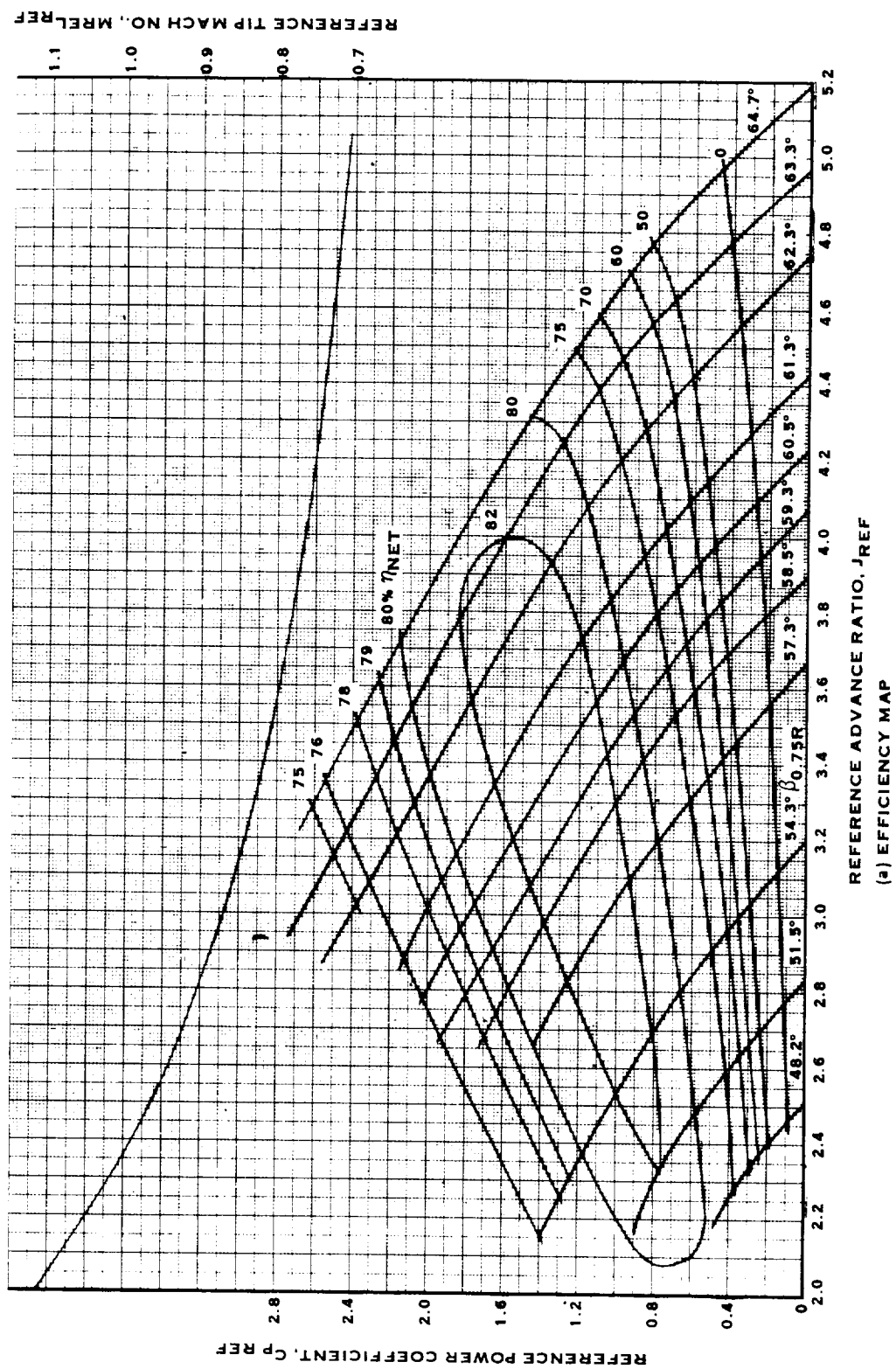
FIGURE 26. PROPELLER PERFORMANCE AT Mo = 0.60

(a) EFFICIENCY MAP

REFERENCE ADVANCE RATIO, J_{REF}

REFERENCE POWER COEFFICIENT, $C_{P\ REF}$

REFERENCE TIP MACH NO., $M_{REL,REF}$

66

REFERENCE ADVANCE RATIO, J_{REF}

(b) POWER COEFFICIENT

FIGURE 26. (CONTINUED)

67

REFERENCE ADVANCE RATIO, J_{REF}

(c) NET EFFICIENCY

NET EFFICIENCY, η_{NET}, %

FIGURE 26. (CONTINUED)

68

REFERENCE ADVANCE RATIO, J_{REF}

(d) NET EFFICIENCY FAIRING

FIGURE 26. (CONTINUED)

69

FIGURE 27. PROPELLER PERFORMANCE AT Mo = 0.70
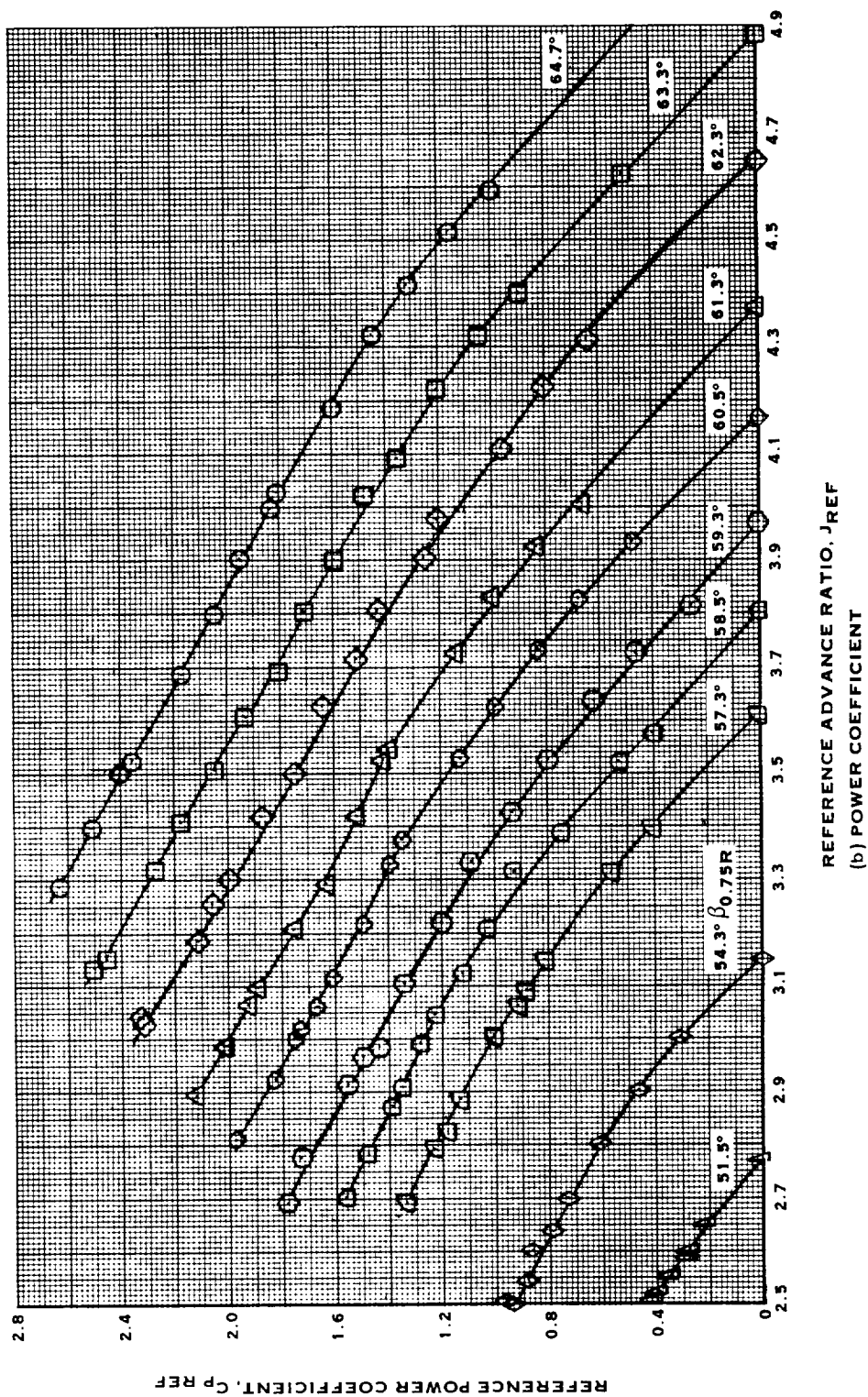
(a) EFFICIENCY MAP

REFERENCE ADVANCE RATIO, J_{REF}

REFERENCE POWER COEFFICIENT, $C_{P\,REF}$

REFERENCE TIP MACH NO., $M_{REL,REF}$

70

REFERENCE ADVANCE RATIO, J_{REF}

(b) POWER COEFFICIENT

FIGURE 27. (CONTINUED)

71

REFERENCE ADVANCE RATIO, J_{REF}

(c) NET EFFICIENCY

FIGURE 27. (CONTINUED)

NET EFFICIENCY, η_{NET}, %

72

(d) NET EFFICIENCY FAIRING

FIGURE 27. (CONTINUED)

REFERENCE TIP MACH NO., MREL,REF

REFERENCE POWER COEFFICIENT, $C_{P\ REF}$

REFERENCE ADVANCE RATIO, J_{REF}
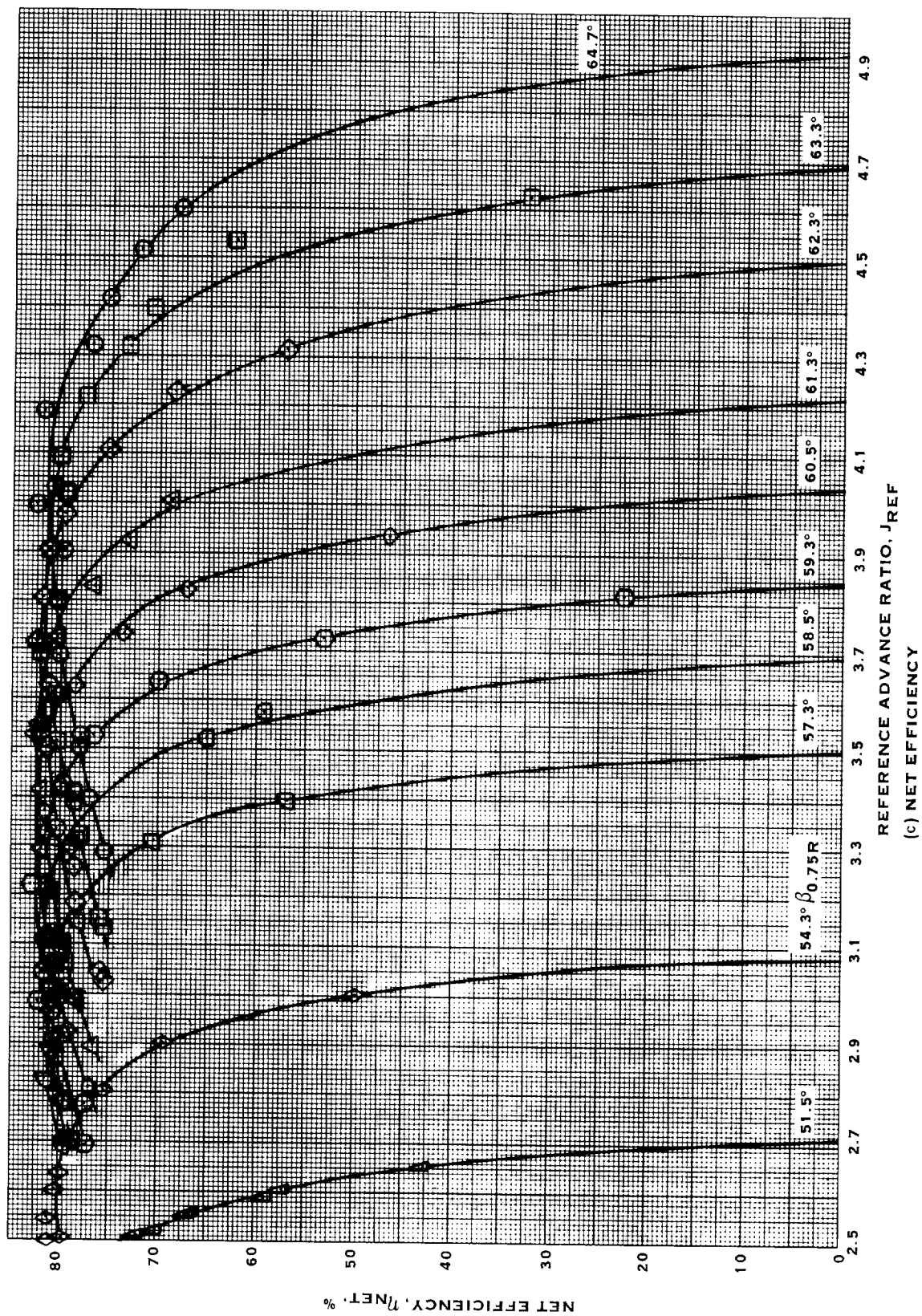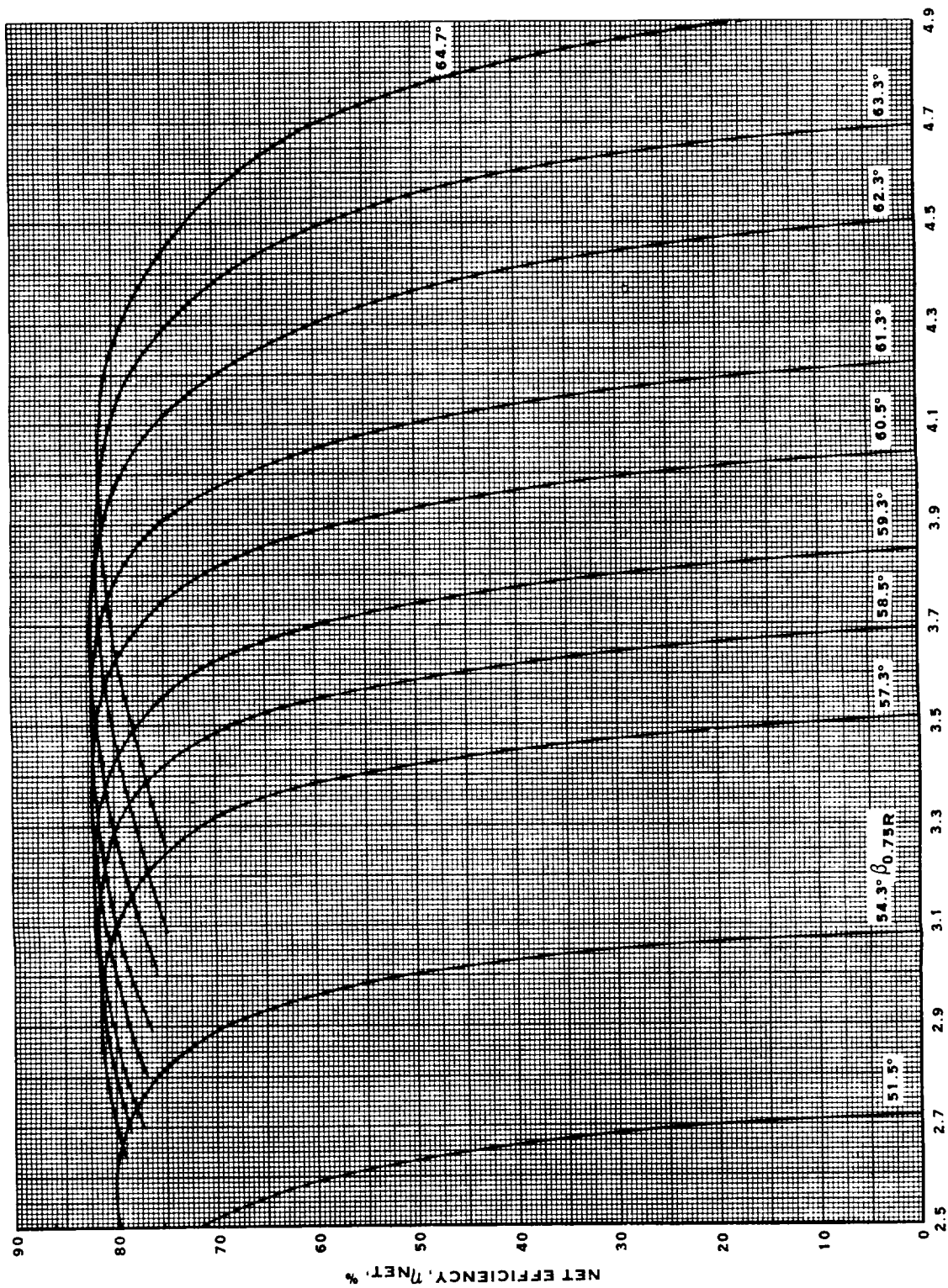
(a) EFFICIENCY MAP
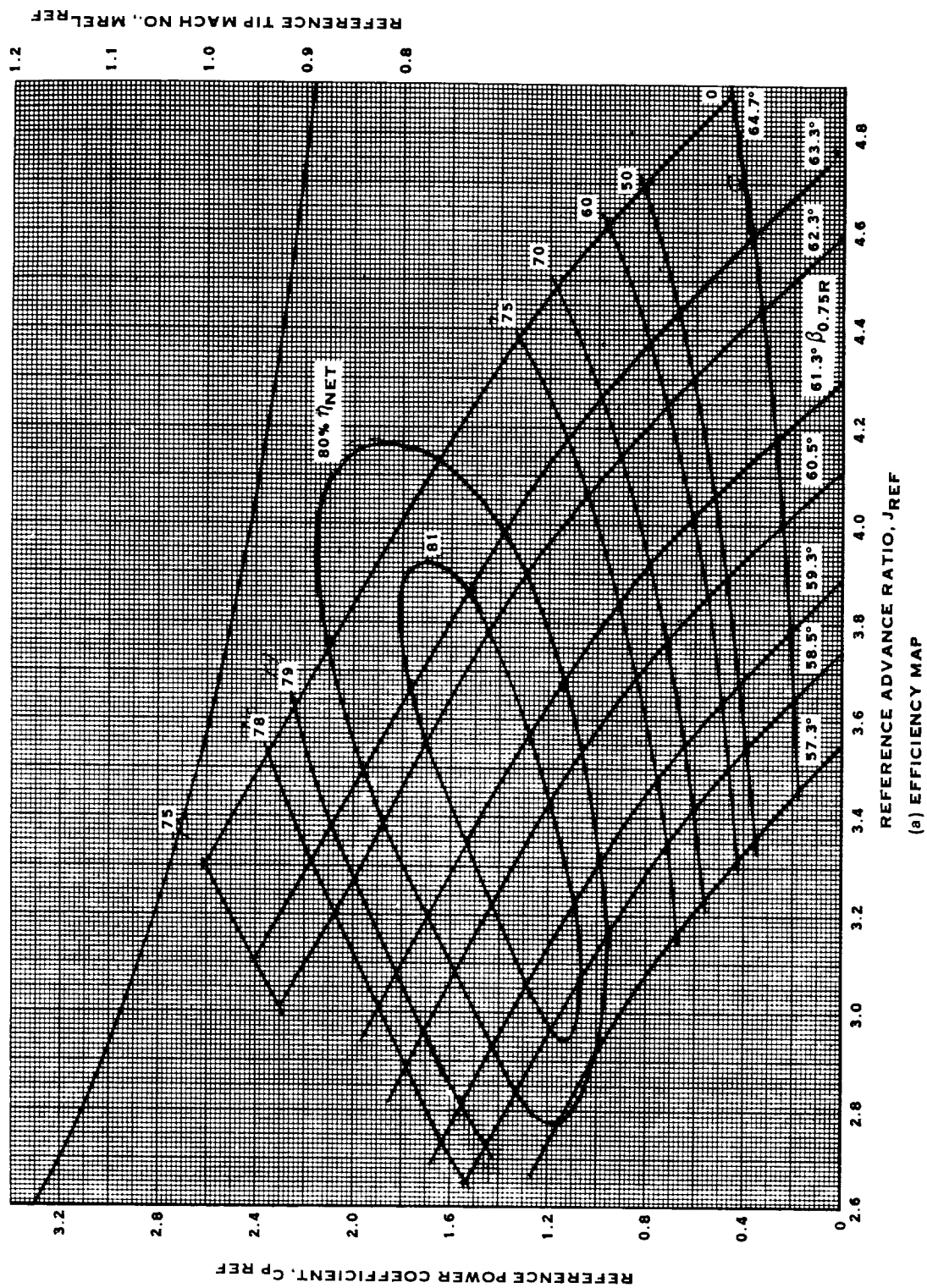
FIGURE 28. PROPELLER PERFORMANCE AT Mo = 0.75

74

REFERENCE ADVANCE RATIO, J_{REF}

(b) POWER COEFFICIENT

FIGURE 28. (CONTINUED)

REFERENCE POWER COEFFICIENT, $C_{P\ REF}$

75

(c) NET EFFICIENCY

FIGURE 28. (CONTINUED)

REFERENCE ADVANCE RATIO, J_{REF}

(d) NET EFFICIENCY FAIRING

FIGURE 28. (CONTINUED)

NET EFFICIENCY, η_{NET}, %
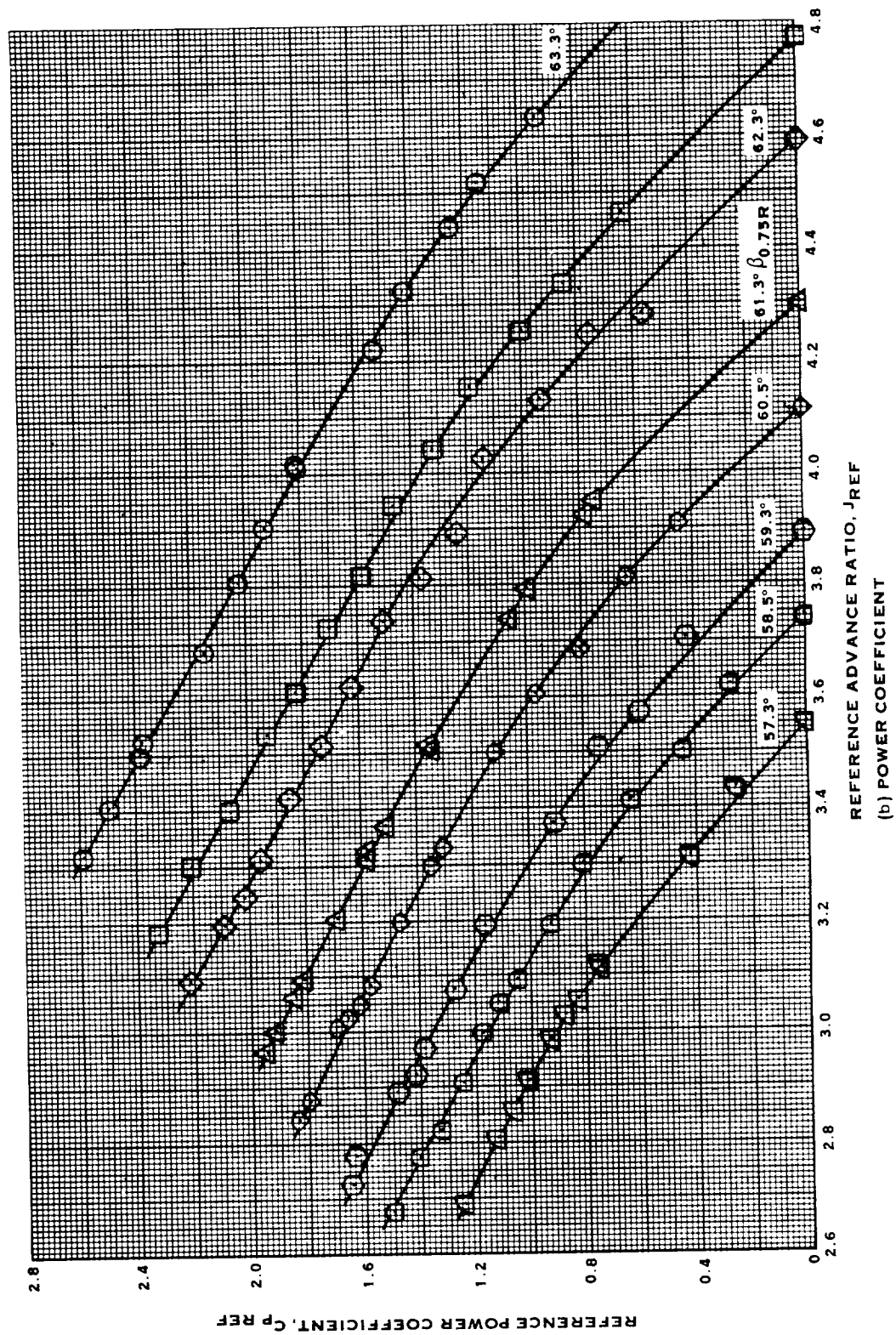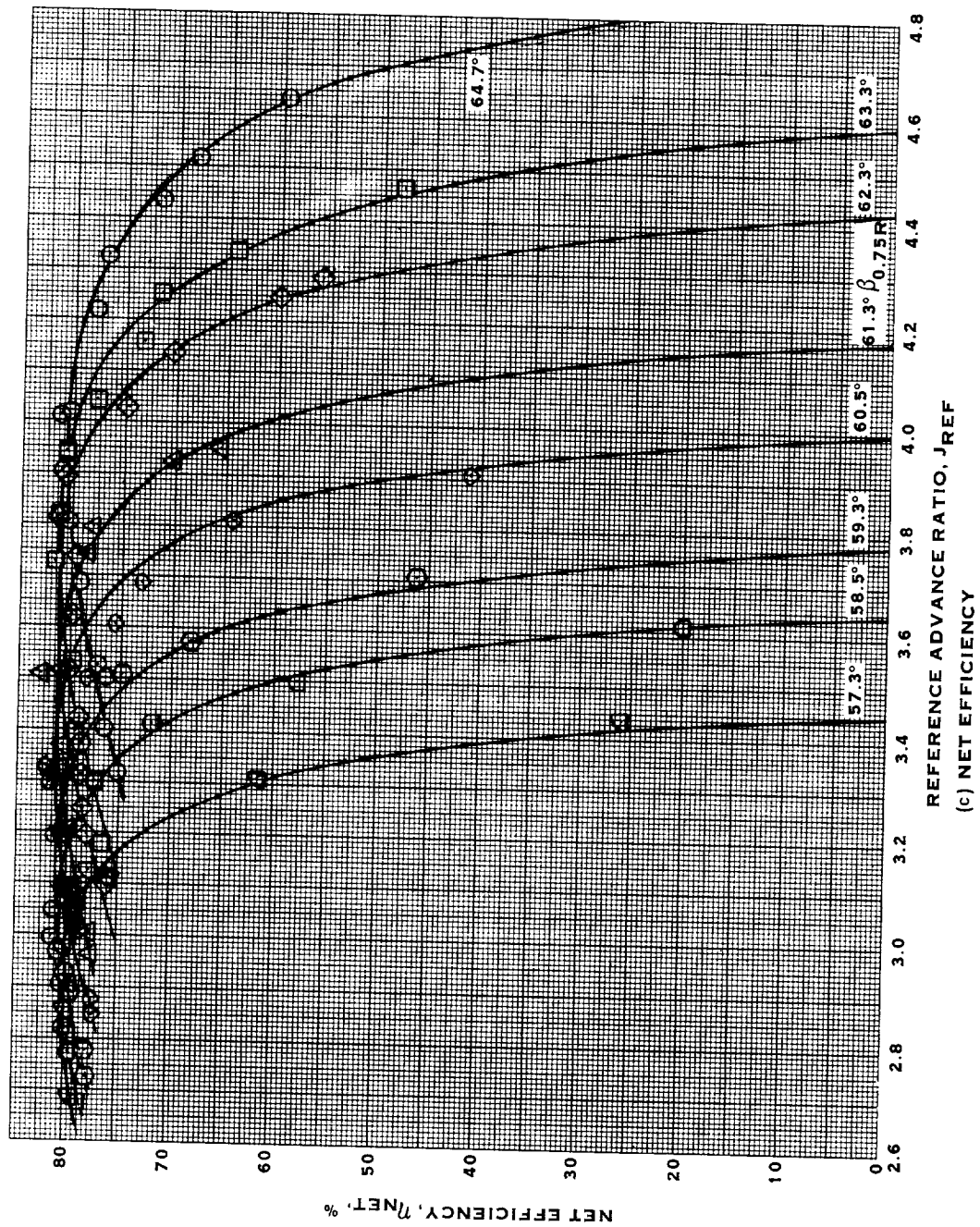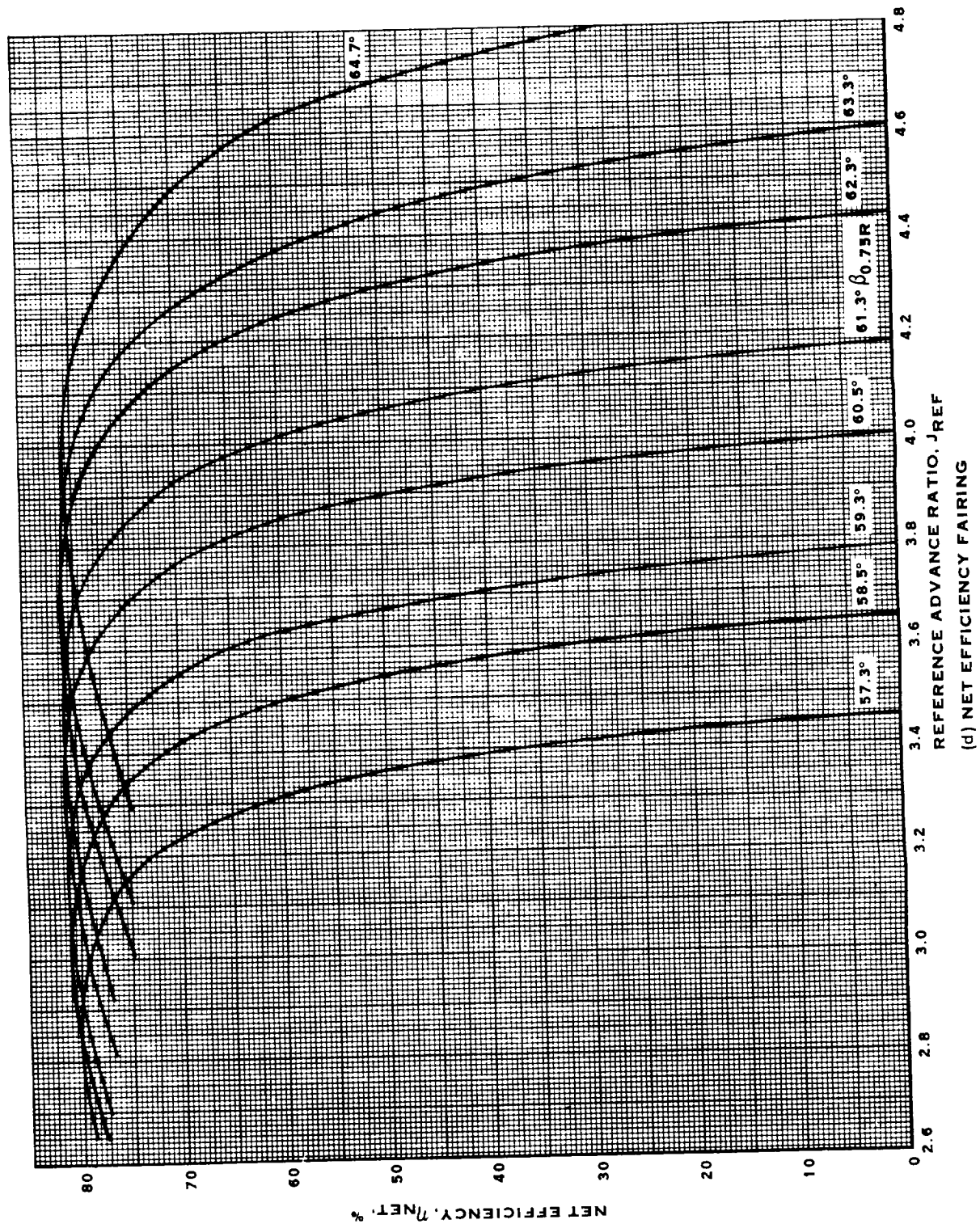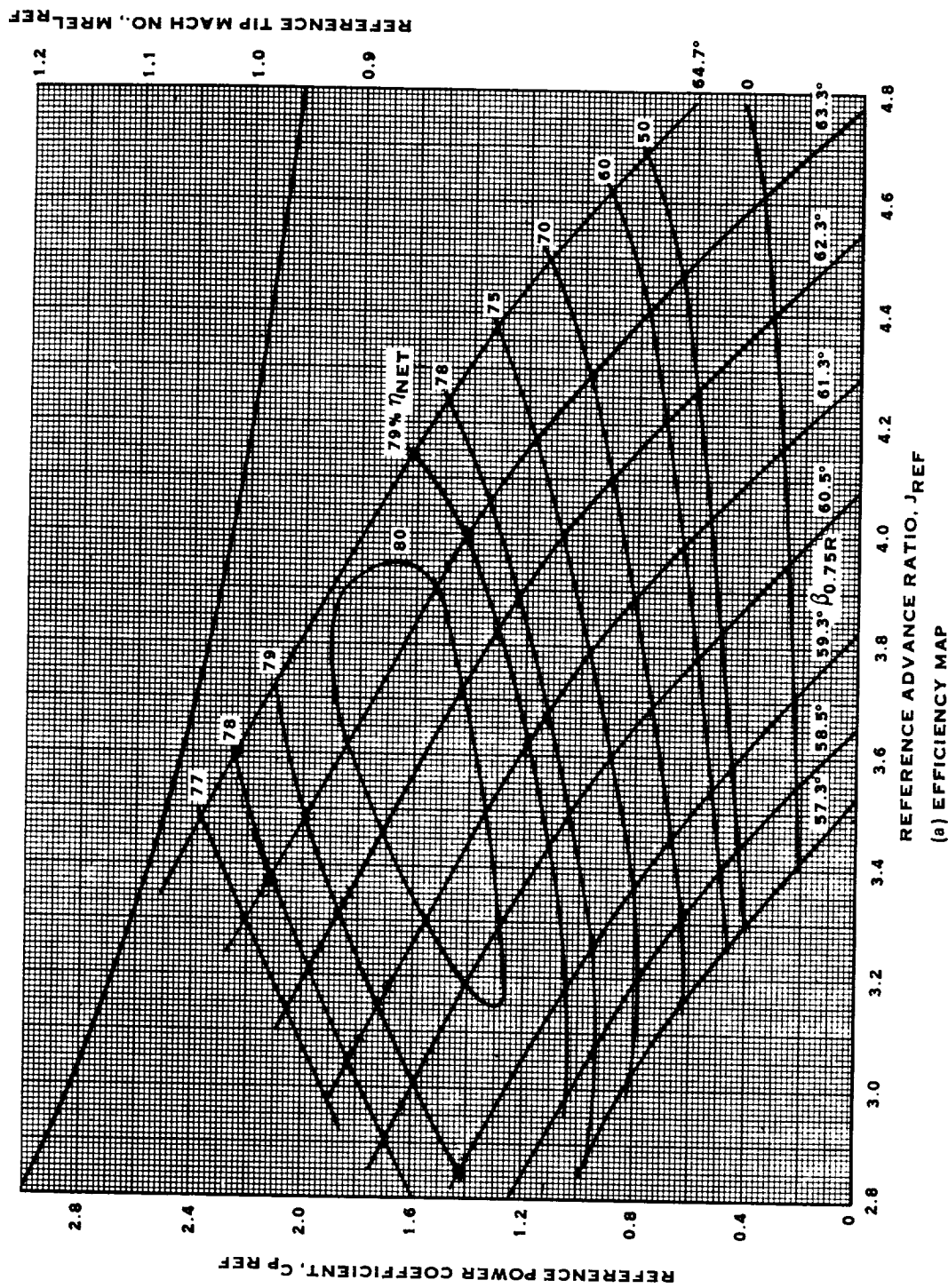
FIGURE 29. PROPELLER PERFORMANCE AT Mo = 0.80

(a) EFFICIENCY MAP

REFERENCE ADVANCE RATIO, J_{REF}

REFERENCE POWER COEFFICIENT, $C_{P\ REF}$

REFERENCE TIP MACH NO., $M_{REL\ REF}$

78

REFERENCE ADVANCE RATIO, J_{REF}

(b) POWER COEFFICIENT

FIGURE 29. (CONTINUED)

REFERENCE ADVANCE RATIO, J_{REF}

(c) NET EFFICIENCY

NET EFFICIENCY, η_{NET}, %

FIGURE 29. (CONTINUED)

80

REFERENCE ADVANCE RATIO, J_{REF}

(d) NET EFFICIENCY FAIRING

FIGURE 29. (CONTINUED)

81

REFERENCE TIP MACH NO., $M_{REL,REF}$

REFERENCE POWER COEFFICIENT, $C_{P\,REF}$

REFERENCE ADVANCE RATIO, J_{REF}

(a) EFFICIENCY MAP

$77\%\,\eta_{NET}$

$61.3°\ \beta_{0.75R}$
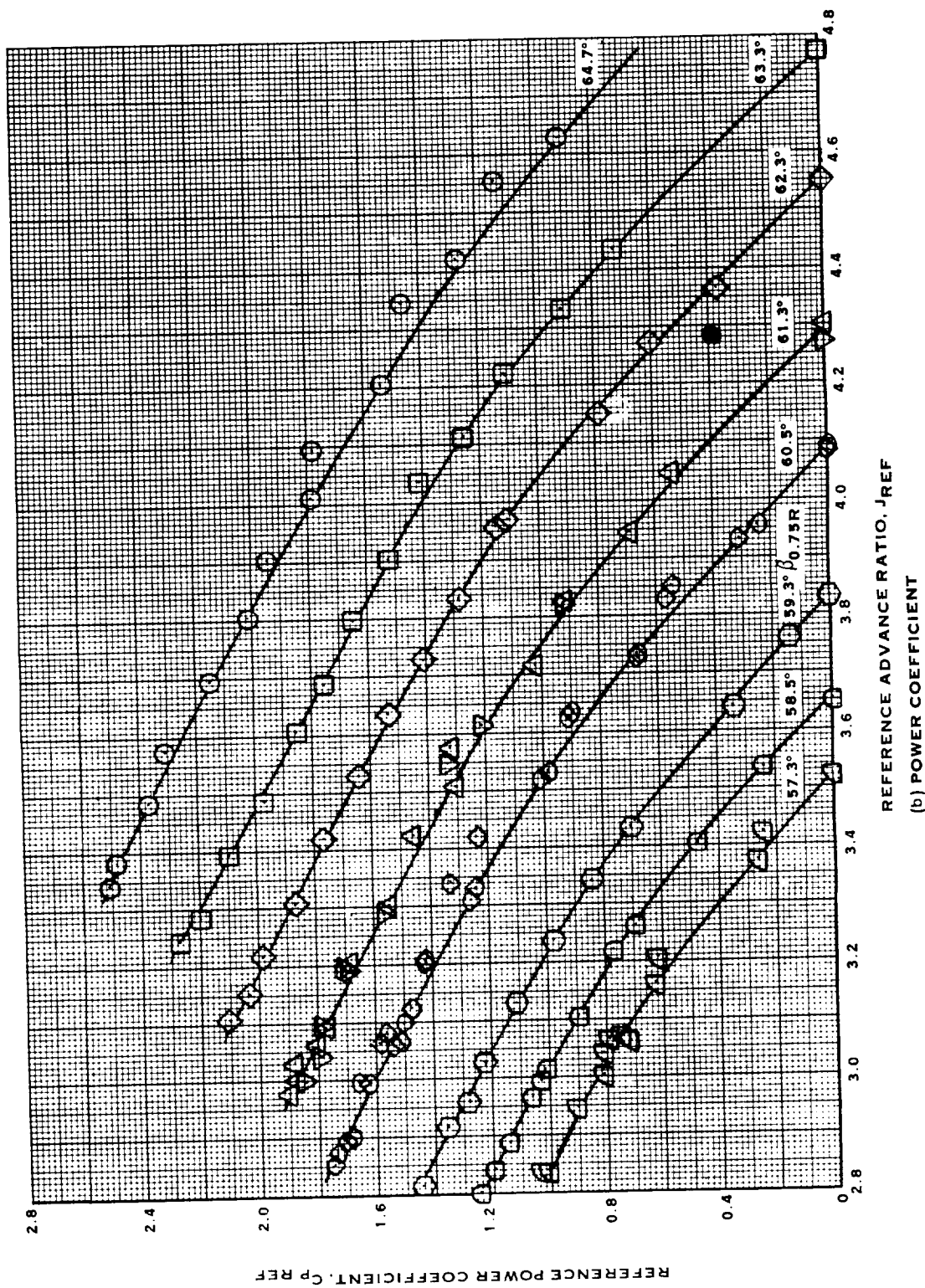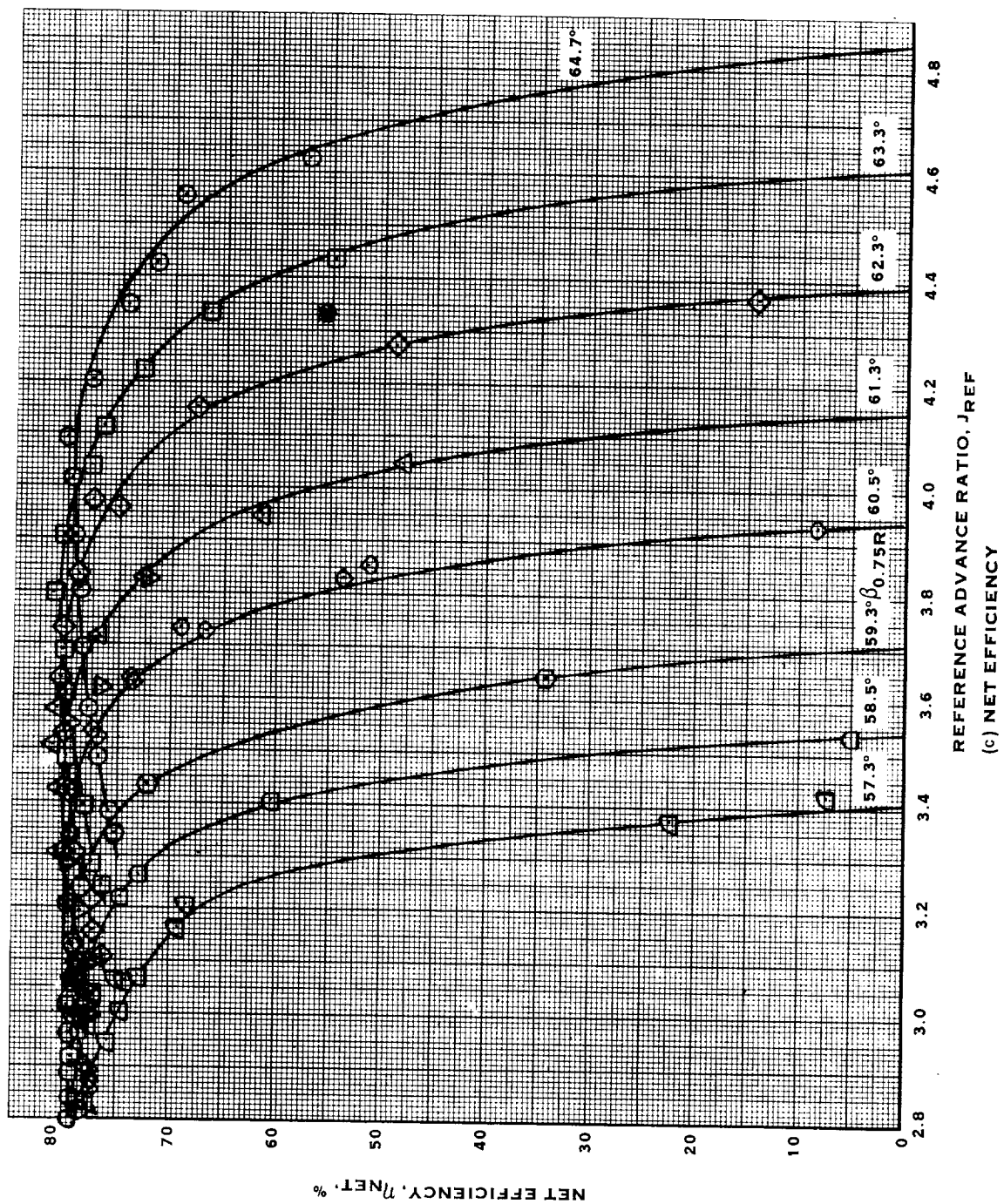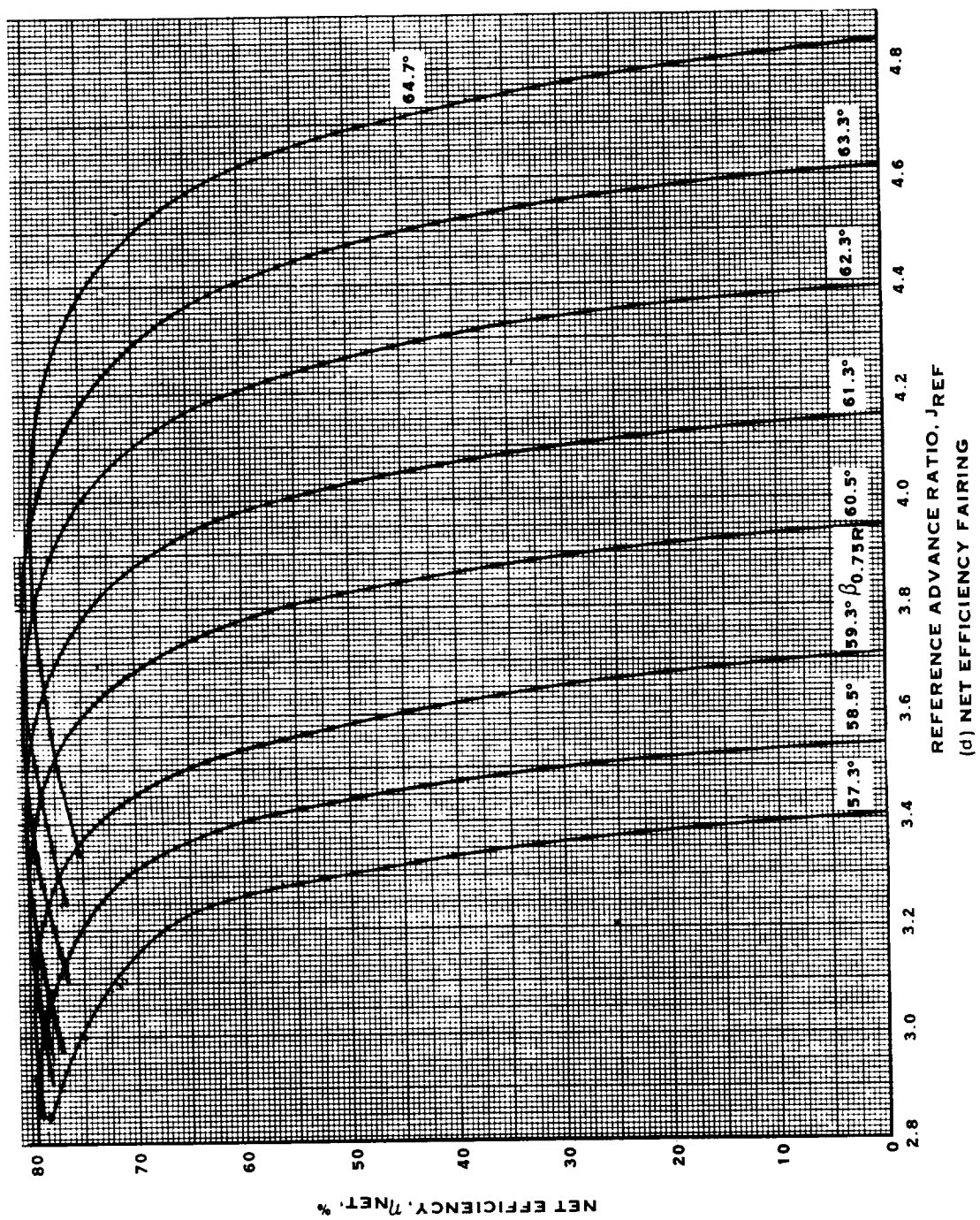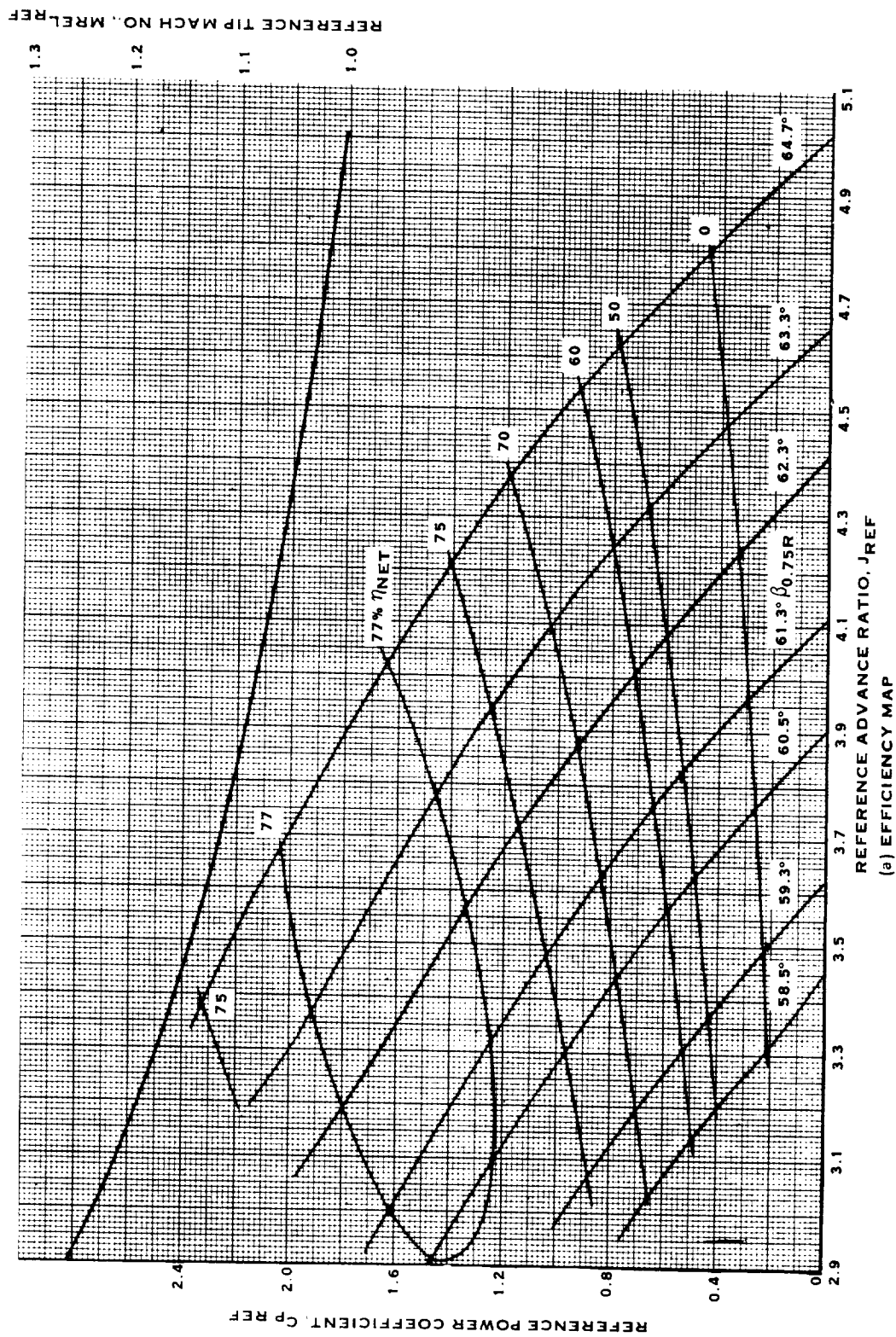
FIGURE 30. PROPELLER PERFORMANCE AT Mo = 0.85
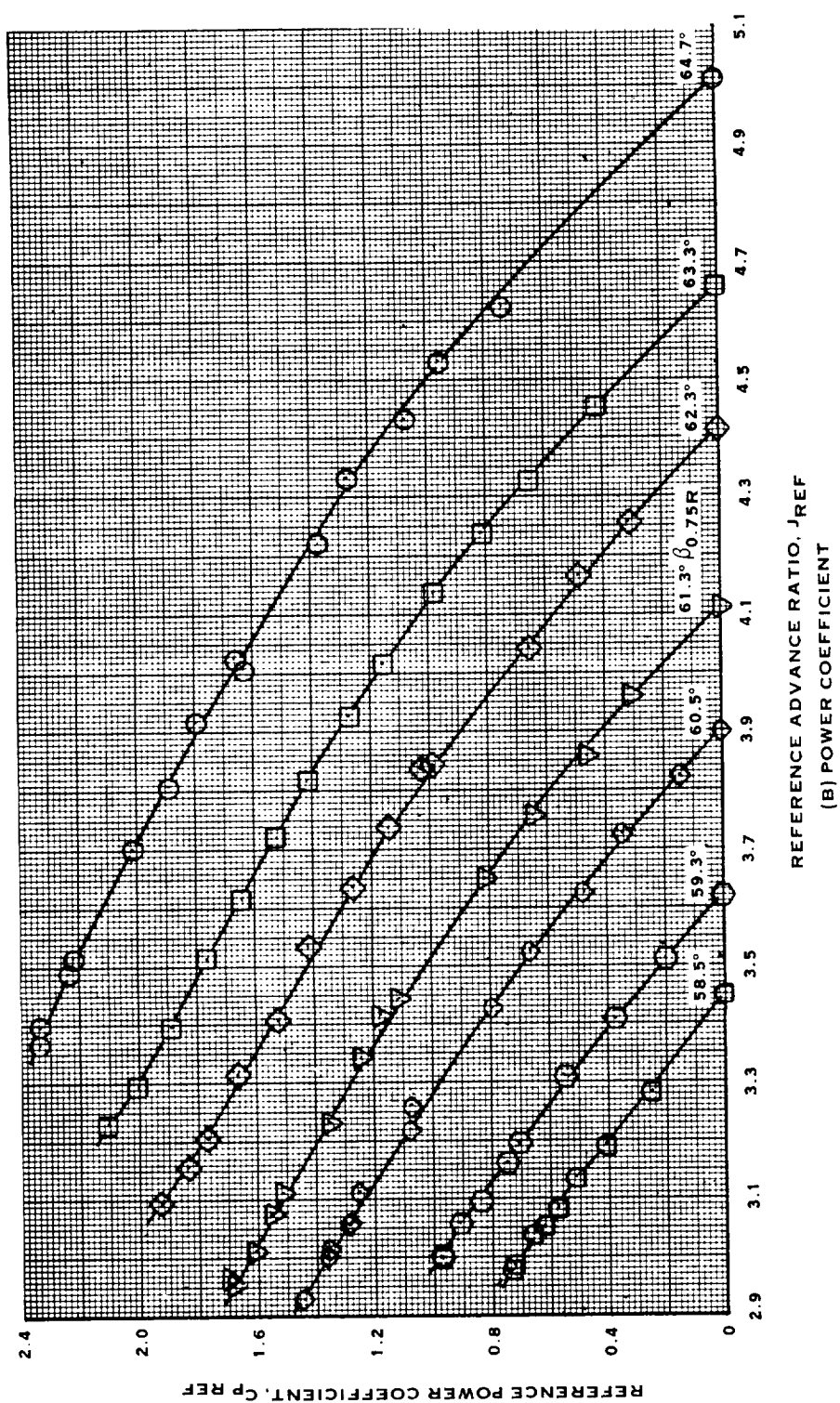
82

REFERENCE ADVANCE RATIO, J_{REF}

(B) POWER COEFFICIENT

FIGURE 30. (CONTINUED)

83

REFERENCE ADVANCE RATIO, J_{REF}

(c) NET EFFICIENCY

FIGURE 30. (CONTINUED)

84
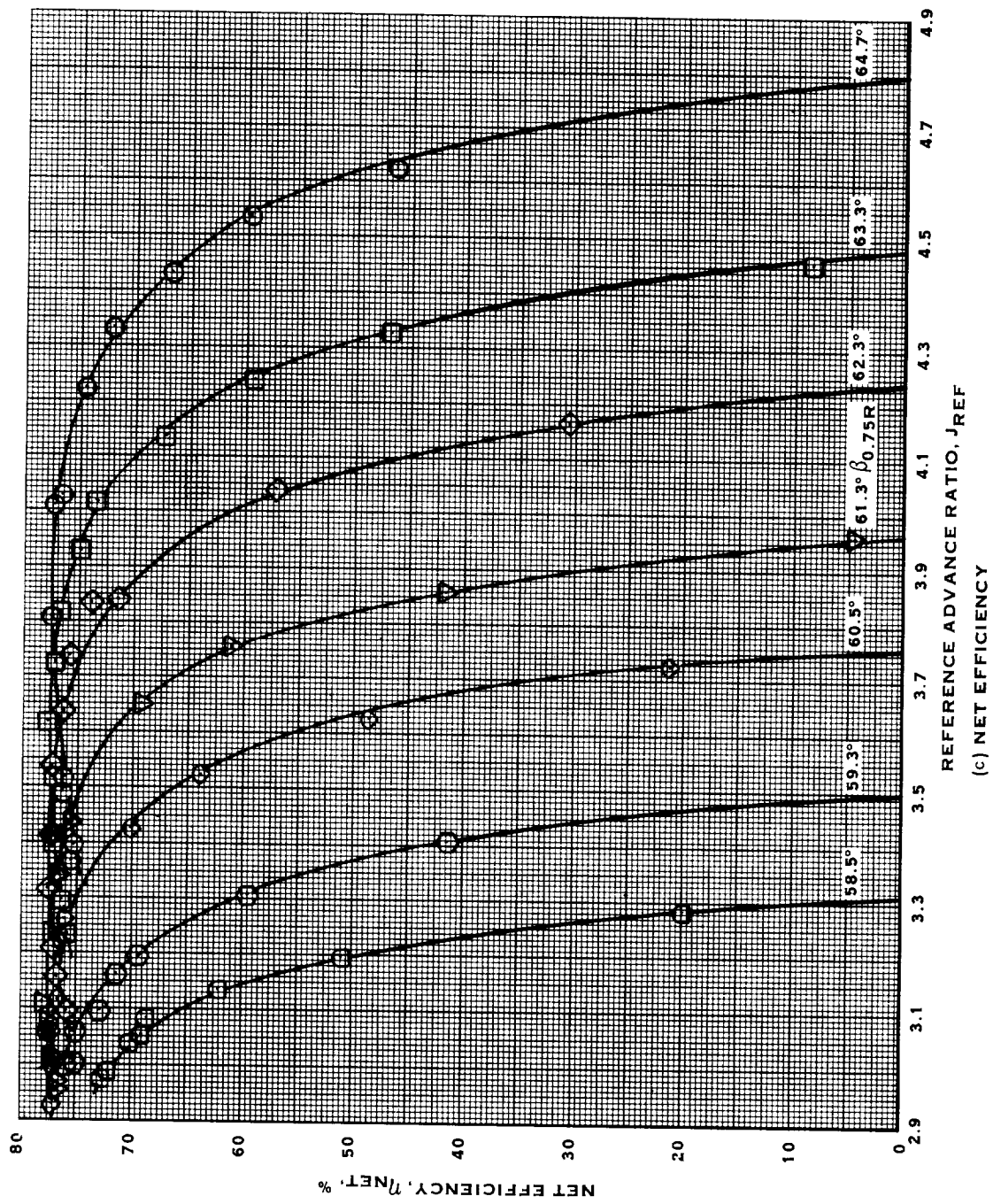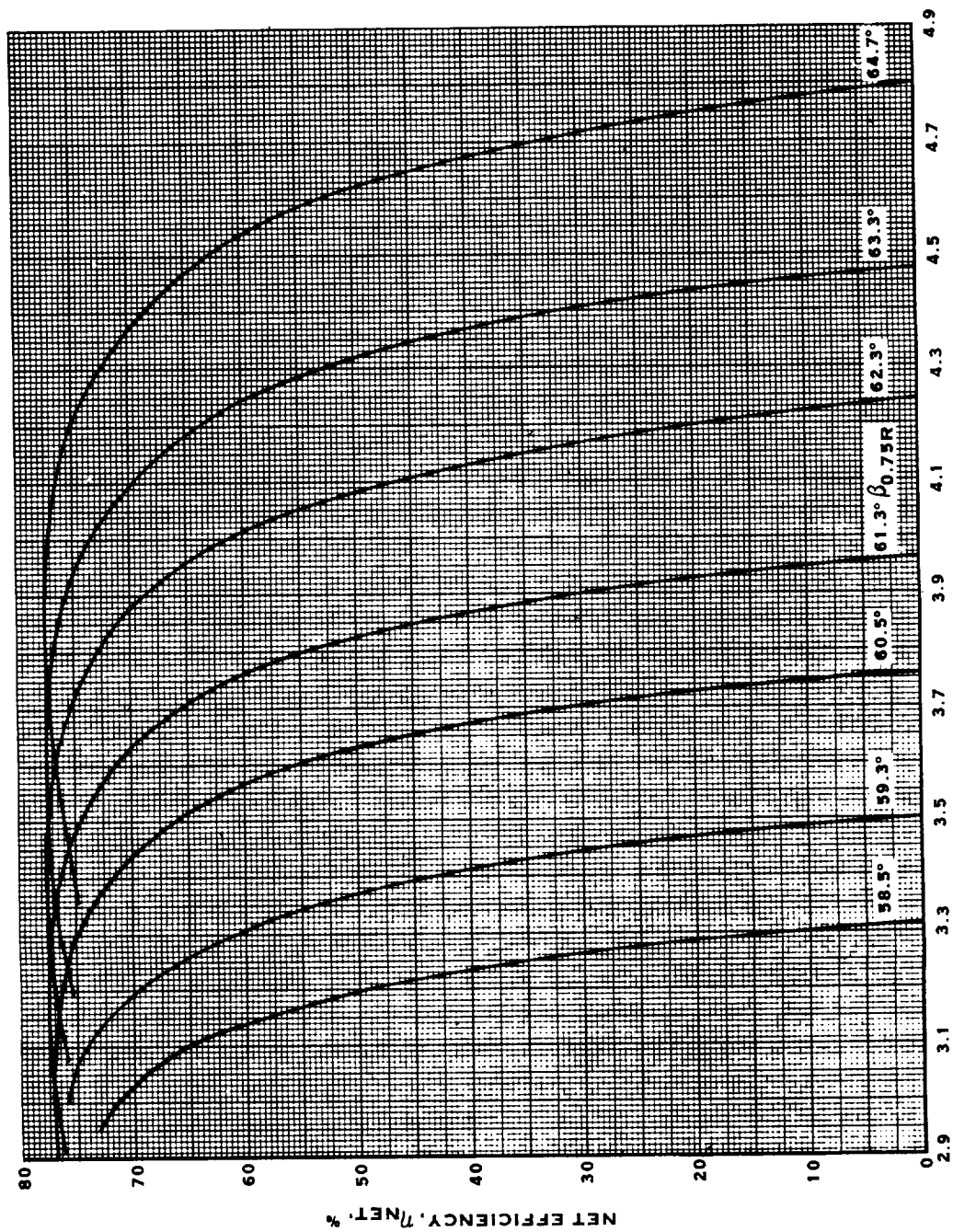
REFERENCE ADVANCE RATIO, J_{REF}

(d) NET EFFICIENCY FAIRING

FIGURE 30. (CONTINUED)

85
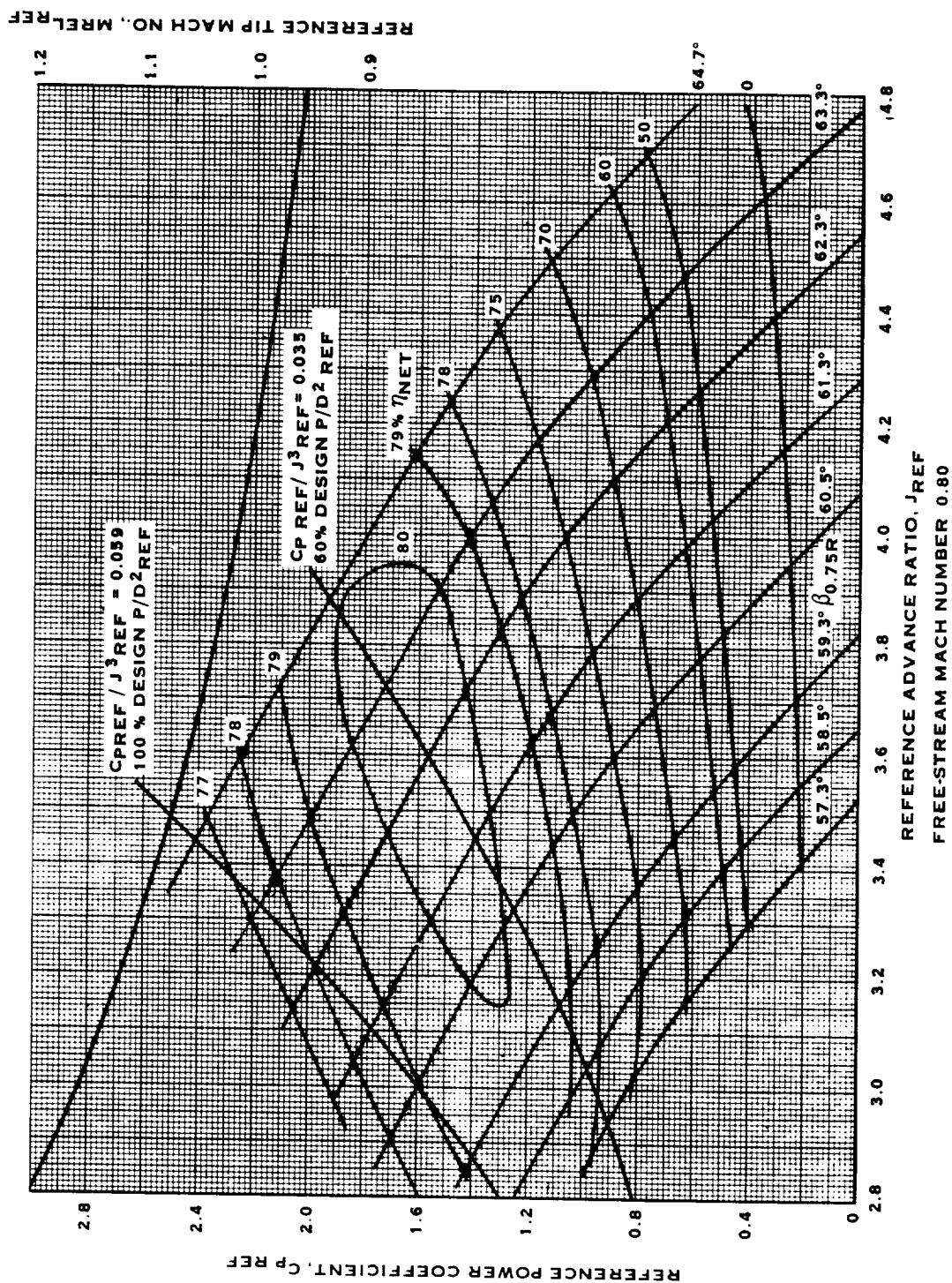
FIGURE 31. 100% AND 60% DESIGN REFERENCE POWER LOADING ON
0.80 MACH NUMBER EFFICIENCY MAP
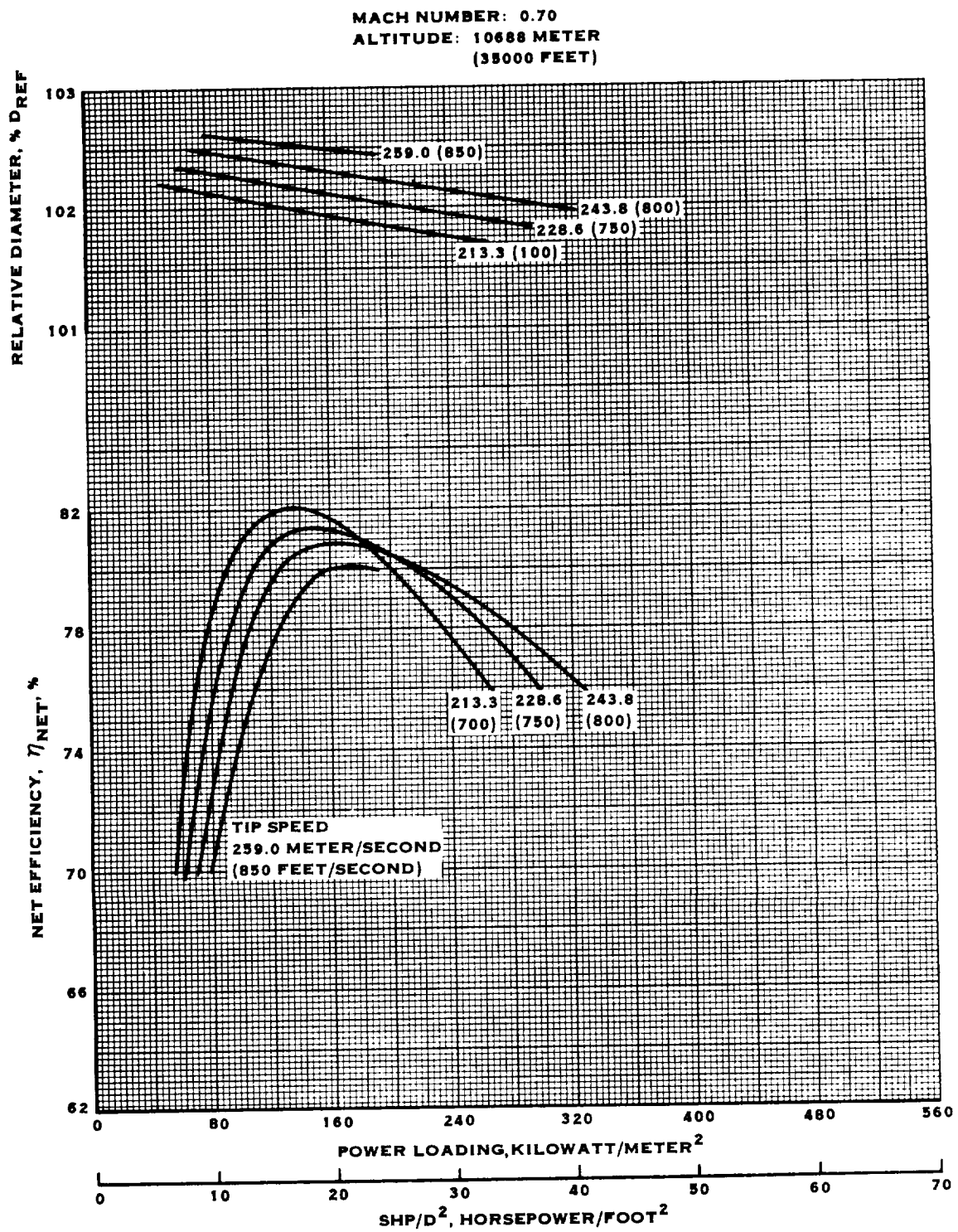
FIGURE 32. VARIATION OF NET EFFICIENCY AND RELATIVE
DIAMETER WITH POWER LOADING AND TIP SPEED

87
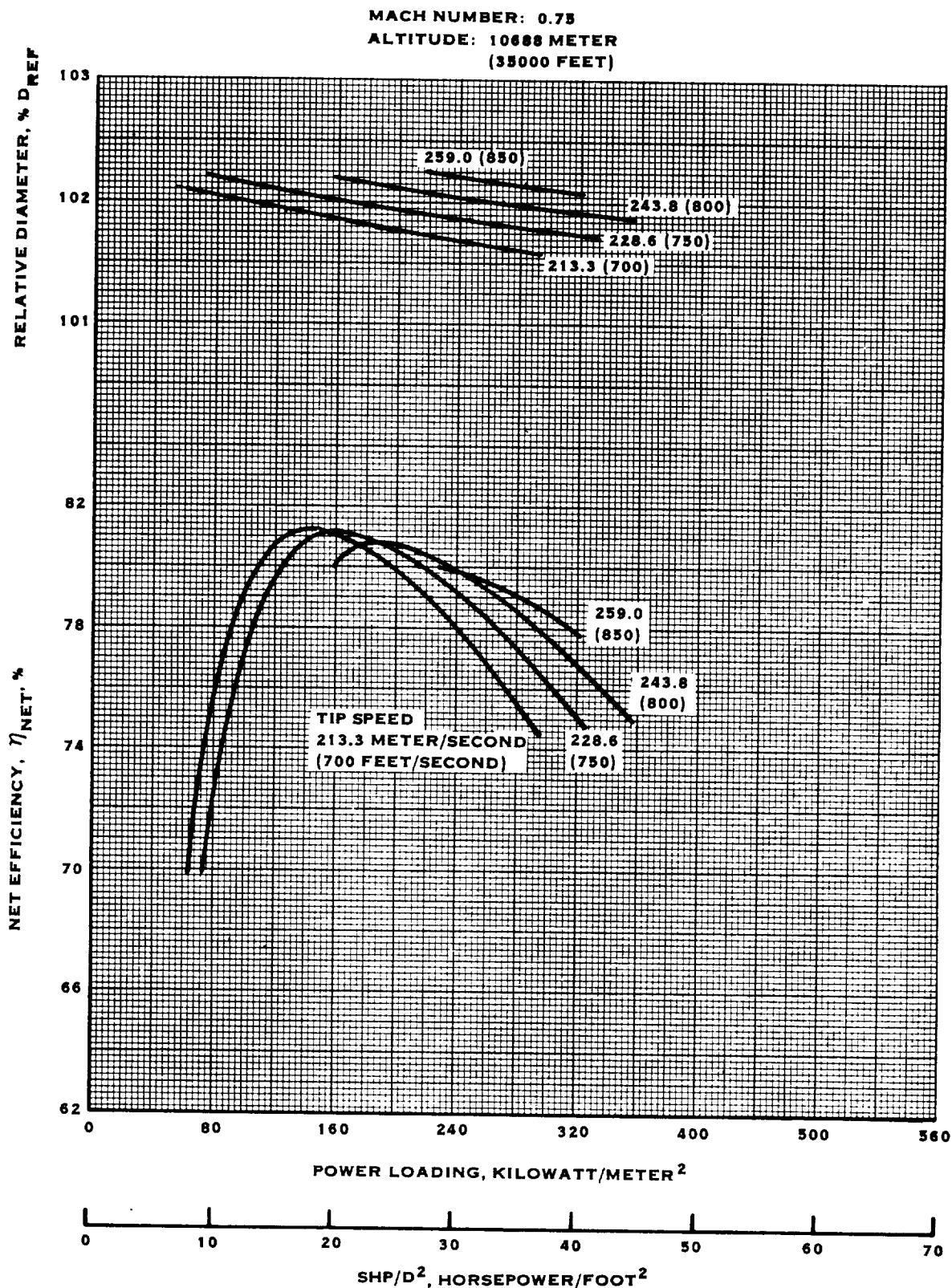
FIGURE 33. VARIATION OF NET EFFICIENCY AND RELATIVE
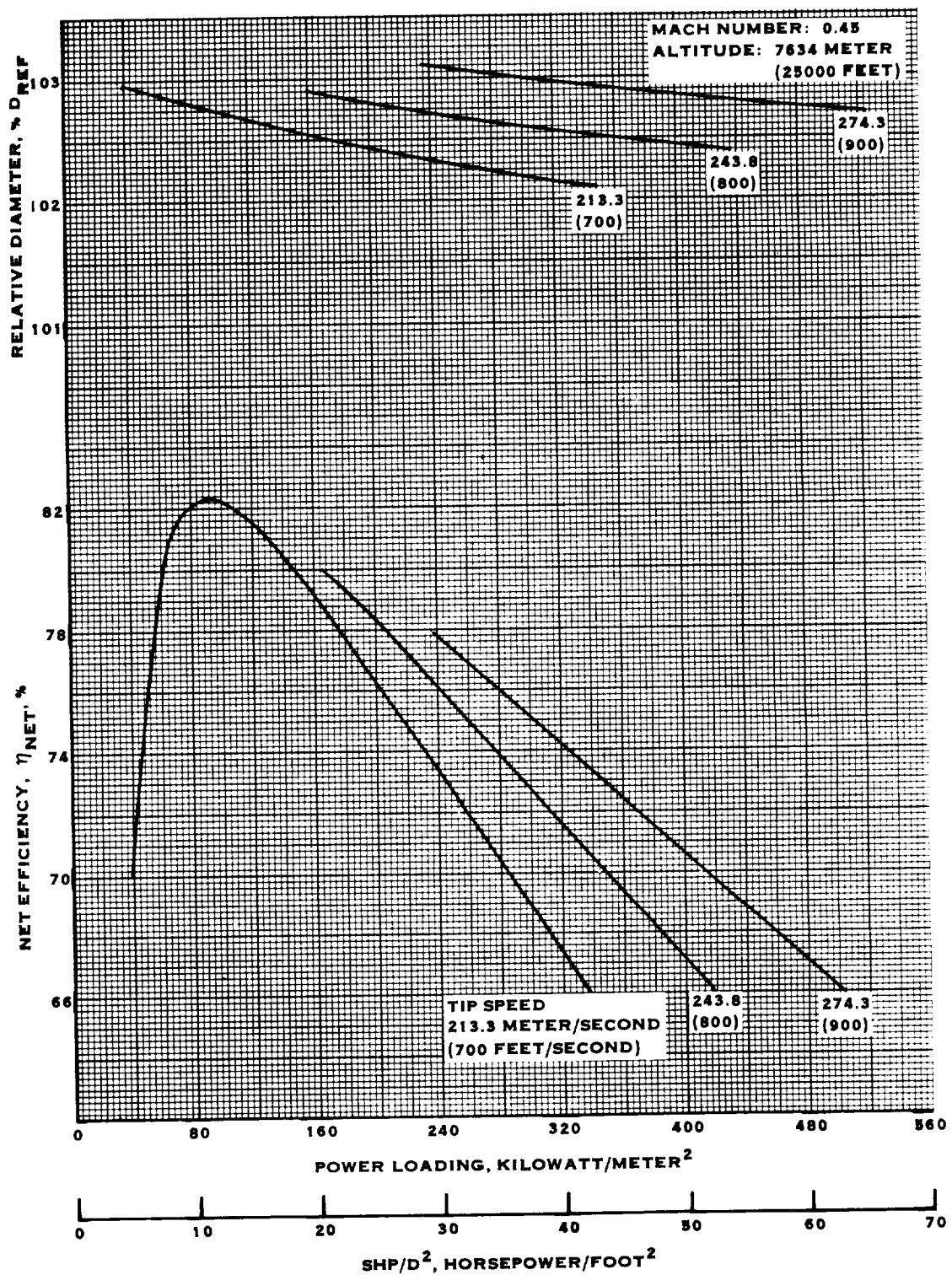DIAMETER WITH POWER LOADING AND TIP SPEED

88
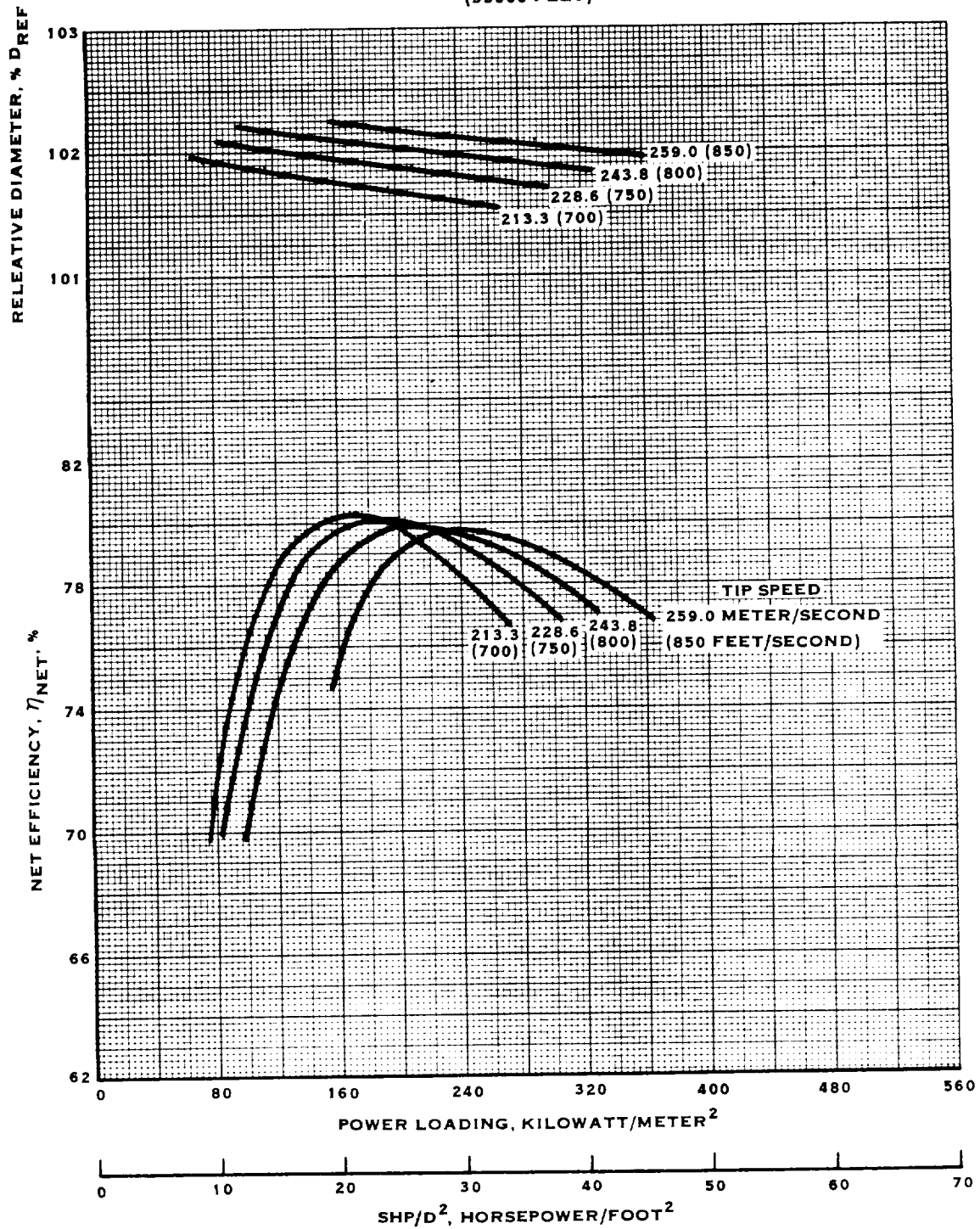
FIGURE 34. VARIATION OF NET EFFICIENCY AND RELATIVE
DIAMETER WITH POWER LOADING AND TIP SPEED
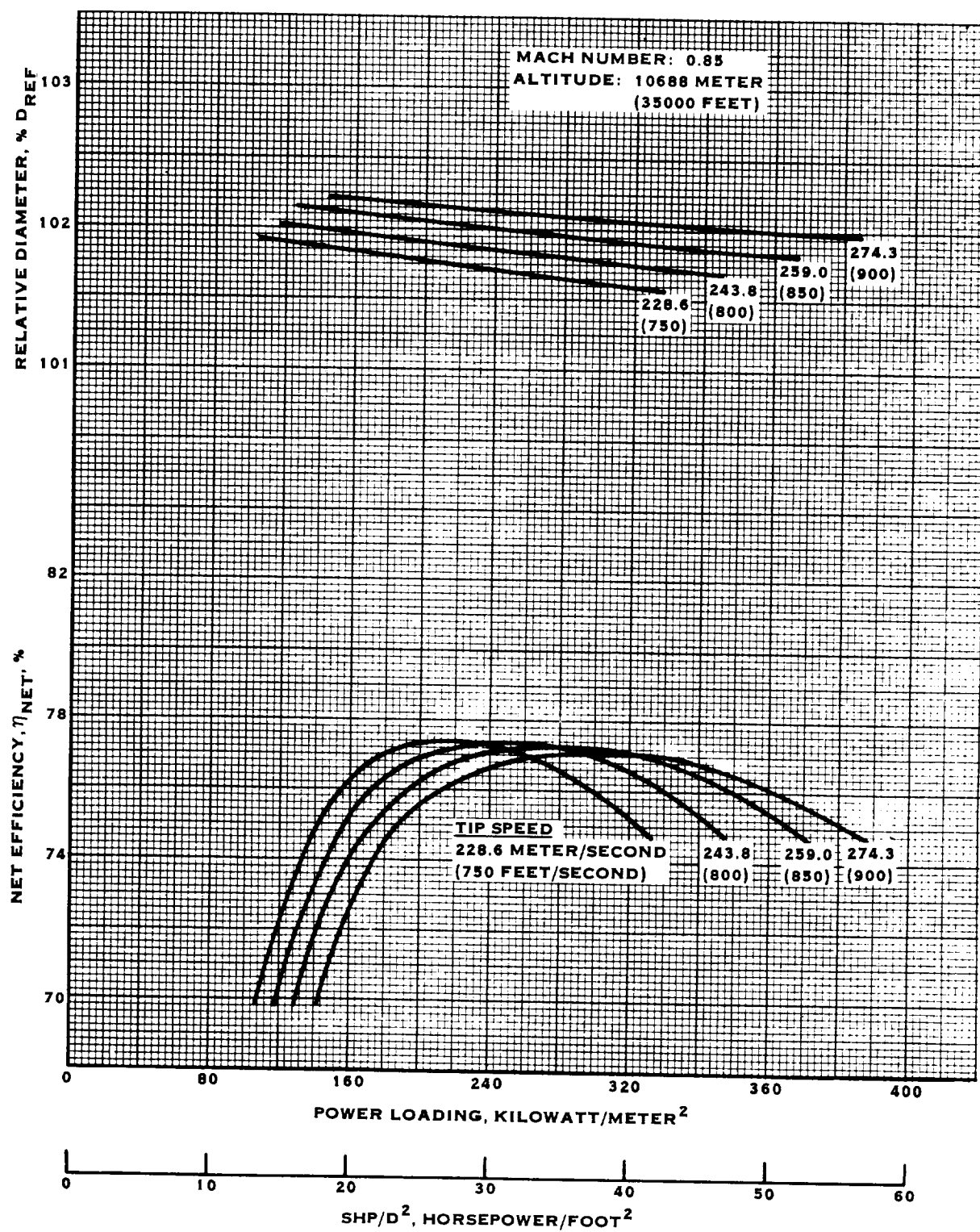
FIGURE 35. VARIATION OF NET EFFICIENCY AND RELATIVE
DIAMETER WITH POWER LOADING AND TIP SPEED

90
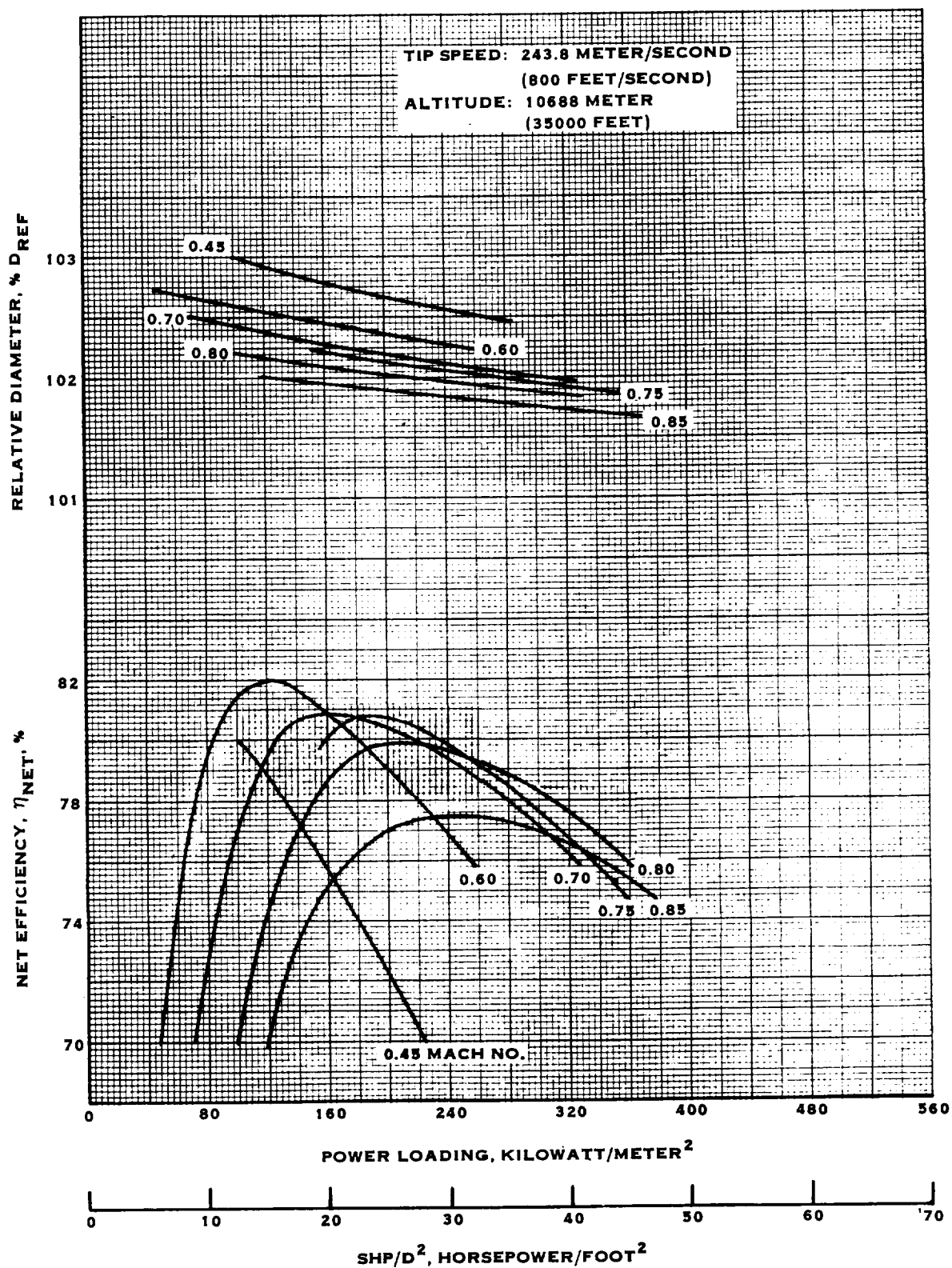
FIGURE 36. VARIATION OF NET EFFICIENCY AND RELATIVE
DIAMETER WITH POWER LOADING AND MACH NUMBER

91

FIGURE 37. VARIATION OF NET EFFICIENCY AND RELATIVE
DIAMETER WITH MACH NUMBER AND POWER LOADING

MACH NUMBER: 0.80
TIP SPEED: 243.8 METER/SECOND
(800 FEET/SECOND)
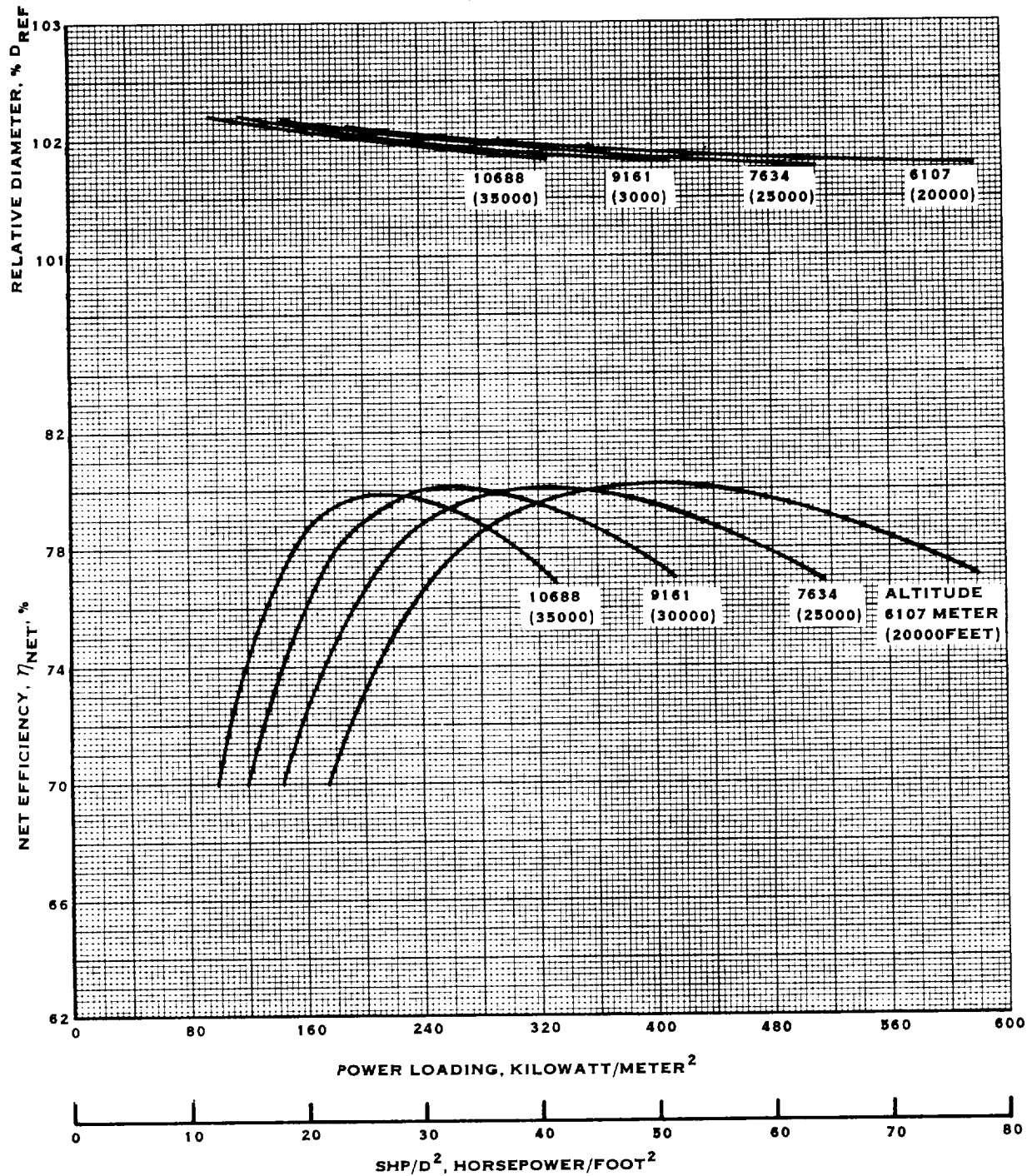
FIGURE 38. VARIATION OF NET EFFICIENCY AND RELATIVE
DIAMETER WITH POWER LOADING AND ALTITUDE

93
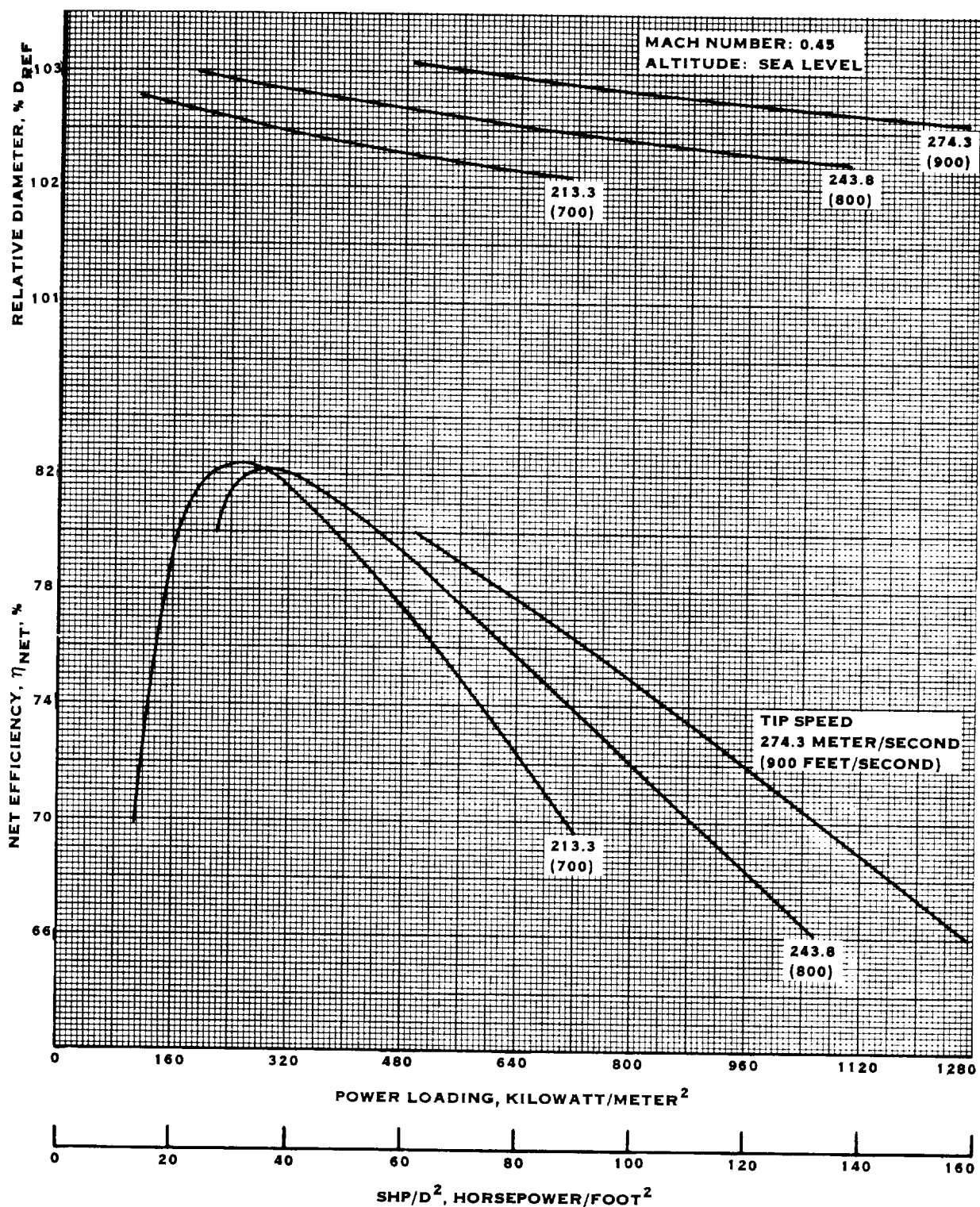
FIGURE 39. VARIATION OF NET EFFICIENCY AND RELATIVE
DIAMETER WITH POWER LOADING AND TIP SPEED

FIGURE 40. VARIATION OF NET EFFICIENCY AND RELATIVE
DIAMETER WITH POWER LOADING AND TIP SPEED
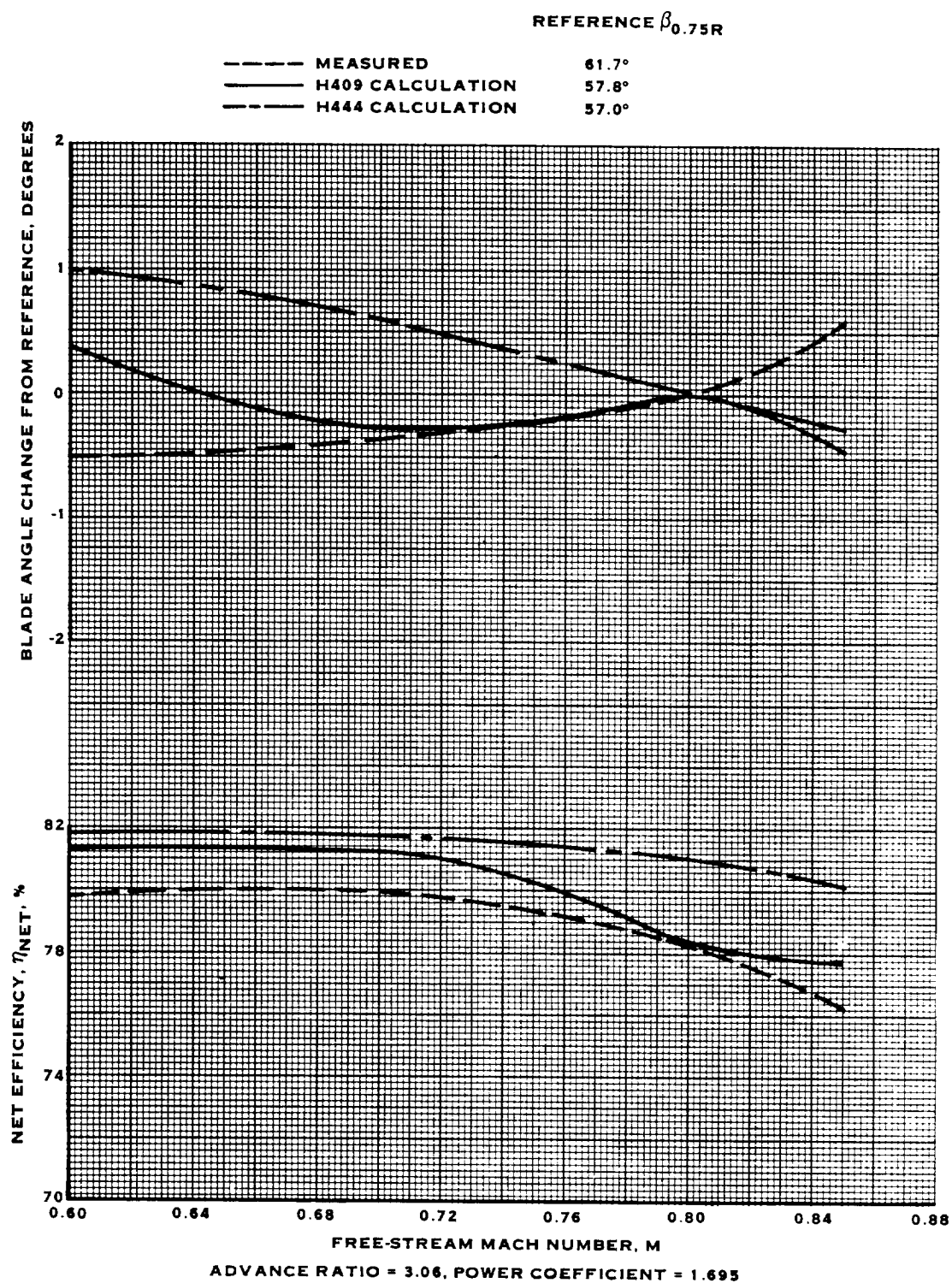
FIGURE 41. CALCULATION AND TEST COMPARISON – MACH NUMBER CHANGE
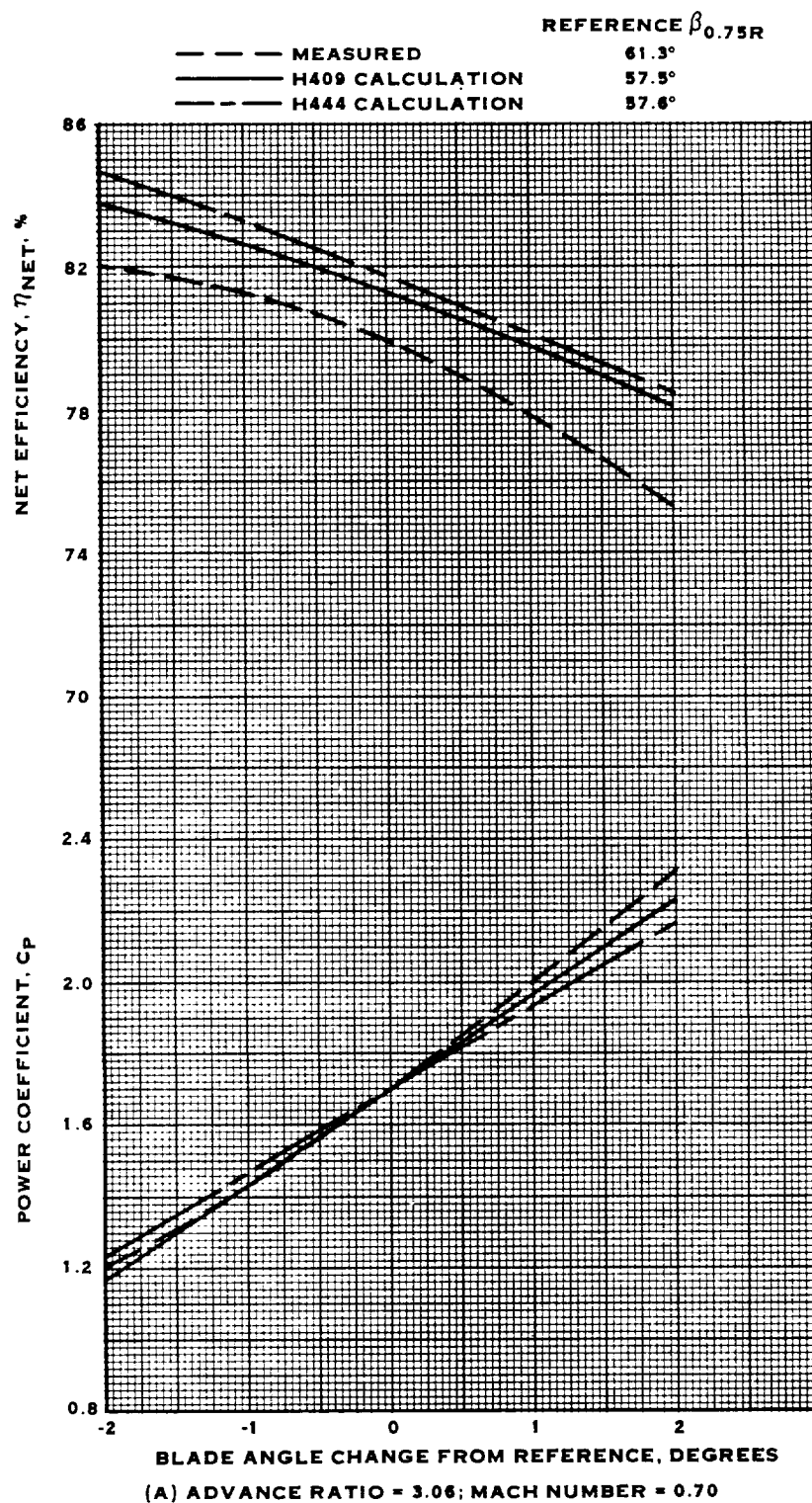
FIGURE 42. CALCULATION AND TEST COMPARISON - BLADE ANGLE CHANGE

REFERENCE $\beta_{0.75R}$

——— MEASURED	61.7°
——— H409 CALCULATION	57.8°
——— H444 CALCULATION	57.0°
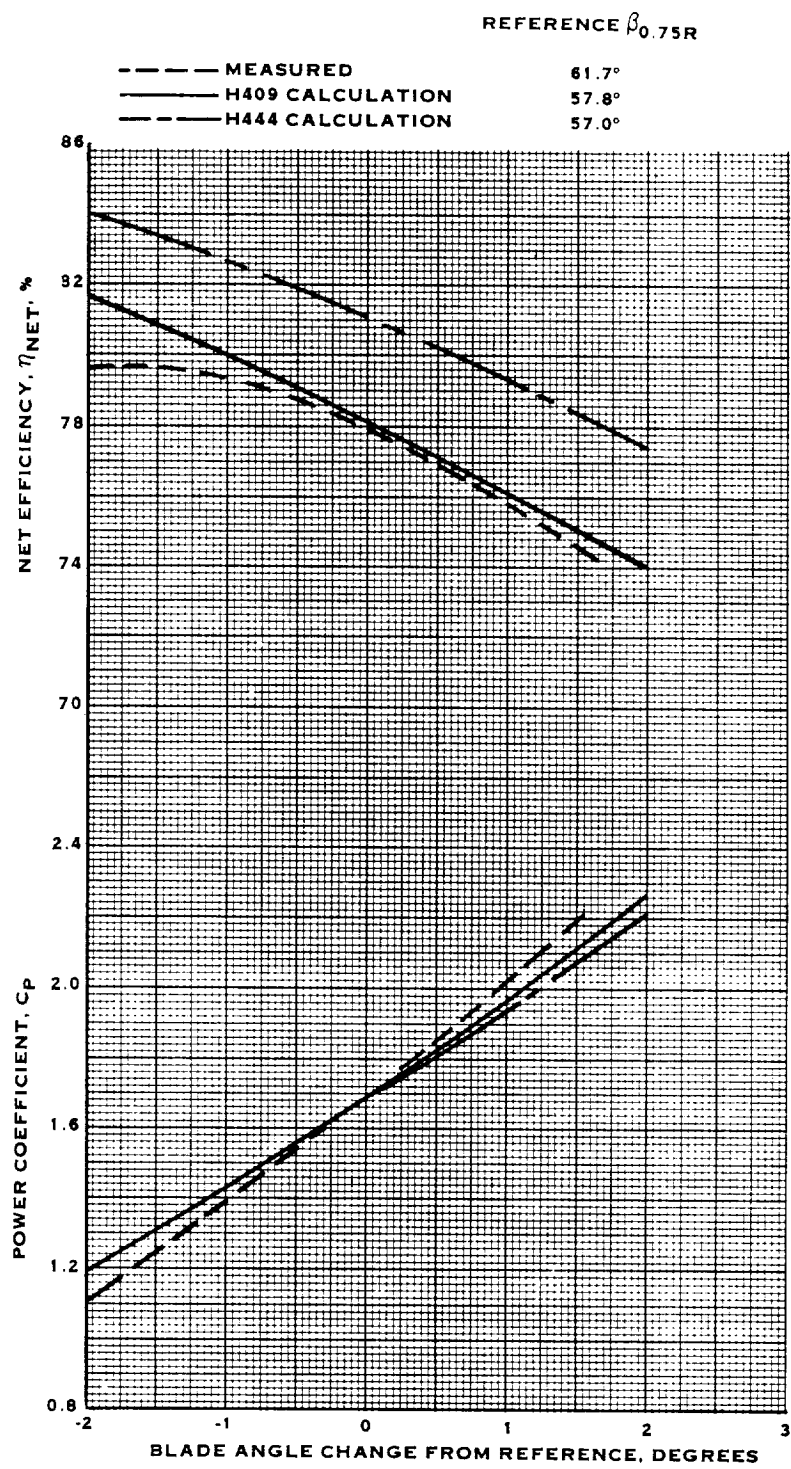
(B) ADVANCE RATIO = 3.06; MACH NUMBER = 0.80

FIGURE 42. (CONTINUED)

98

REFERENCE $\beta_{0.75R}$

---- MEASURED .... 62.3°
———— H409 CALCULATION ... 57.3°
—- - —— H444 CALCULATION ... 56.7°

BLADE ANGLE CHANGE FROM REFERENCE, DEGREES

(C) ADVANCE RATIO = 3.06; MACH NUMBER = 0.85

FIGURE 42. (CONTINUED)

REFERENCE $\beta_{0.75R}$

– – – – MEASURED	61.3°
———— H409 CALCULATION	57.5°
– – – – H444 CALCULATION	57.6°
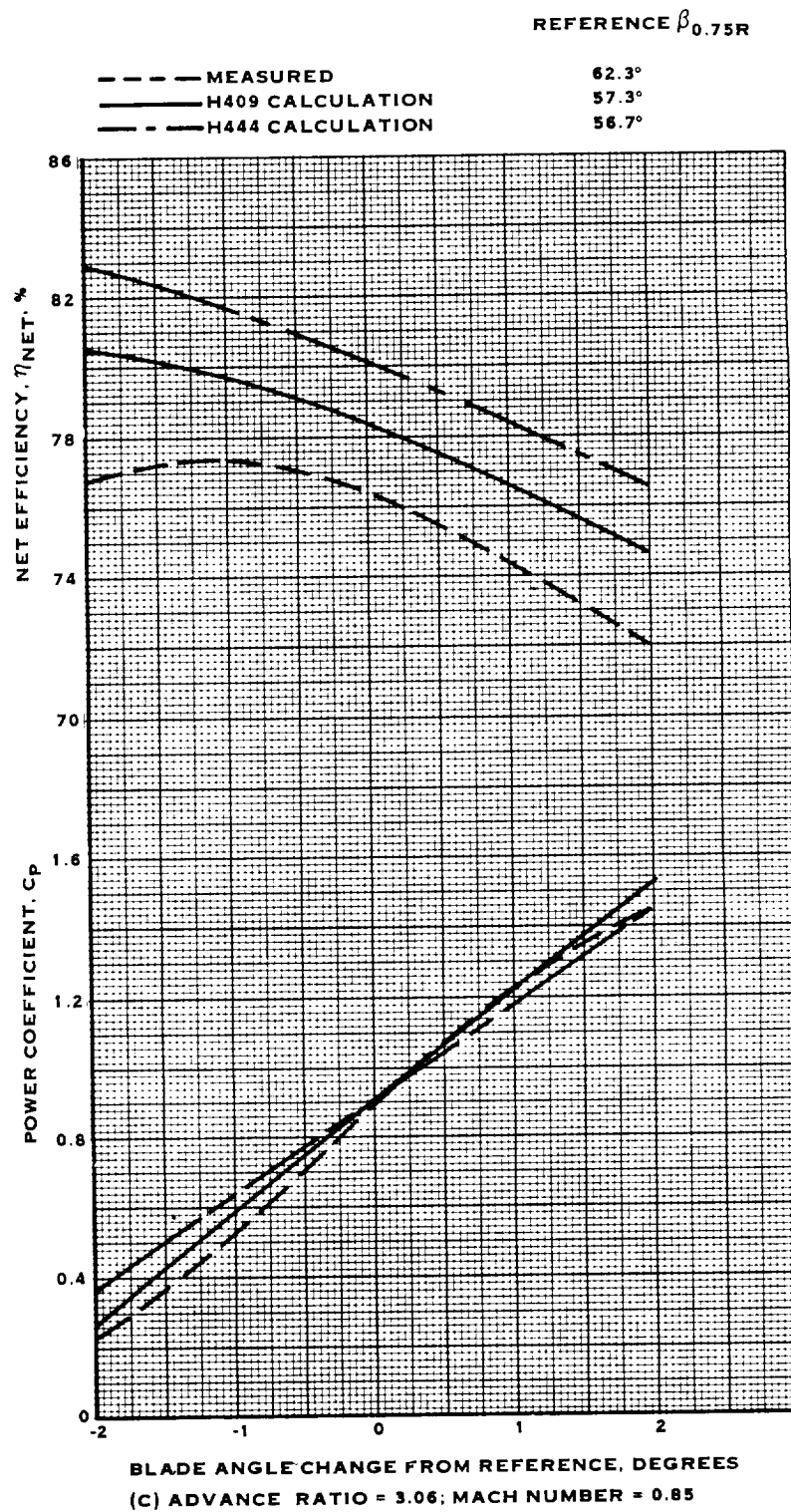
(A) BLADE ANGLE = CONSTANT: MACH NUMBER = 0.70
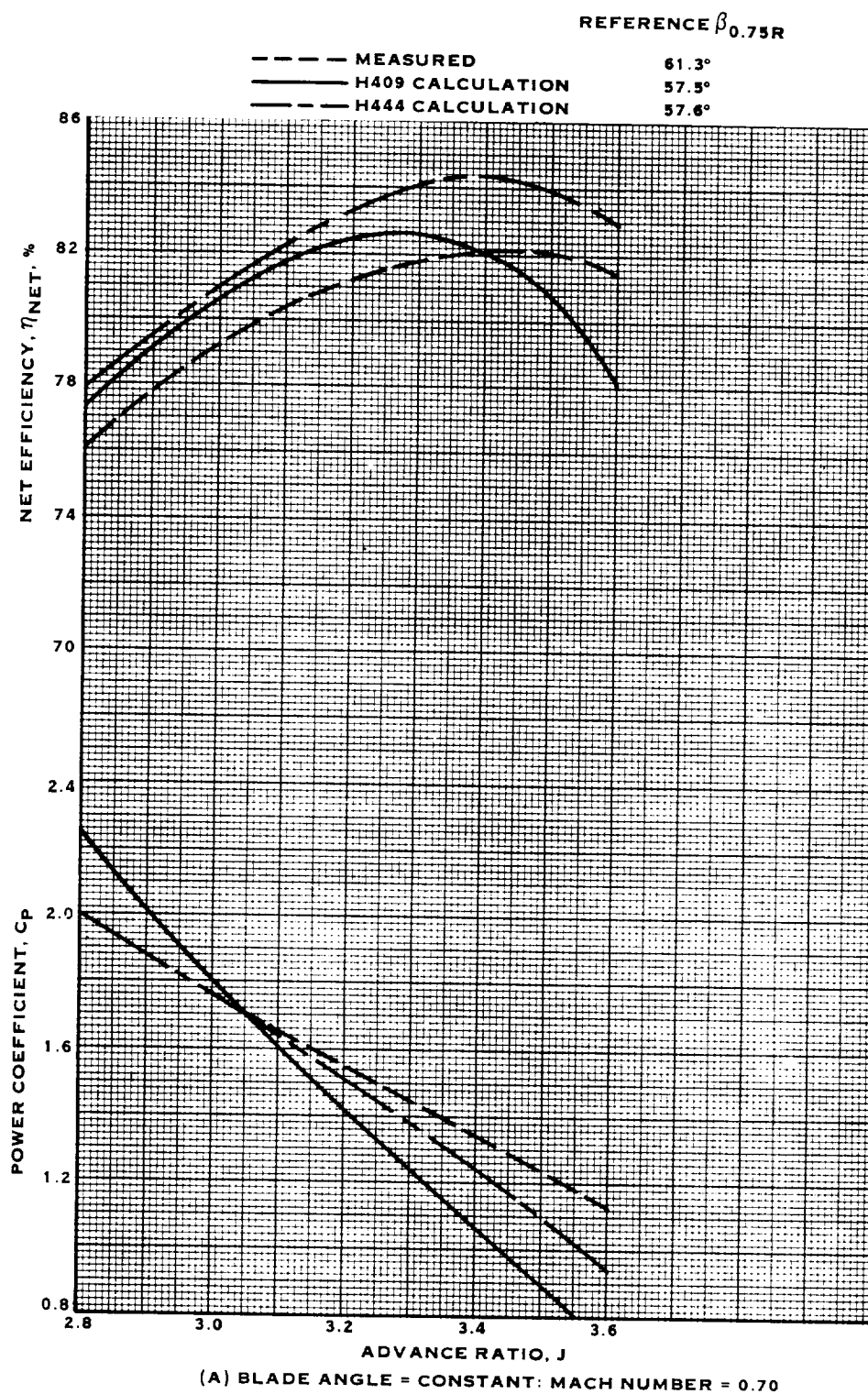
FIGURE 43. CALCULATION AND TEST COMPARISON – ADVANCE RATIO CHANGE

100

REFERENCE $\beta_{0.75R}$

— — — MEASURED   61.7°
———— H409 CALCULATION   57.8°
—— — H444 CALCULATION   57.0°
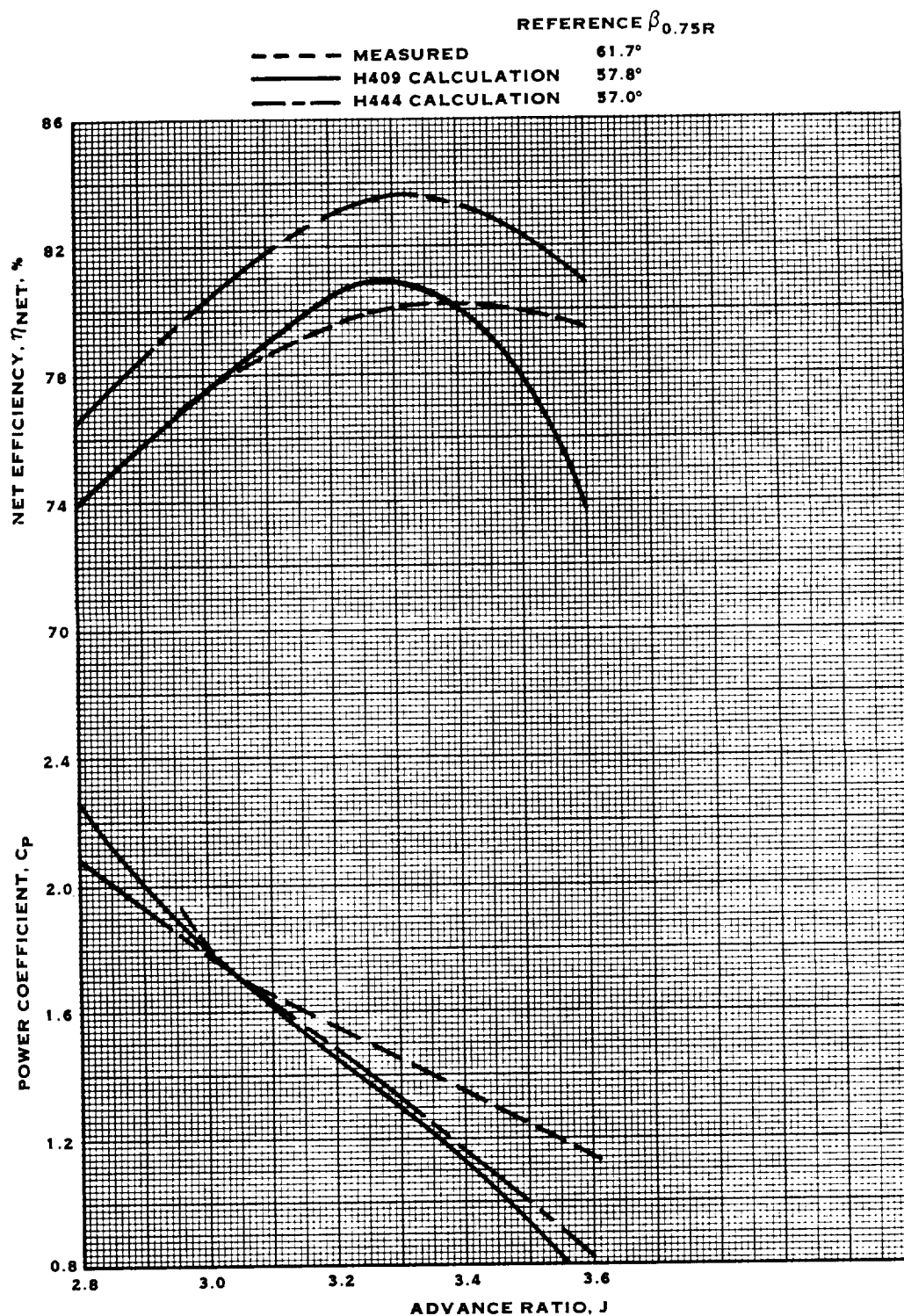
(B) BLADE ANGLE = CONSTANT: MACH NUMBER = 0.80

FIGURE 43. (CONTINUED)

FIGURE 43. (CONTINUED)

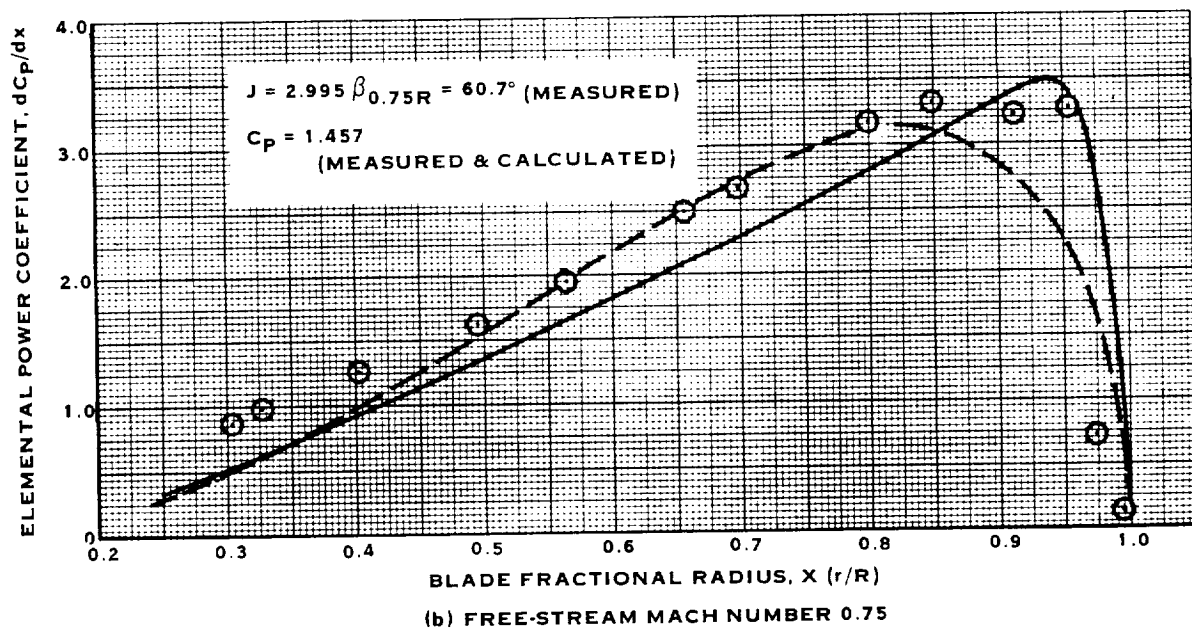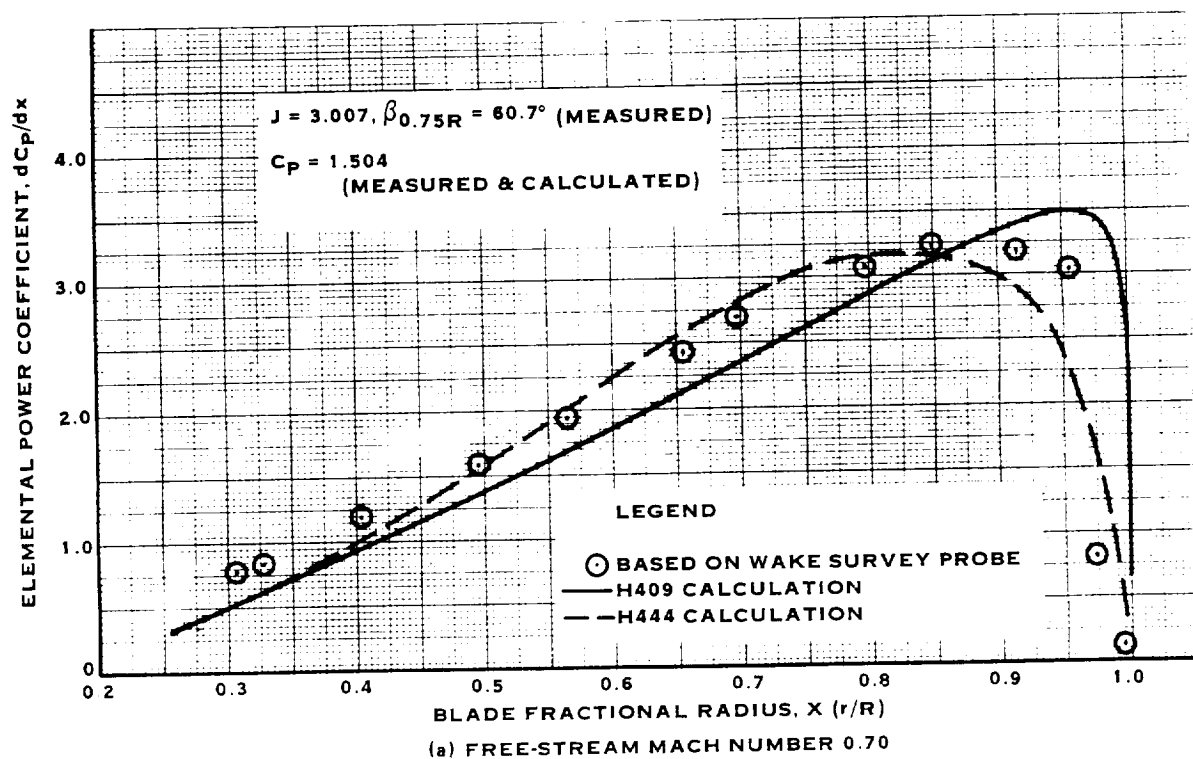(a) FREE-STREAM MACH NUMBER 0.70

(b) FREE-STREAM MACH NUMBER 0.75

FIGURE 44. COMPARISON OF PREDICTED AND TEST BASED ELEMENTAL POWER LOADING DISTRIBUTIONS

103

(c) FREE-STREAM MACH NUMBER 0.80
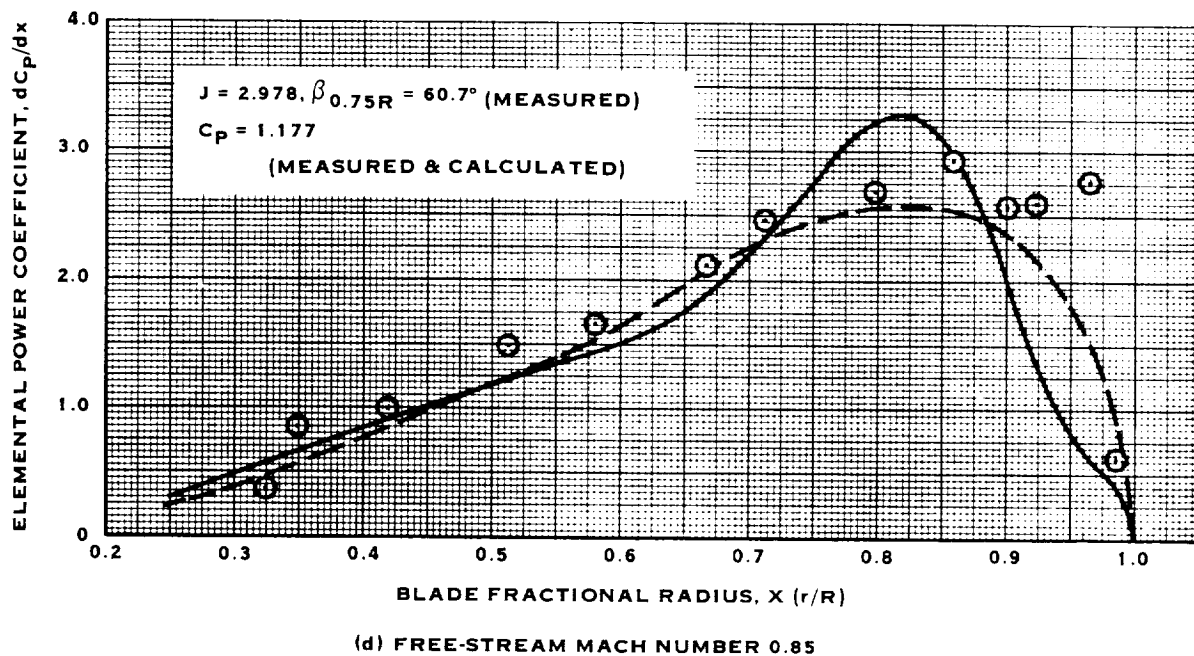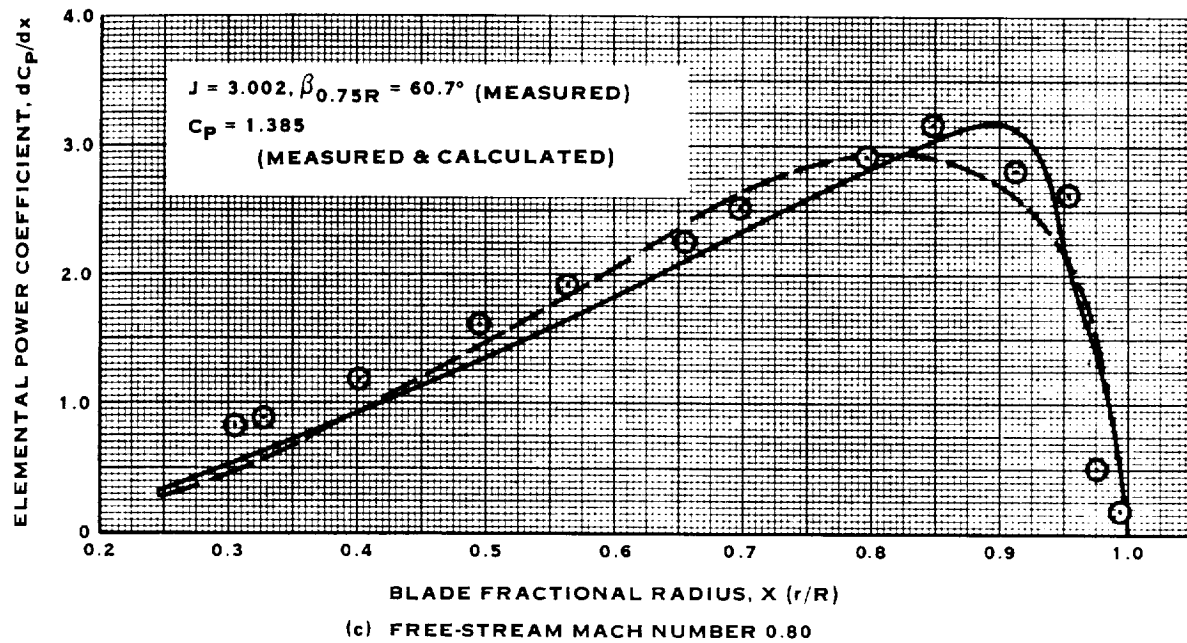

(d) FREE-STREAM MACH NUMBER 0.85
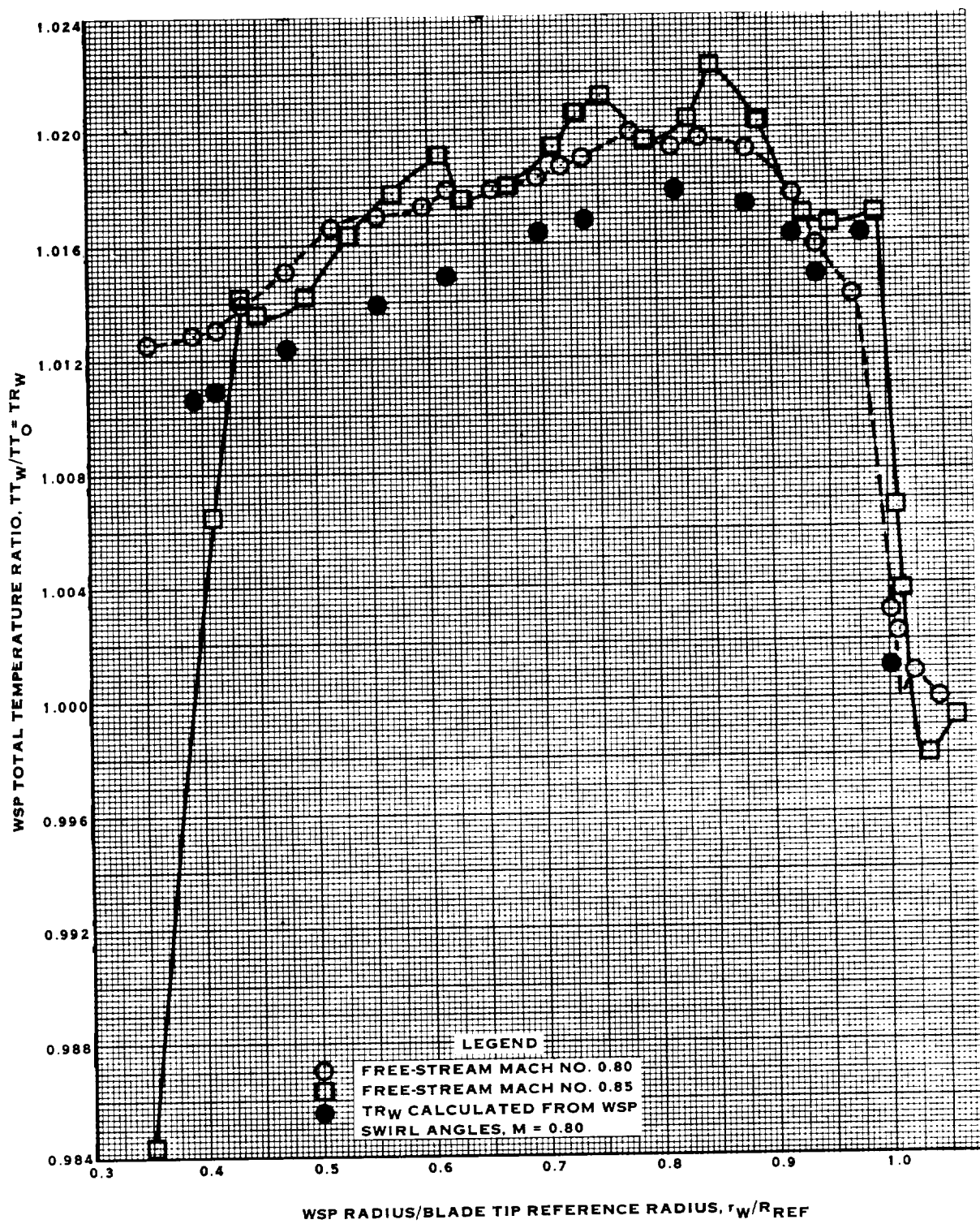
FIGURE 44. (CONTINUED)

104

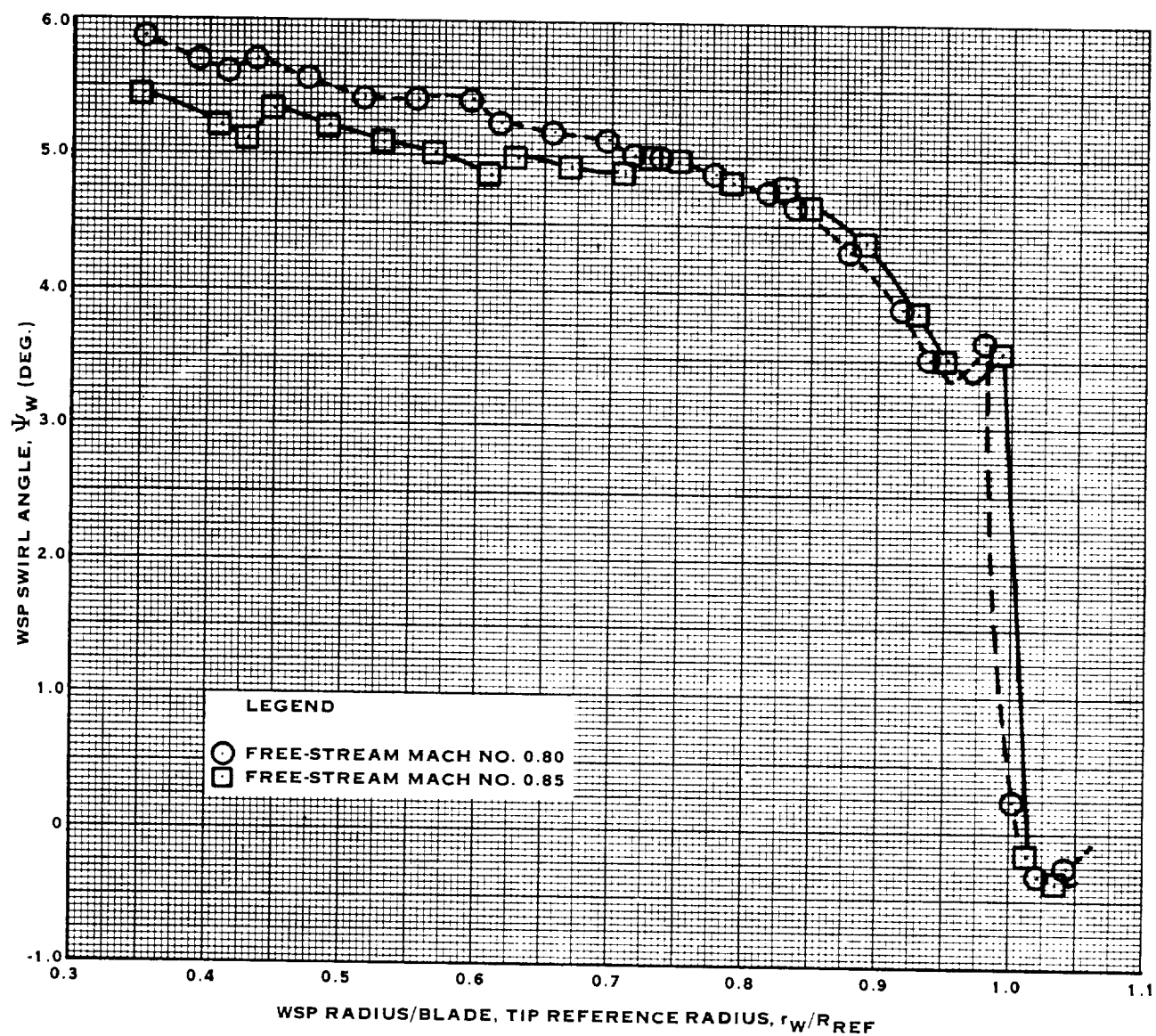FIGURE 45. WAKE SURVEY PROBE TEMPERATURE RATIO

105

FIGURE 46. WAKE SURVEY PROBE SWIRL ANGLE

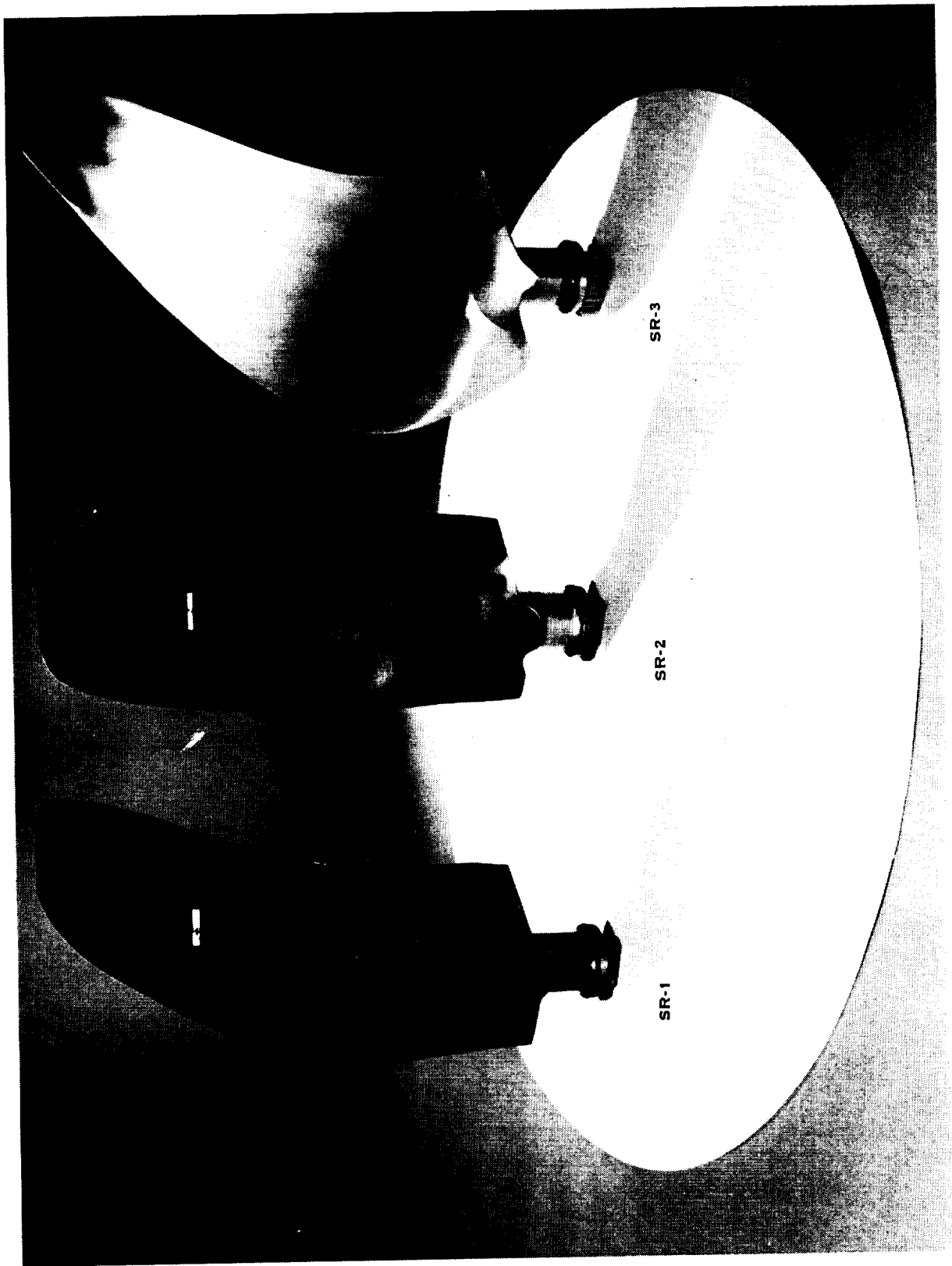FIGURE 47. PROP-FAN MODEL BLADE CONFIGURATIONS

107

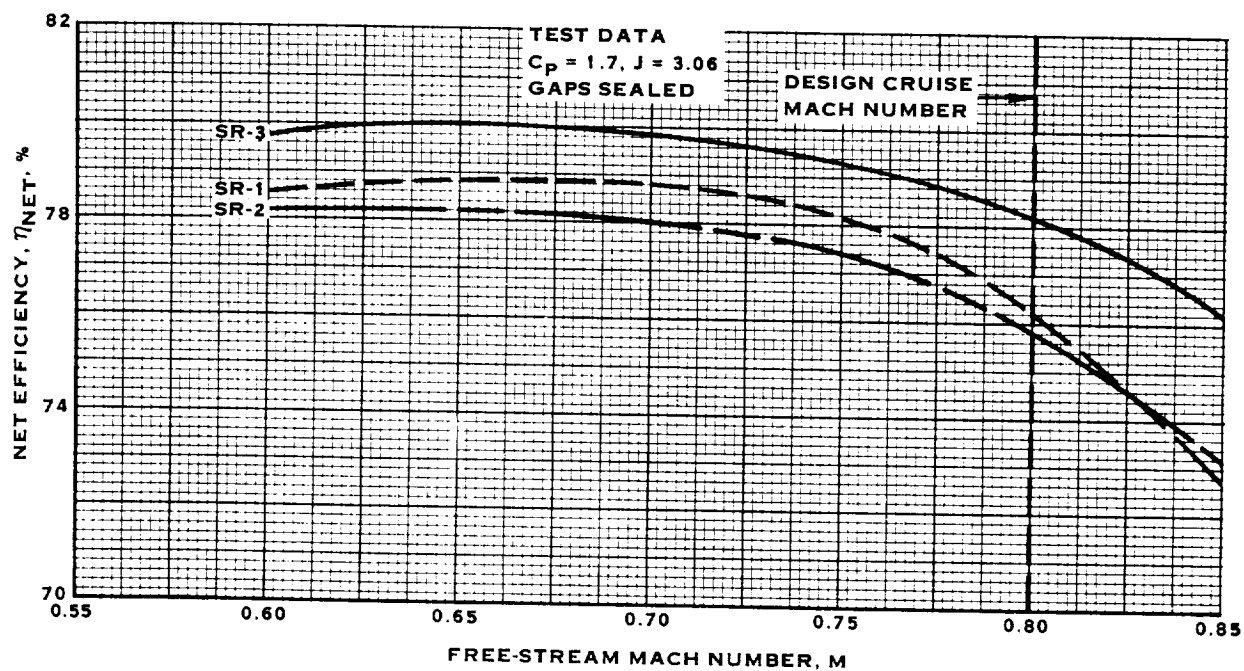FIGURE 48. PROP-FAN PERFORMANCE SUMMARY

108
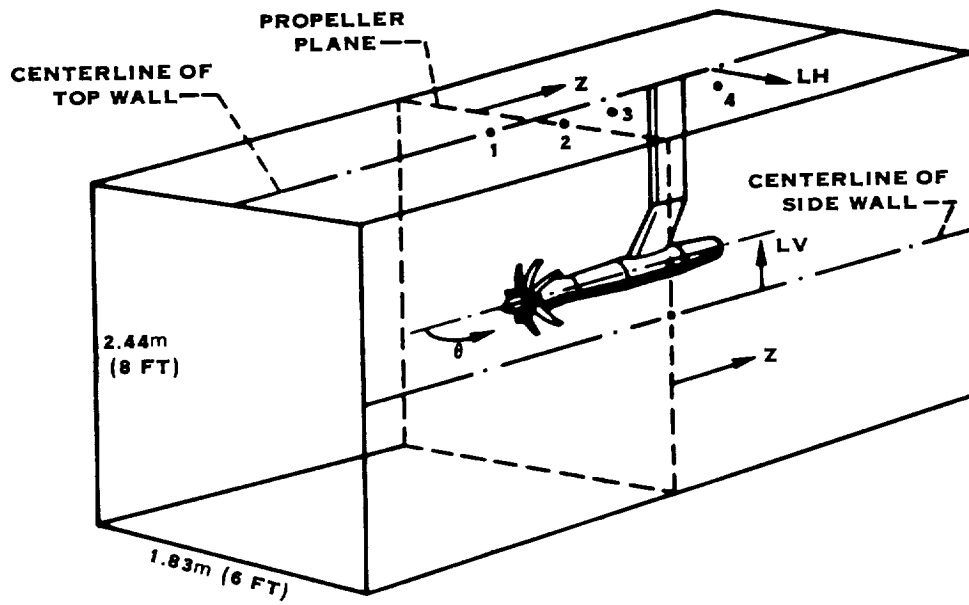
TRANSDUCER POSITIONS, CM/IN.

POSITIONS	1		2		3		4	
Z	-27.7	-10.9	0.953	0.375	45.2	17.8	104.4	41.1
LH	2.54	1.0	10.2	4.0	7.62	3.0	31.5	12.4
LV	121.9	48.0	121.9	48.0	121.9	48.0	121.9	48.0
NOMINAL ANGLE, θ	77°		90°		110°		130°	

(A) PRESSURE TRANSDUCER POSITIONS.

FIGURE 49. ACOUSTIC TESTING IN POROUS-WALL TUNNEL

NEAR FIELD NOISE

$J \approx 3.06, \quad C_P \approx 1.7, \quad M_0 = 0.80$

FORE AND AFT LOCATION IN PROP-FAN DIAMETERS

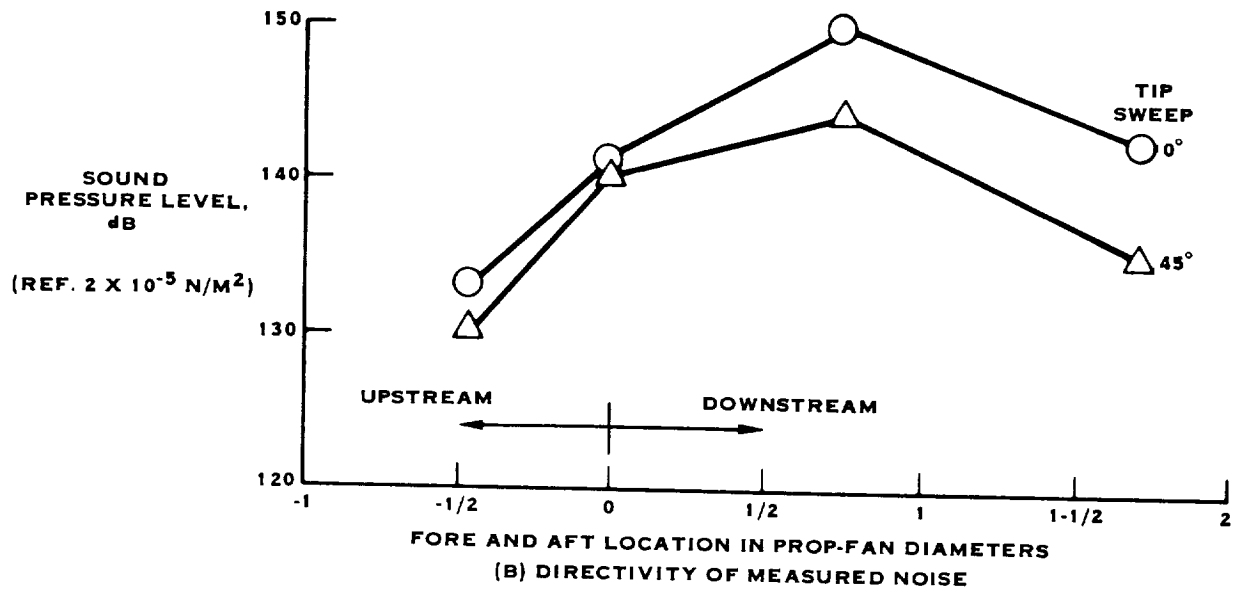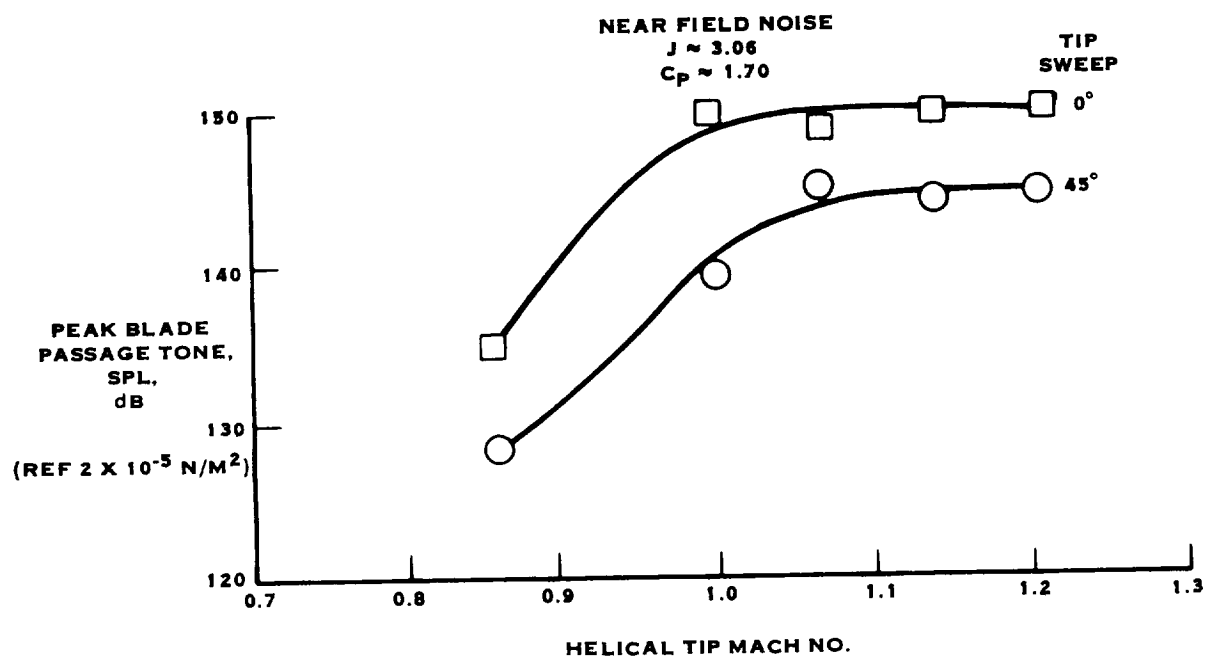(B) DIRECTIVITY OF MEASURED NOISE

FIGURE 49. CONTINUED

110

(C) EFFECT OF TIP MACH NUMBER ON MEASURED NOISE

FIGURE 49. CONCLUDED

111

APPENDIX A
ADJUSTED METHOD USED TO OBTAIN MEASURED PROPELLER THRUST

The propeller at windmill (no power) was used as a reference condition to correct the thrust readings from the rotating balance. This procedure was required to overcome a slow thermal drift in the rotating balance thrust reading. Windmill reference conditions were established during special tunnel runs using the strut-mounted force system. Dimensionless propeller thrust coefficient and advance ratio were used to eliminate possible small variations in windmill operation due to any day-to-day changes in wind tunnel conditions. After establishing the reference windmill conditions (Figures A.1 and A.2), incremental thrust data were obtained using the rotating balance in a windmill-power-windmill test sequence. At each desired power point, the PTR was first windmilled, then a power point was taken followed by a second windmill point. By subtracting from the thrust at the power point the average of the two windmill points (from the rotating balance) an incremental propeller thrust was obtained. Since the drift in thrust output from the rotating balance was very small over the short time increment required to obtain the three data points, any significant error (in the incremental thrust) could be eliminated. The incremental thrust from the rotating balance was combined with the reference windmill conditions determined in the earlier tests (with the strut-mounted force system) to establish the final propeller operating conditions. The procedure and equations that were used to establish the final adjusted performance conditions were:

(a) Obtain an average reference windmill advance ratio (JPR) for each blade angle and Mach number from the powered runs.

(b) Obtain an equivalent blade angle (β eq) from JPR of the powered runs and the windmill-advance-ratio curves generated in the windmill drag runs (Figure A.1).

(c) Obtain the reference effective (or net) thrust coefficient at windmill (CT$_{EFR}$) at βeq from the effective-thrust-coefficient-at-windmill curves generated in the windmill drag runs (Figure A.2).

(d) Calculate and print adjusted summary tables based on the reference advance ratio (JPR) and reference effective thrust coefficient (CTEFR). The thrusts at power-points are adjusted for thermal zero shift according to the equation:

$$CTP = CTB - CTWB \left(\frac{JP^2}{JPW^2} \right) + CT_{EFR} \left(\frac{JP^2}{JPR^2} \right)$$

where   CTP = adjusted thrust coefficient (rotating balance)

           CTB = power-point thrust coefficient (rotating balance)

JP = power-point advance ratio

CTWP = average of effective thrust coefficients from windmill points before and after power-point (rotating balance)

JPW = average of advance ratios from windmill points before and after power-point

and JPR and CT_{EFR} as described above.

Figures A.1 and A.2 illustrate the procedure described above, shown on the JPR and CT_{EFR} versus $\beta_{0.75R}$ plots used for the data reduction. Identical propeller hardware (SR-1) with a conic spinner) was tested in both the NASA Lewis 2.44 x 1.83m (8 x 6 ft) tunnel and the UTRC 2.44m (8 ft) octagonal tunnel using different Propeller Test Rigs (PTR). The NASA data were reduced using the Adjusted Performance Method described above. Figure A.3 presents a comparison of data from these two facilities at 90% and 100% design power loading. The data agree within about one percent at 90% loading, and at design the agreement is even better. A slight extrapolation of the UTRC data was required to obtain the design power loading condition due to limited power capability of that facility's PTR.
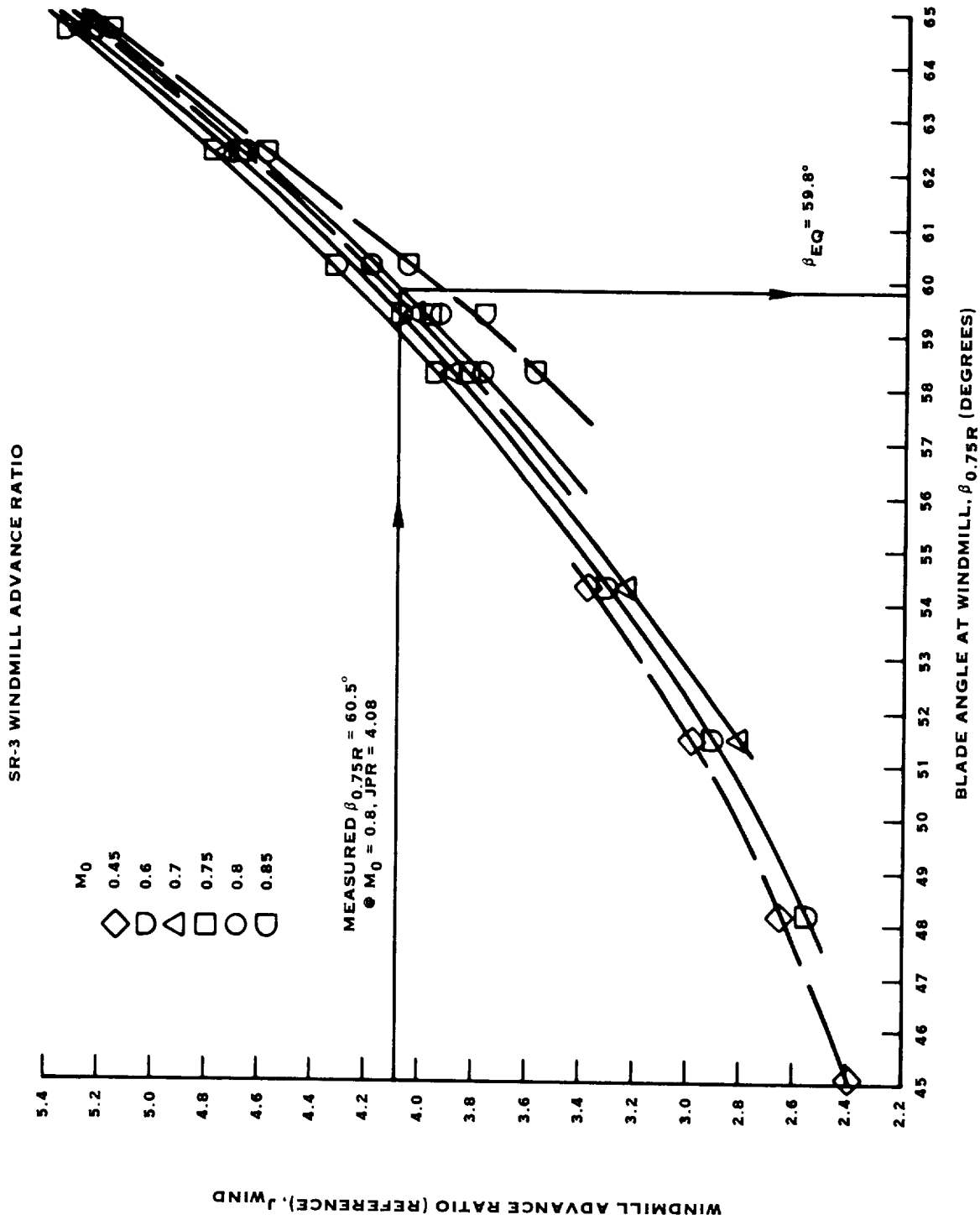
FIGURE A.1 - REFERENCE ADVANCE RATIO VALUES FOR ADJUSTED PERFORMANCE CALCULATIONS
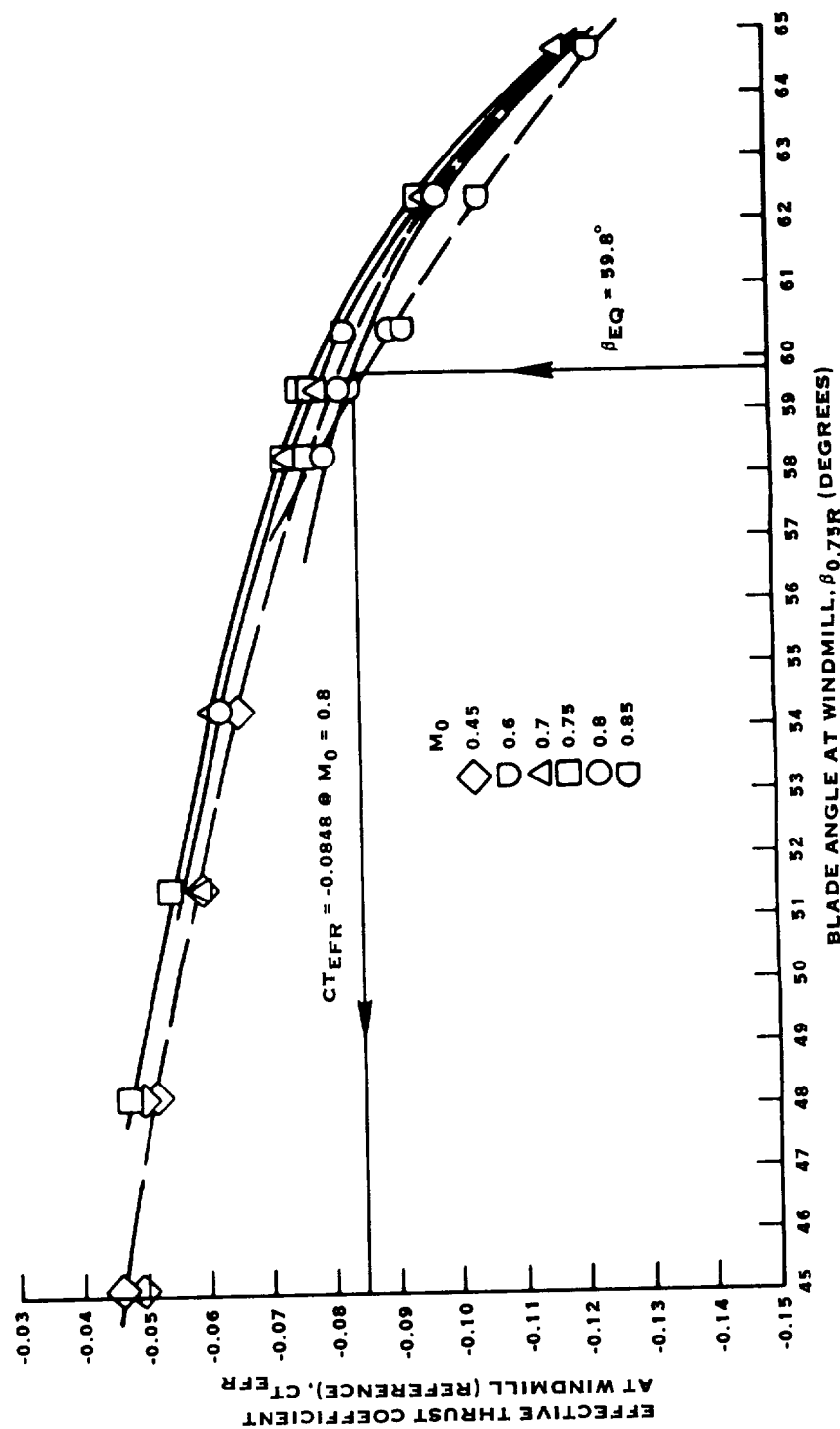
SR-3 WINDMILL DRAG

FIGURE A.2 - REFERENCE WINDMILL THRUST COEFFICIENT VALUES FOR ADJUSTED PERFORMANCE CALCULATIONS
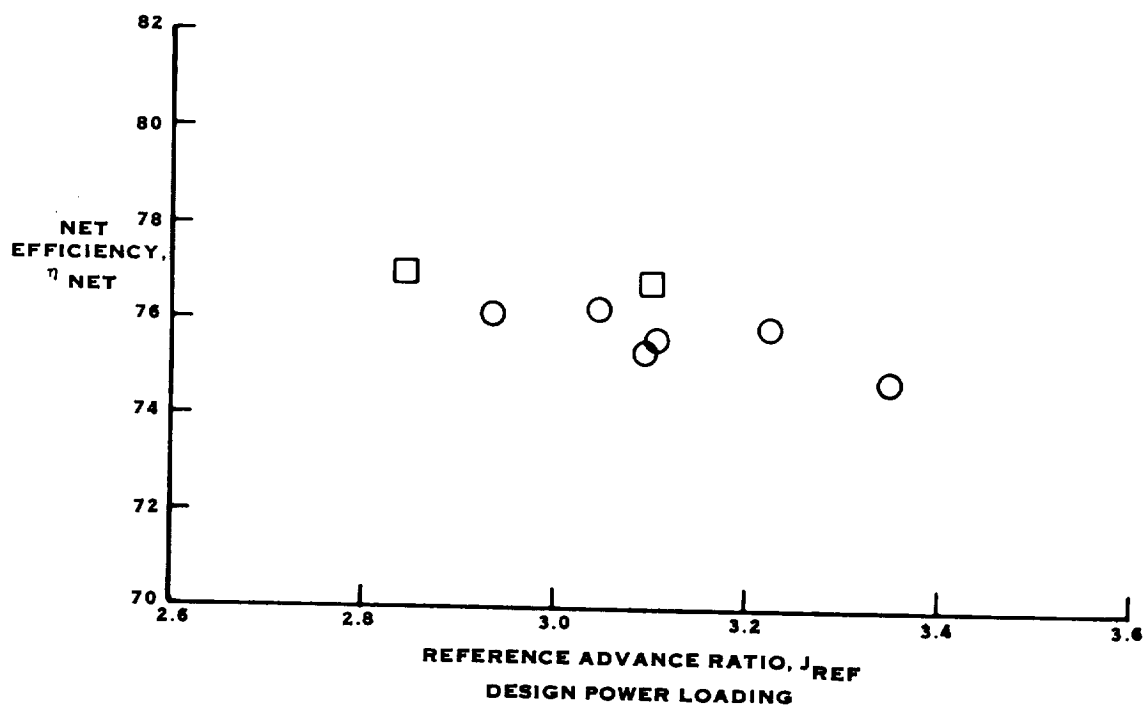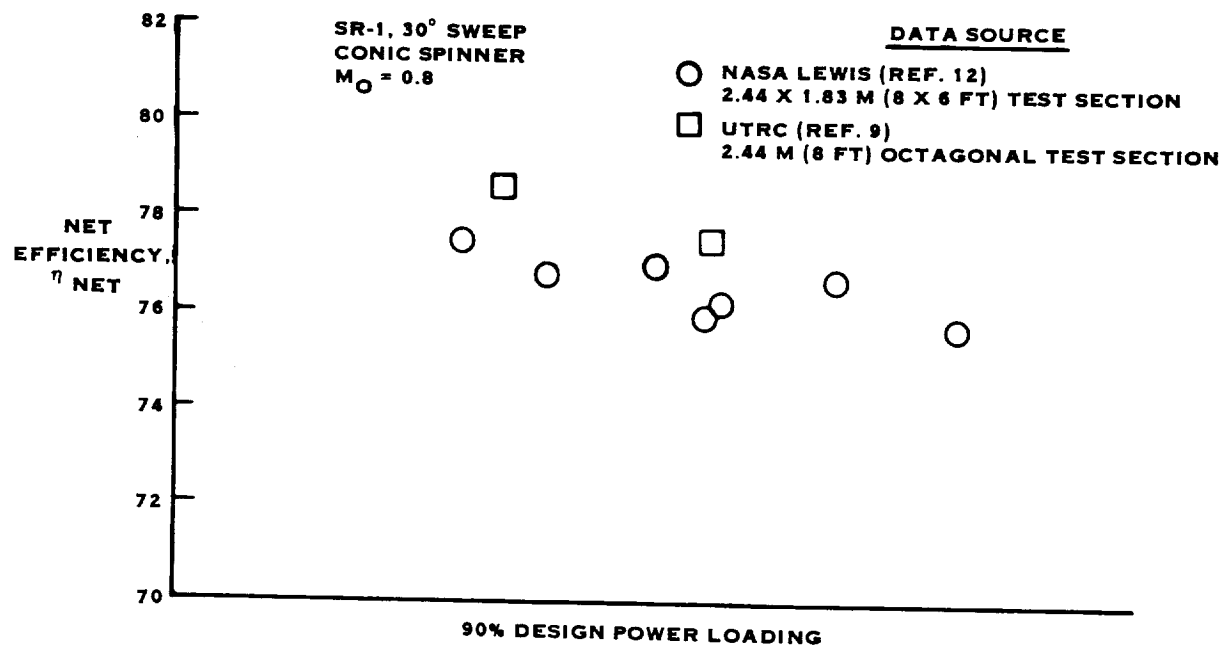
115

FIGURE A.3. PERFORMANCE COMPARISON FOR DATA FROM TWO WIND TUNNELS -
SR-1 PROP-FAN

116

APPENDIX B

EQUATIONS RELATING ACTUAL AND
REFERENCE PERFORMANCE CHARACTERISTICS

Definitions

1. $D/D_{REF} = f(\beta 0.75R, N)$, see Figure 14.

2. Actual quantities are based upon D and are not subscripted.

3. Reference quantities are based upon D_{REF} and are subscripted "REF".

4. Net efficiency is not dependent upon diameter.

5. $D_{REF} = D/(D/D_{REF})$.

6. Reference advance ratio and power coefficient:

$$J_{REF} = V/(n \cdot D_{REF}) \qquad (B2)$$

$$C_{P_{REF}} = P/(\rho \cdot n^3 \cdot D^5_{REF}) \quad (B3)$$

7. Actual advance ratio and power coefficient:

$$J = V/(n \cdot D) \qquad (B4)$$

$$C_P = P/(\rho \cdot n^3 \cdot D^5) \qquad (B5)$$

Relationships for the Various Performance Summaries Presented in this Report

1. To use the reference performance charts (Figures 25 - 31 for actual J & C_P values.

$$J_{REF} = J(D/D_{REF}) \qquad (B6)$$

$$J_{REF} > J$$

$$C_{P_{REF}} = C_P (D/D_{REF})^5 \qquad (B7)$$

$$C_{P_{REF}} > C_P$$

where D/D_{REF} is read from Figure 14.

2. To obtain power loadings (P/D^2) at specific tip speeds (U) as shown in Figures 32 through 40 from the reference performance coefficient charts.

$$J_{REF} = \frac{\pi \cdot V}{U} \quad (D/D_{REF}) \tag{B8a}$$

or in terms of Mach number,

$$J_{REF} = \pi \, c_{std} \, \frac{M}{U/\sqrt{\Theta}} \quad (D/D_{REF}) \tag{B8b}$$

and,

$$C_{P_{REF}} = \frac{\pi^3 \cdot g \cdot R \cdot t_{std}}{p_{std}} \left(\frac{P/D^2}{\sqrt{\Theta \cdot \delta}}\right) \frac{(D/D_{REF})^5}{(U/\sqrt{\Theta})^3} \tag{B9a}$$

or,

$$C_{P_{REF}} = \frac{\pi^3}{\rho} \quad (P/D^2) \quad \frac{(D/D_{REF})^2}{U^3} \tag{B9b}$$

and, in terms of J_{REF} and M

$$C_{P_{REF}} = \frac{(D/D_{REF})^2}{\gamma \cdot p_{std} \cdot c_{std}} \left(\frac{P/D^2}{\sqrt{\Theta} \cdot \delta}\right) \left(\frac{J_{REF}}{M}\right)^3 \tag{B9c}$$

3. To obtain performance characteristics for specified tip rotational Mach numbers:

$$J_{REF} = \frac{\pi M}{M\Omega} \quad (D/D_{REF}) \tag{B10}$$

where, $M\Omega = U/c$

$$C_{P_{REF}} = \frac{(D/D_{REF})^5}{(M\Omega)^3} \frac{P/D^2}{\sqrt{\Theta} \cdot \delta} \frac{\pi^3}{\gamma \cdot p_{std} \cdot c_{std}} \tag{B11}$$

118

4. The equation relating the actual and the reference tip relative Mach number is presented in the text, and is:

$$\text{MREL} = \text{Mo} \left[\left(\frac{\pi}{J_{\text{REF}}} \right)^2 \left(\frac{D}{D_{\text{REF}}} \right)^2 + 1 \right]^{1/2} \tag{B12}$$

APPENDIX C
CALCULATION OF dCp/dx AT BLADE CENTERLINE FROM THE WAKE SURVEY PROBE (WSP) MEASUREMENTS

Measurements

P_s, P_t, T_t and ψ @ 27 radial locations. See flowpath sketch, Figure C.1.

Assumptions and Definitions

a. Elemental flow (dW), total temperature (T_t) and rCu are constant for a stream-tube downstream of the blades.

b. Prop-Fan slipstream boundary is determinable from the WSP measurements.

c. Streamlines are the same from the blade to the WSP station for all conditions that have the same slipstream boundary.

d. Total temperature provides a better measure of the dCp/dx loadings than swirl angle (ψ). This is justified by the adiabatic efficiencies (η_{ad}) which are calculable from each; generally $\eta_{ad} > 100\%$ from ψ and $< 100\%$ from TR, as shown in item 4.

e. Streamlines are predictable from an internal flow compressible turbofan streamline curvature program for which the slipstream boundary represents the OD wall.

f. $dCp/dx = dP/dx / \rho_o n^3 D^5$

g. Blade centerline variables are not subscripted.

h. Pitch angles, Θ, are from design point analysis.

i. Calibrated WSP measurements are converted to the quantities required for this analysis by:

$$M_w = \left(\left[(P_T/P_S)_w^{2/7} - 1 \right] 5 \right)^{1/2}$$

$$T_{sw} = \left(1 + M_w^2/5 \right)^{-1} T_{tw}$$
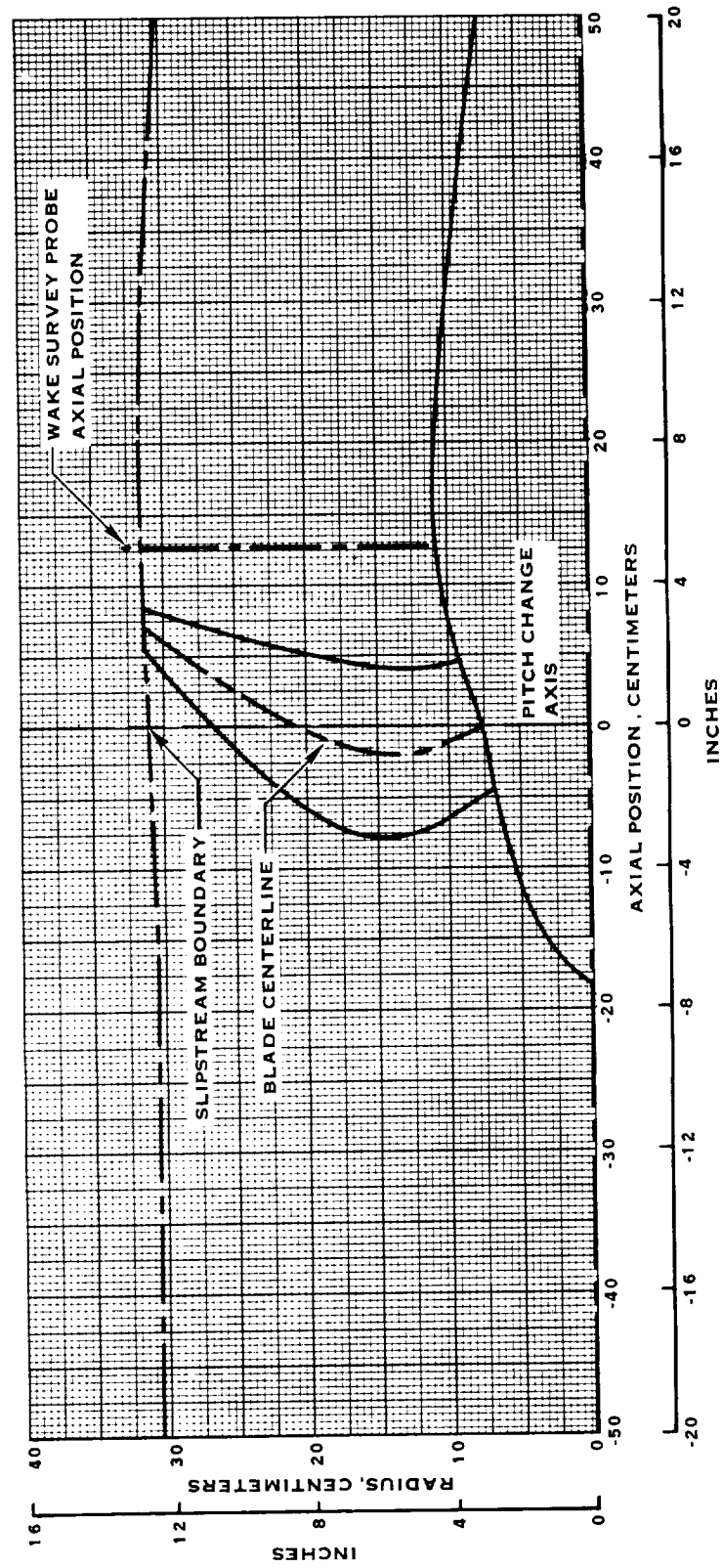
$$C_w = \left(\gamma_w g R T_{sw} \right)^{1/2} M_w$$

FIGURE C-1. FLOWPATH FOR POWER LOADING CALCULATIONS

$$C_{xw} = C_w \cos \psi_w \cos \theta_w$$

$$g\rho_w = P_{sw}/(R \cdot T_{sw})$$

$$C_{uw} = C_w \sin \psi_w \cos \theta_w$$

$$TR_w = T_{tw}/T_{to}$$

Equations for calculating dCp/dx

1. From WSP total temperatures measurements:

From the steady flow energy equation:

$$dP = CP \cdot J \cdot T_{to} (TR_w - 1) dW_w$$

and by assumptions and definitions:

$$dW_w = dW$$

$$TR_w = TR$$

$$dW_w = 2 \pi g\rho_w C_{xw} r_w dr_w$$

$$dr = dx (D/2)$$

$$r_w = x (D/2)(r_w/r)$$

and, defining a condition constant:

$$Q = (\pi \cdot CP \cdot J \cdot T_{to})/(2\rho_o n^3 D^3)$$

then,

$$dCp/dx = Q \text{ x } (r_w/r)(dr_w/dr) g\rho_w C_{xw} (TR_w - 1) \tag{C1}$$

The relationships between r_w and r and dr_w and dr were obtained from curve fits of the design point streamline analysis:

$$r = -2.381 + 1.336 r_w - 0.0121 r_w^2 \tag{C2}$$

122

and,

$$dr/dr_w = 1.336 - 0.0242\ r_w \tag{C3}$$

2. From WSP swirl angle (swirl velocity) measurements:

From the steady flow energy equation:

$$dP = dW_w\ (UC_u)_w/g$$

since,

$$C_{uw} = C_{xw}\ \tan \psi_w$$

$$dW_w = dW$$

$$(UC_u)_w = UC_u$$

$$U_w = 2\pi n\ r_w$$

and, defining a condition constant:

$$S = \pi^2/(2g\,\rho_o\,n^2 D^2)$$

$$dCp/dx = S\ x^2\ (r_w/r)^2\ (dr_w/dr)\ g\rho_w\ C_{xw}^2\ \tan \psi_w \tag{C4}$$

3. Correlation between TR_w and ψ_w.

Theoretically TR_w and ψ_w should produce the same dCp/dx values. However, due to the very large influence of small temperature and swirl angle errors, this equivalency is practically never achieved. The WSP temperature ratios are shown in Figure 45 for the 0.80 and 0.85 free-stream Mach number cases which are illustrated in the dCp/dx distributions, Figure 44 (c) and 44 (d). The temperature ratios calculated from the swirl angles are also shown on Figure 45 for the 0.80 Mach number case. These temperature ratios are about 0.002 lower than those based upon the measured temperatures, representing about 0.6°K (1.0°R) differential. The 0.80 and 0.85 Mach number swirl angles are shown in Figure 46.

123

Equating either the two dCp/dx equations, C1 and C4, or the steady flow energy Euler equations, defines the theoretical equivalency between TR_w and ψ_w.

4. dCp/dx distributions were calculated from the wake survey probe total temperature measurements using equation C1. This decision was made because the total temperature measurements were believed to be more accurate than the swirl angle measurements. Evidence of this is shown in the levels of adiabatic efficiencies that were calculated from both the temperature and swirl angle measurements. A typical example of the adiabatic efficiencies calculated from both measurements for the 0.80 Mach number condition, Figure 44c, is shown in the table below. Adiabatic efficiencies were calculated from:

Condition: $M = 0.80$, $J = 3.002$, $Cp = 1.385$, $\beta_{0.75R} = 60.7°$

r_w/R	ηad (from TR_w)	ηad (equiv. TR_w from ψ_w)
1.001	64.6%	176.2%
0.980	88.7%	77.3%
0.940	94.9%	101.2%
0.879	93.9%	104.8%
0.818	96.5%	105.2%
0.737	94.1%	106.4%
0.617	95.0%	114.1%
0.475	98.1%	119.4%

1. Report No. NASA CR-3505	2. Government Accession No.	3. Recipient's Catalog No.
4. Title and Subtitle EVALUATION OF WIND TUNNEL PERFORMANCE TESTINGS OF AN ADVANCED 45° SWEPT EIGHT-BLADED PROPELLER AT MACH NUMBERS FROM 0.45 TO 0.85		5. Report Date March 1982
		6. Performing Organization Code 73030
7. Author(s) C. Rohrbach, F. B. Metzger, D. M. Black, and R. M. Ladden		8. Performing Organization Report No.
9. Performing Organization Name and Address Hamilton Standard Division of United Technologies Windsor Locks, Connecticut 06096		10. Work Unit No.
		11. Contract or Grant No. NAS3-20769
12. Sponsoring Agency Name and Address National Aeronautics and Space Administration Washington, D.C. 20546		13. Type of Report and Period Covered Contractor Report
		14. Sponsoring Agency Code 535-03-12

16. Abstract

The increased emphasis of fuel conservation in the world and the rapid increase in the cost of jet fuel has stimulated a series of studies of both conventional and unconventional propulsion systems for commercial aircraft. The results of these studies indicate that a fuel saving of 15 to 30 percent may be realized by the use of an advanced high-speed turboprop (Prop-Fan) compared to aircraft equipped with high bypass turbofan engines of equivalent technology. The Prop-Fan propulsion system is being investigated as part of the NASA Aircraft Energy Efficient Program. This effort includes the wind tunnel testing of a series of 8 and 10-blade Prop-Fan models incorporate swept blades. Test results indicate efficiency levels near the goal of 80 percent at Mach 0.8 cruise and an altitude of 10.67 km (35,000 ft). Each successive swept model has shown improved efficiency relative to the straight blade model. The fourth model, with 45° swept blades reported herein, shows a net efficiency of 78.2 at the design point with a power loading of 301 kW/m^2 (37.5 SHP/D^2) and a tip speed of 243.8 m/sec (800 ft/sec).

17. Key Words (Suggested by Author(s)) Advanced turboprop Prop-fan Energy efficient Propeller	18. Distribution Statement Unclassified - unlimited STAR Category 02		
19. Security Classif. (of this report) Unclassified	20. Security Classif. (of this page) Unclassified	21. No. of Pages 128	22. Price* A07